



UNIVERSITY OF MESSINA

DOCTORAL THESIS

**Advanced Synthesis and Characterization of
Quantum Silicon Nanowires**

SSD FIS/03

Author:
Giovanni BORGH

Supervisor:
Prof. Salvatore PATANÈ

Co-Supervisor:
Dott.ssa Rosaria PUGLISI

Coordinator:
Prof. Vincenza CRUPI

*A thesis submitted in fulfillment of the requirements for the degree of
Doctor of Philosophy in the*

Department of Mathematical and Computer Sciences, Physical Sciences
and Earth Sciences (MIFT)

Ph.D Programme in Physics, Cycle XXXIV

Academic Year 2020/2021

Index

Abstract.....	5
Introduction Nanostructures and their unique properties.....	7
Bibliography.....	13
1. Literature Overview on SiNWs synthesis.....	14
1.1 Bottom up and top-down approaches for SiNWs.....	14
1.2 Electron Beam Lithography and Reactive Ion Etching.....	15
1.3 Metal Assisted Chemical Etching.....	19
1.4 Principles of Vapor Liquid Solid mechanism.....	23
1.5 Principles of Chemical Vapor Deposition.....	29
1.6 SiNWs applications.....	36
1.7 Conclusions.....	37
Bibliography.....	38
2. Introduction to Plasmon resonance.....	42
2.1 Lorentz model.....	43
2.2 Plasmon resonance in metals.....	50
2.3 Surface plasmon resonance (SPR).....	50
2.4 Localized surface plasmon resonances.....	57
2.5 PR in cylindrical system.....	60
2.6 Surface plasmon resonance in SiNWs.....	65
2.7 Conclusions.....	66
Bibliography.....	67
3. Experimental.....	71
3.1 Pretreatment.....	71
3.1.1 Sonication.....	71
3.1.2 HF etching.....	72
3.2 Catalyst deposition via sputtering.....	73
3.3 Synthesis of SiNWs by CVD via VLS.....	75

3.4 Gold removal	76
Bibliography.....	83
4. Plasmonic behavior in 30 nm SiNWs in diameter.....	84
4.1 Electron microscopy.....	85
4.2 Electron energy loss spectroscopy (EELS).....	85
4.3 EELS/EFTEM analysis.....	87
4.4 Peak fit.....	90
4.5 EFSI spatial maps.....	92
4.6 Theoretical simulations.....	95
4.7 Conclusions.....	101
Bibliography.....	102
5. Plasmonic behavior of SiNWs between 10 e 30 nm in diameter	104
5.1 EFSI maps.....	104
5.2 Spectral features.....	109
5.3 Conclusions.....	111
Bibliography.....	112
6. Future perspectives.....	113
6.1 Plasmonics on SiNWs below 10 nm	113
6.2 Plasmonics on SiNWs: shell oxide effect	114
7. Early stages of aluminum-doped zinc oxide deposited by sputtering on silicon nanowires	116
7.1 Introduction.....	117
7.2 Methods	119
7.3 Results and discussion	119
7.4 Conclusions.....	127
Bibliography	128
Conclusions.....	130
Acknowledgments	131

Abstract

The great advances in technology observed in recent decades have only been possible thanks to the miniaturization of transistors, as foreseen by Moore's law.

However, the device's miniaturization represents a necessary requirement for progress in general and not only in the electronic field, so much so that it has already affected every branch of science.

As well known, this has made the nanoscience and nanotechnology sectors fields of great interest as well as subject of large financial resources by public and private entities. And this trend is constantly increasing.

Although the most known and used nano objects are made of metals, silicon nano systems are very promising materials because they can show useful properties like metal particles. Furthermore, silicon until now has dominated the semiconductor industry and is expected to continue to do so in the next few years. This is due to its abundance on earth, its well-known electronic properties, stability, inertness, safety, and cost.

About that, Silicon NanoWires (SiNWs) attract great interest due to their very useful electro-optical properties. NWs are elongated quasi one-dimensional (1D) nanostructures with a high aspect ratio (higher than 5:1) [1] whose diameter is of the order of tens of nanometers. This geometry generates peculiar characteristics that significantly differ from the corresponding ones of bulk, making SiNWs promising building blocks for nanostructured devices spanning through several fields, going from microelectronics to photovoltaics, photonics, and sensors. They can be used for light harvesting, to obtain radial p-n junctions in transistors, to amplify SERS signals as nanoresonators and they have several other applications.

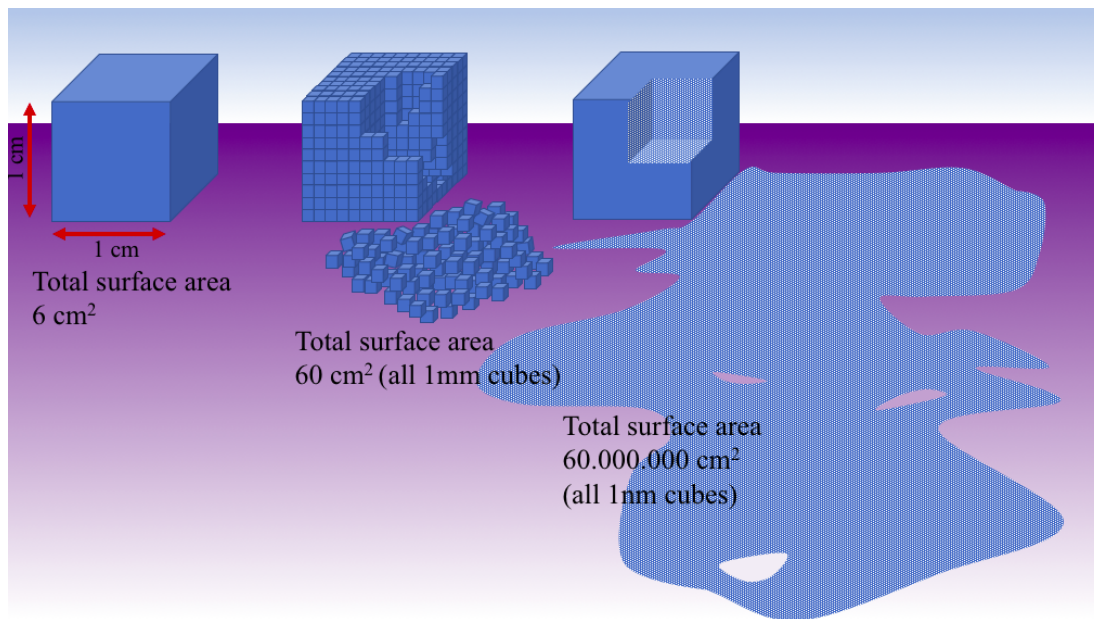
The purpose of this thesis is to explore the most used synthesis method of SiNWs, observe their morphological and structural properties and study their electro-optical properties. In particular the investigation focuses on electronic phenomena, among which we find the plasmon resonance that these cylindrical-like structures exhibit in the energetic range between UV and Vis. The major scope is to experimentally

observe, distinguish and describe the plasmon's resonances through electron energy loss spectroscopy. The general theory is presented although there is no univocal analytical model at the state of the art for the description of the electronic phenomena observed in these nanostructures. The aim is to understand the several aspects not yet fully clear of SiNWs mainly clarifying how the geometry and medium variations influence the electronic features. To support the experimental observations, theoretical simulations based on the finite element method were also performed.

[1] TsakalagosL2008Mater.Sci.Eng.R62175–89.

Introduction

Nanostructures and their unique properties



Nanomaterials, nanostructures and nanoparticles (and several others) are terms that refer to an object having at least one of its three dimensions below 100 nanometers, one hundred billionth of a meter.

The study of nanomaterials constitutes a major research field all over the world and is currently in full development in all areas of science and technology. New application opportunities, reducing costs, increasing efficiency and novel design have been provided by reducing size.

In general, nanosystems can be classified in three types: two-dimensional (2-D, like sheets, films), with a single dimension below 100 nm; one-dimensional (1-D, like tubes, wires) which have two dimensions below 100 nm and quasi-zero dimensional (0-D, like clusters, dots), with all three dimensions smaller than 100 nm.

These systems can be very different from each other in terms of size and shape as well as in chemical composition and most of all in properties. The nanomaterials can be made from a single element, such as iron, gold, silver, silicon, zinc (and many others) or to be compounds such as oxides and still resulting from the composition of two or more materials. They can also be made up of organic material and be biocompatible. They can have the most imaginative geometries, indeed there are nano

rods, nano triangles, nano cubes, nano springs, nano stars and countless others (Figure 1).

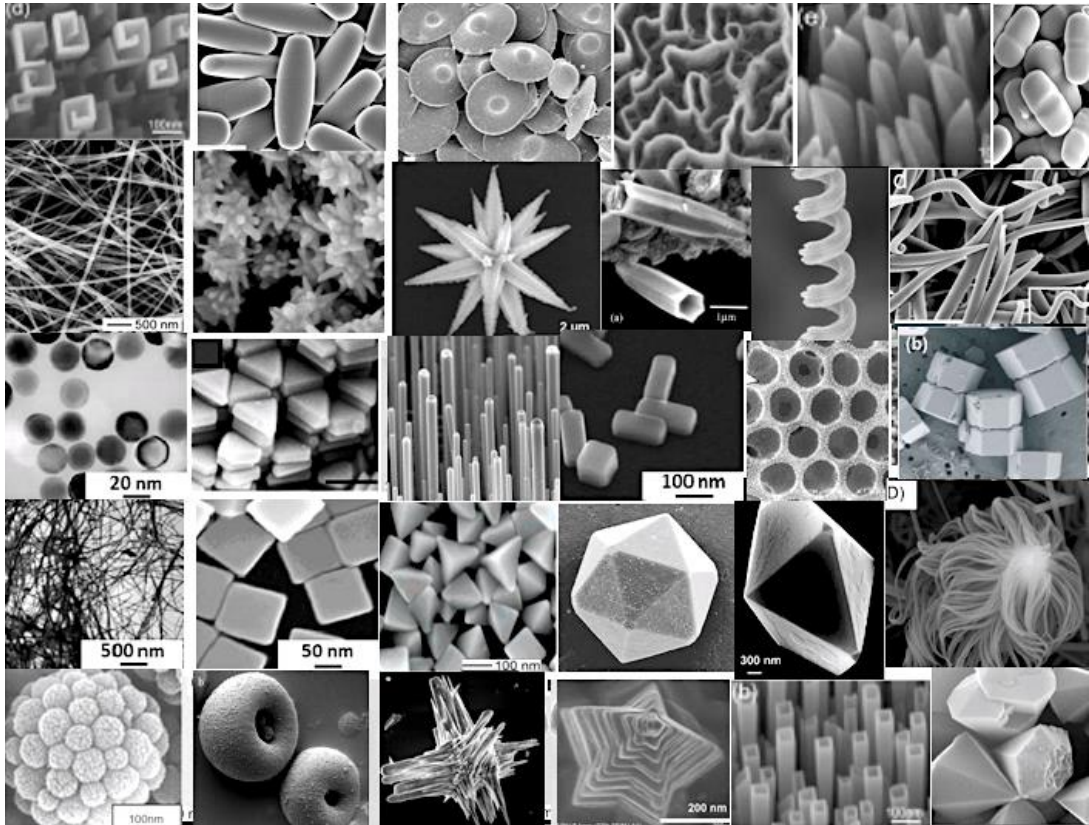


Figure 1: Experimental micrographs of Nanoparticles with different shapes, sizes, and composition seen through transmission electron microscopy (TEM) and/or scanning electron microscope (SEM) illustrate the broad possibilities of nanoscience [1-4].

The nanoscopic dimensions provide them with unique physical (thermal, electrical, optical,...) and chemical (reactivity, solubility,...) properties. At the nanoscale, indeed, the features of materials change dramatically mainly due to the quantum effects. Surface effects become important too, indeed many properties are related to the surface/volume ratio, and since it increases as the system size decreases, at the nanometer scale it is very high.

If we consider the surface of a sphere, its area is proportional to the square of the radius:

$$S = 4 \pi r^2$$

while the volume scales with the cube of the radius:

$$V = \frac{4}{3} r^3$$

The total number of atoms N in this sphere scales linearly with volume. The fraction of atoms at the surface is called dispersion F , and it scales with S/V , i.e. with the inverse radius:

$$F \propto S/V = 3 r^{-1}$$

and thus, also with the total number of atoms:

$$F \propto N^{-1/3}$$

Basically, the same relation holds also for long cylindrical geometry [5].

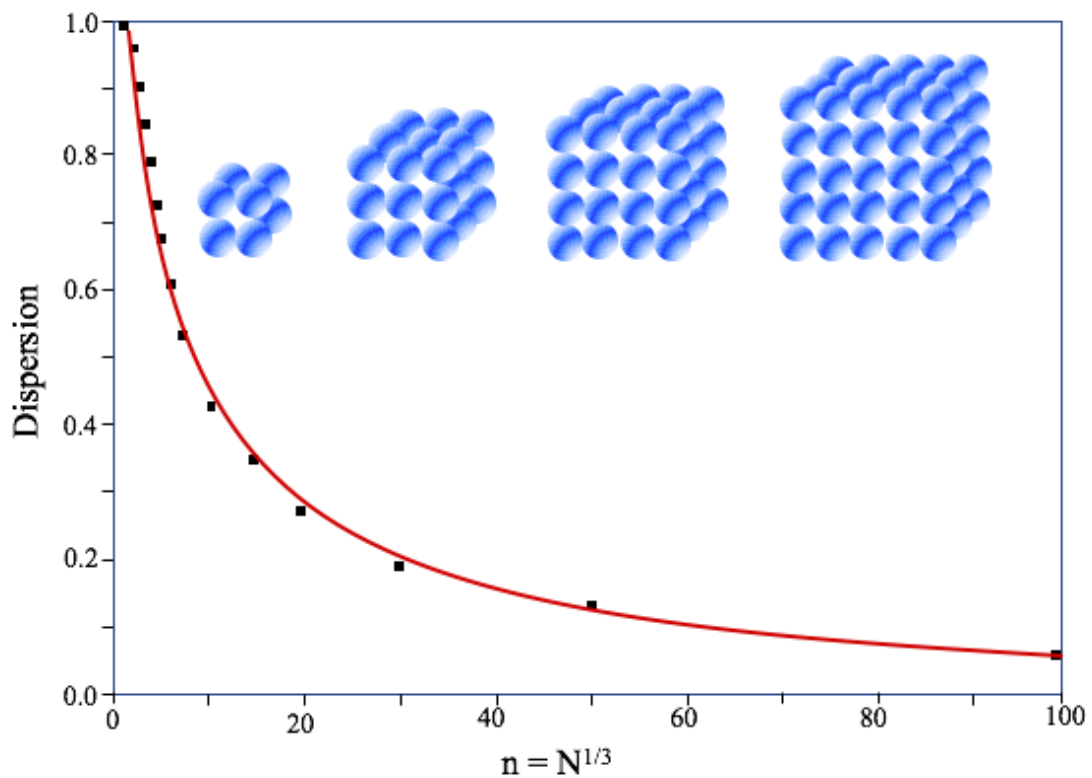


Figure 2: Evolution of the dispersion F as a function of n for cubic clusters up to $n = 100$ ($N = 106$). The structure of the first four clusters is displayed [6].

Atoms at the surface have fewer direct neighbors than atoms in the bulk. Particles with a large fraction of atoms at the surface have indeed low mean coordination number (= the number of the nearest neighbors).

This is very important, because every nanoparticle's interaction with the external environment occurs through the atoms on the surface.

The dispersion F and the mean coordination number obey the same scaling law and are equivalent measures of surface effects [6] (Figure 2). This behavior can give rise to unprecedented phenomena, not observable on macroscopic materials. For example, the cohesive energy (i.e. the bond energy per atom) scales the same way as the coordination number. The melting point dramatically decreases with the particle size. The electronic structure is affected too (quantum confinement) and the nanoparticle extinction changes, and thus the color of the same material changes with dimension (Figure 3).

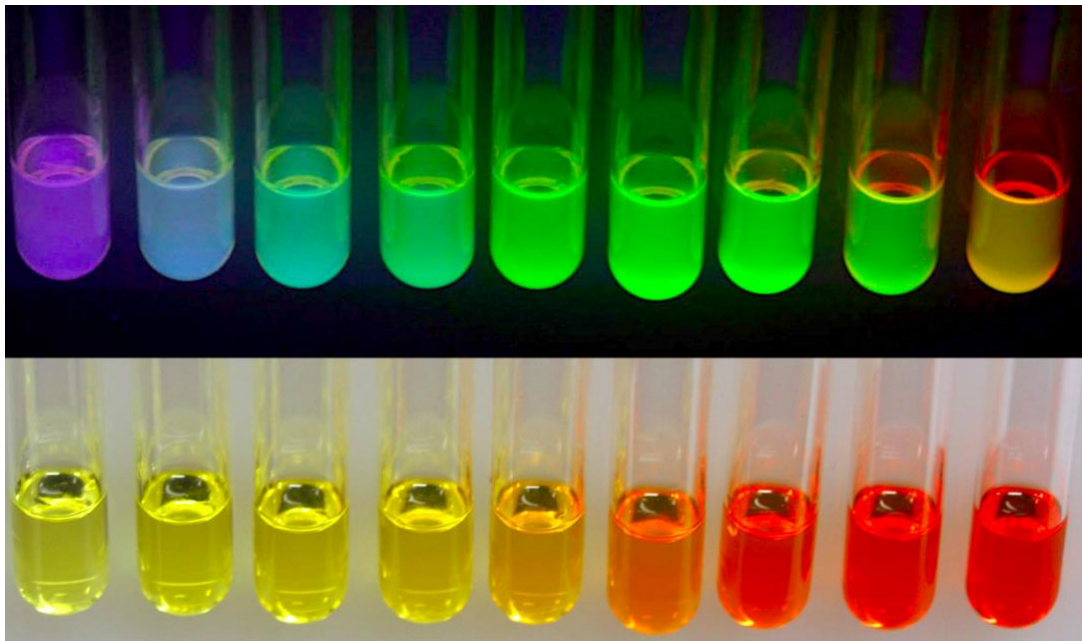


Figure 3: colloidal suspension of CdSe quantum dots of increasing size from left to right (approximately 1.8 nm diameter) to right (approximately 4.0 nm diameter). Bottom: Samples viewed in ambient light vary in color from green-yellow to orange-red. Top: The same sample viewed under long-wave ultraviolet illumination varies in color from blue to yellow [7].

Moreover, nanoparticles' properties depend not only on the system size, but also on its shape. For instance, it has been observed that spherical nanoparticles have different properties from cubic or triangular nanoparticles of the same material [8].

By controlling the shape and size of nanoparticles, it is possible to design their properties to be effective in different application fields. For instance, it is possible to make it sensitive to a toxic gas for detection or to dangerous molecules for removal, build hollow nanoparticles to encapsulate another functional material such as dyes and magnetic particles [9] or capable of carrying a drug or catching a toxin offering high stability [10]. Also, the building of a new generation of transistors, new smart drugs and sensitive materials for diagnostics imaging and photothermal cancer therapy are possible [11].

Many of these extraordinary properties are related to the peculiar electromagnetic response of conductive nanostructures, observable as spectral extinction bands, due to a phenomenon called plasmon resonance, which causes the increasing electric field near the surface of the nano-object. Theoretically, the field can be amplified over a million times and this makes possible applications otherwise unattainable in many fields.

Furthermore, when plasmons are triggered in metallic NWs such as Au or Ag, the structures can behave as nanoantennas, also these nanostructures can be used to make nanolasers. This is due to the fact that the wire-like structures act like nano-resonators in which some permitted plasmonic modes exhibit harmonic behavior. This feature makes it possible to modulate the spatial distribution of the locally amplified electric field as well as the resonant frequencies, opening the way to novel technological applications. In the following, it will be shown an original behavior of silicon NWs, that, under certain experimental conditions, show its plasmonic character. The thesis mainly focusses on this point, that, in our opinion, is much interesting both from a fundamental and a technological point of view as silicon is still the main material of the electronics industry.

The first chapter reports an overview of the most common synthesis methods for SiNWs, spanning from bottom-up to top-down approaches focusing on the former that has been used in this work. Also, the Chemical vapor Deposition (CVD) coupled to the Vapor Liquid Solid (VLS) technique will be discussed in detail.

In the second chapter the plasmon resonance theory will be briefly introduced through the description of one of the most common models for macroscopic and nanoscopic systems of both metal and semiconductors.

Chapter three describes the experimental set up and the procedures carried out to synthesize the samples.

Subsequently, the plasmonic behavior in isolated SiNWs with different dimensions and diameter are presented.

In chapter four, experimental and theoretical data on the plasmonic behavior of NWs with diameter of 30 nm are presented and discussed.

In the subsequent chapter, the plasmonic behavior of nanowires with dimensionality ranging between 30 and 10 nm is described.

Chapter six reports the preliminary results for structures with a diameter as small as 7 nm.

In addition to the size of the structures, it is known that the presence of surface oxides modifies the plasmonic features. For this reason, the experimental investigation is presented in the next chapter aimed at understanding the effect of the variation in the thickness of the silicon oxide that encapsulates the wires.

Finally, in the seventh chapter is reported a work concerning the deposition of Aluminum doped Zinc Oxide (AZO) [12] on SiNWs. AZO is a Transparent Conductive Oxide (TCO) [13] with interesting properties, such as flexibility. The TCO is an always necessary element for electro-optical devices. Through this work we intend to demonstrate the possibility of depositing TCOs of good quality through an economical and scalable technique such as sputtering, even on highly nanostructured substrates such as an array of NWs with a view to future applications.

Bibliography

- [1] Champion, Julie A., Yogesh K. Katare, and Samir Mitragotri. "Making polymeric micro-and nanoparticles of complex shapes." *Proceedings of the National Academy of Sciences* 104.29 (2007): 11901-11904.
- [2] <https://www.fau.eu/2014/08/28/news/research/what-are-the-effects-of-nanoparticles/>
- [3] Champion, Julie A., Yogesh K. Katare, and Samir Mitragotri. "Making polymeric micro-and nanoparticles of complex shapes." *Proceedings of the National Academy of Sciences* 104.29 (2007): 11901-11904.
- [4] Ali, Attarad, Abdul-Rehman Phull, and Muhammad Zia. "Elemental zinc to zinc nanoparticles: Is ZnO NPs crucial for life? Synthesis, toxicological, and environmental concerns." *Nanotechnology Reviews* 7.5 (2018): 413-441.
- [5] Chem. Soc. Rev., 2006, 35, 583–592
- [6] E. Roduner, *Nanosopic Materials: Size-Dependent Phenomena*. The Royal Society of Chemistry, Cambridge, 2006
- [7] *J. Chem. Educ.* 2005, 82, 9, 1360A
- [8] Pal, Sukdeb, Yu Kyung Tak, and Joon Myong Song. "Does the antibacterial activity of silver nanoparticles depend on the shape of the nanoparticle? A study of the gram-negative bacterium *Escherichia coli*." *Applied and environmental microbiology* 73.6 (2007): 1712-1720
- [9] Huang, C.; Jiang, J.; Muangphat, C.; Sun, X.; Hao, Y. *Nanoscale Res. Lett.* 2010, 6, 1–5
- [10] Zhang, X.; Zhang, G.; Zhang, B.; Su, Z. *Langmuir* 2013, 29, 6722–6727
- [11] Coughlin, A. J.; Ananta, J. S.; Deng, N.; Larina, I. V.; Decuzzi, P.; West, J. L. *Small* 2014, 10, 556–565.
- [12] S. Boscarino, I. Crupi, S. Mirabella, F. Simone, A. Terrasi, 2014 *Appl. Phys. A* **116** 1287–1291.
- [13] D.S. Ginley, C. Bright, 2000 *MRS Bull.* **25.8** 15-18.

Chapter 1

Literature Overview on Si NWs synthesis

1.1 Bottom up and top down approaches for SiNWs



This chapter would like to give a general overview of the main techniques regarding the production of SiNWs. The general approaches to make SiNWs can be divided in two: bottom-up and top-down. The Bottom-Up approach attempts to build nano-systems by binding together smaller components “brick by brick” such as atoms or molecules. Basically, they are all chemical-physical methods of synthesis, which involve more or less complex synthesis reactions. The major techniques concerning the vapor phase include chemical vapor deposition (CVD), molecular beam epitaxy (MBE), atomic layer deposition (ALD). There are also techniques in the liquid state, among which we recall the sol-gel technique, electrochemical deposition or synthesis in solution of colloids.

The Top-Down approach can be likened to sculpting from a block of stone in which pieces of the base material are gradually eroded until the starting material is reduced to nanometric dimensions and the desired shape is achieved. These are substantially physical or mechanical methods. Among the many known techniques, the most widespread are those based on etching, and lithography and laser ablation.

The synthesis of the material can be sometimes templated, that means a pre-existing structure, as a mask, guides its growth determining its shape and size.

Note that not all existing techniques to obtain SiNWs have been (obviously) listed so far, because they are countless. Here we will only give an overview of the main ones, namely: the electron beam lithography (EBL) coupled with the reactive ion etching (RIE), the metal assisted chemical etching technique (MACetch) and the chemical

vapor deposition (CVD) via vapor liquid solid mechanism (VLS), that is the selected one to obtain SiNWs in this research. This latter technique is, in our opinion, the most promising since it requires low temperatures, it guarantees a high yield, and it is fast and controllable and relatively cheap.

1.2 Electron Beam Lithography and Reactive Ion Etching

Electron Beam Lithography (EBL) [1] and Reactive Ion Etching techniques (RIE) are two top-down techniques suitable to be used in fabricating densely packed SiNWs.

EBL is a very popular physico-chemical technique used to fabricate structures on the nanometric scale. Indeed, arrays of dot structures firstly produced by EBL can be used to produce vertical nanowire arrays through the subsequent use of RIE [2].

Lithography (from the Greek lithos, "stone" and, gràphein, "to write"), was developed in the 1960s [3]. It consists of a direct writing, where electron beam (the ink) exposure alters the chemistry of a material, called resist (the paper), in order to create a high-resolution photomask. Resists are polymers; there exist two types of resists. The first type is called "positive resist", it produces an exact copy of the pattern. The second type is called "negative resist", and produces inverse of the pattern to be transferred. This is possible because a positive resist dissolves in the "developer solution" (the washing solvent) only in the areas where it is exposed to the beam, while a negative resist dissolves only in those areas with which the beam has not interacted.

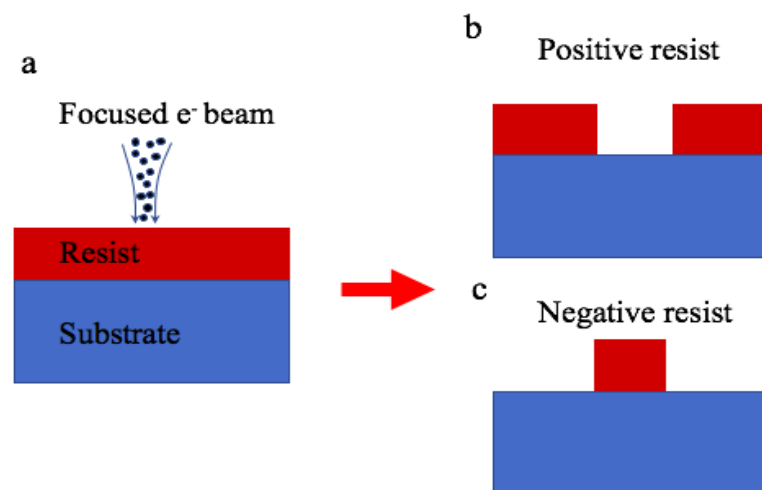
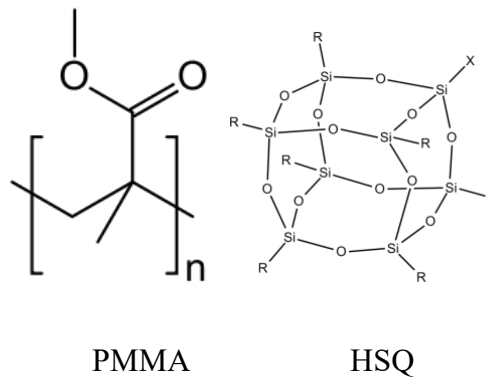


Figure 1: (a) electron beam exposure. (b) positive and (c) negative photoresist scheme [1].

The most common positive resist is based on Polymethylmethacrylate (PMMA); a common negative resist is based on Hydrogen silsesquioxane (HSQ).



Usually, the resist is deposited through the spin coating technique [4].

The EBL tool consists of a modified SEM system where an electron beam is focused on a thin film of the resist previously deposited on a substrate (Figure 2a). The crucial mechanism involved in the beam / resist interaction is the modification of the resist chemical properties (Figure 2b), indeed it polymerizes (solidifies by crosslinking) by becoming insoluble after the electron beam passage. This step allows us to define a 2D-pattern on it.

The radiated material (positive resist, Figure 2c) or the complementary (negative resist, Figure 1c) is selectively eliminated, by creating a contrast on the sample for pattern transfer. This step is defined *developing*; it consists, in the case of positive resist, in opening windows or pores (Figure 2c) in the photoresist in order to make the underlying substrate accessible. An etch resistant material can now be deposited, filling the pores (Figure 2d).

Afterwards the remaining resist can be easily removed with a washing step called stripping, using a proper solvent in which it is soluble (Figure 2e).

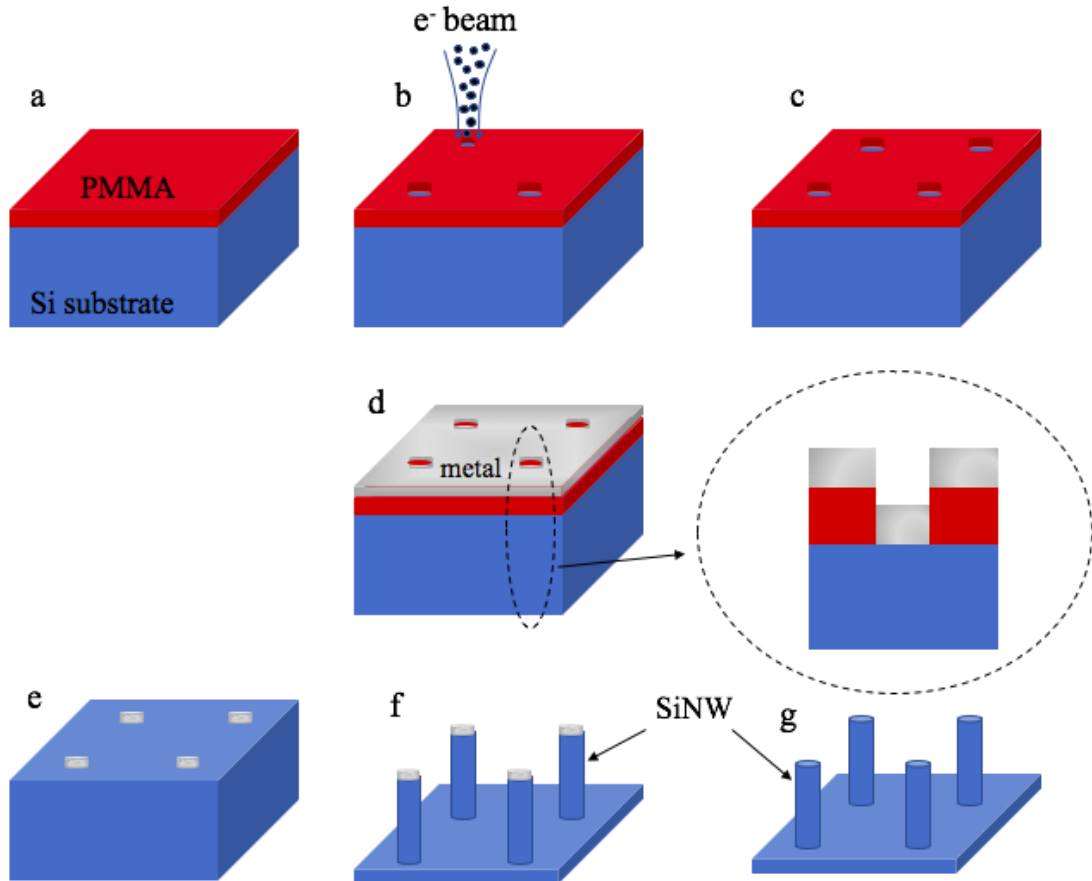


Figure 2: Schematic of EBL process coupled with the Reactive ions etching to obtain SiNWs [2].

The dot pattern of the hard mask (monodisperse particles) needed for the successive etching is finally ready and the sculpting of the nanowires, through RIE, can begin.

Typically, Al_2O_3 , Al, SiO_2 and SiN_x are used as hard masks for vertical Si nanowire fabrication [5].

Although the EBL has important advantages, such as high resolution, or the possibility of computer programming the beam path (and thus obtaining limitless and perfectly reproducible patterns), it also turns out to be impractical for mass production. Indeed, to generate the pattern the focused electron beam has to scan the resist surface point by point and it must dwell on each point for a sufficient time to modify the polymer characteristics. Although typically the beam needs only a few microseconds to write

one point, the entire process takes several minutes, making the technology unsuitable for production on an industrial scale.

RIE is a common type of dry etching, which erodes the substrate surface by exposing the system to an ion bombardment, usually obtained from a plasma of reactive gases, but not affecting the hard mask. The peculiarity of RIE is that it typically etches directionally, or anisotropically, along different crystal orientations (Figure 3c) [6].

Etching is defined as isotropic when its speed is the same vertically and horizontally ($r_v = r_H$) (Figure 3a); it is defined anisotropic when the vertical rate is different from the horizontal one ($r_v \neq r_H$); that is, the regime depends on the relationship:

$$R_L = \frac{r_H}{r_V}$$

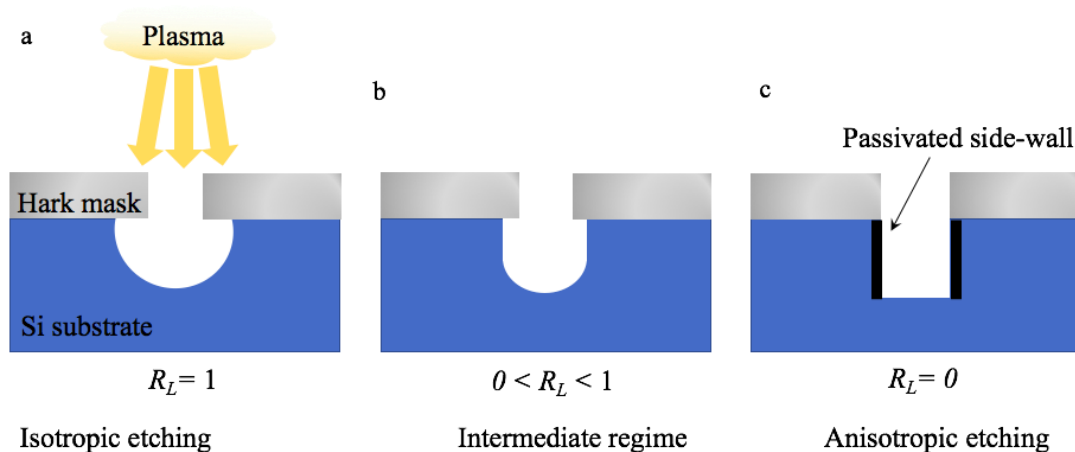


Figure 3: Comparison between isotropic etch (a) to anisotropic etch (c). (b) Intermediate regime [6].

The basis of RIE is simple: it uses a gas glow discharge to dissociate and ionize a gas, e.g. SF_6 for Si etching, free from hard mask, forming chemically reactive etching environment which consists of neutrals species, electrons, photons, radicals (F^\cdot), positive (SF_5^+) and negative (F^-) ions that react with the Si, resulting in its etching. The process provides successive etching and deposition cycles to coat the sidewalls (see arrow in Figure 3c) as etching progresses. Each cycle involves a typical ion bombardment and is followed with a deposition step of a chemically inert passivation layer (usually C_4F_8) on the newly exposed sidewalls, protecting them from reacting

with chemical species. Without the passivation layer on the sidewalls, the ions would react with substrate as deeper etches are made, leaving undesirable isotropic etch patterns [7].

The etch spontaneously produces volatile reaction products, SiF_4 , or their precursors, SiF_x ($x < 4$) so they can desorb from the etching surface into the bulk of the plasma and can be pumped out. At the end of this multistep process the SiNWs array is finally ready. A typical and satisfying result is shown in Figure 4.

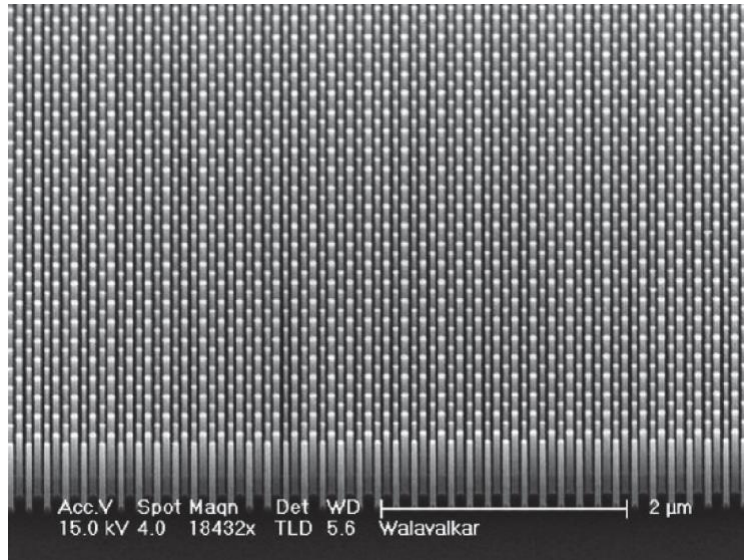


Figure 4: A tilted SEM micrograph of an array of EBL made Si NWs [8].

This technique however has some limitations, for example the fact that the final surface of the target is not always optimal (smooth and flat) but is damaged due to physical attack. Furthermore, the metals used for the masks are expensive (nickel, chrome or others).

1.3 Metal Assisted Chemical Etching

Metal-assisted chemical etching (MACetch) [9] is a valid electrochemical preparation technique of SiNWs. It is interesting since the chemical process occurs at room temperature. It provides for use of a Si substrate partially covered by noble metal nanoparticles or different shapes (Figure 5 a,c,e), typically of silver (Ag), that is subjected to an etchant solution made of HF and an oxidant agent as H_2O_2 . Si underneath the metal particle is etched faster than the Si without noble metal on top,

as a consequence, the metal and isolated cluster sinks into the Si substrate (Figure 5b) by generating pores and, with the proper shaped noble metals, Si wires (Figure 5d,f).

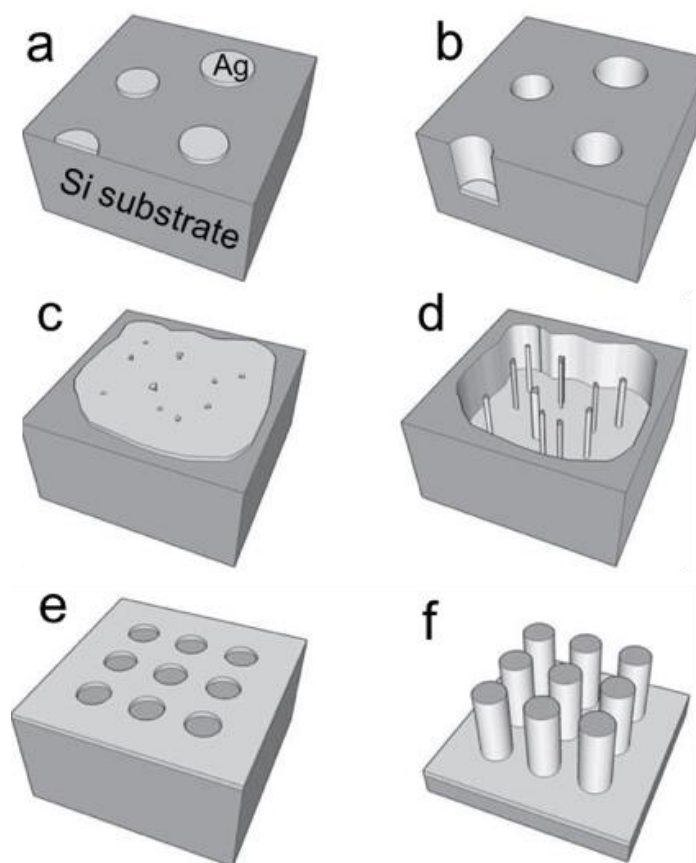


Figure 5: Scheme of typical morphologies of etched structures (right column) induced by metal catalysts with differently shaped noble metals (left column) [10].

The first process step is the metal deposition. The simplest way to achieve a deposition of metal nanoparticles on an Si substrate is to use a solution of metal salts [11-12]. Ag^+ ions in the vicinity of the Si surface withdraw electrons from Si and are deposited in the form of nano metallic Ag clusters. These Ag dots have strong catalytic activity and could provide a catalytic surface for the cathodic reaction (reduction of Ag ions). At this point the etching process starts according to the following scheme (Figure 6):

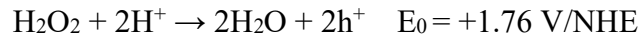
i) The oxidant is preferentially reduced at the surface of the noble metal, due to its catalytic activity on the reduction of the oxidant, the metal acts as a nano-cathode.

The proposed cathodic reactions in the absence of H_2O_2 are:

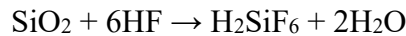
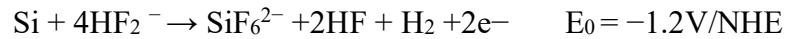
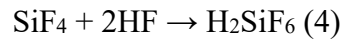




And in the presence of H_2O_2 [10]:



- ii) The holes generated due to the reduction of the oxidant diffuse through the noble metal and are injected into the Si that is in contact with the noble metal.
- iii) The Si is oxidized by the injected holes and dissolved at the Si/metal interface by HF. The reactant (HF) and the byproducts diffuse along the interface between the Si and the noble metal. There are several possible anode reactions for the dissolution process of Si [13]:



- iv) The concentration of holes has its maximum at the Si/metal interface. Therefore, the Si that is in contact with the metal is etched much faster by HF than a bare Si surface without metal coverage would be.
- v) If the rate of hole consumption at the Si/metal interface is smaller than the rate of hole injection, the holes diffuse from the Si under the noble metal to off-metal areas or to the wall of the pore. Accordingly, the off-metal areas or sidewalls of the pore may be etched and form microporous silicon and finally silicon nanowires.

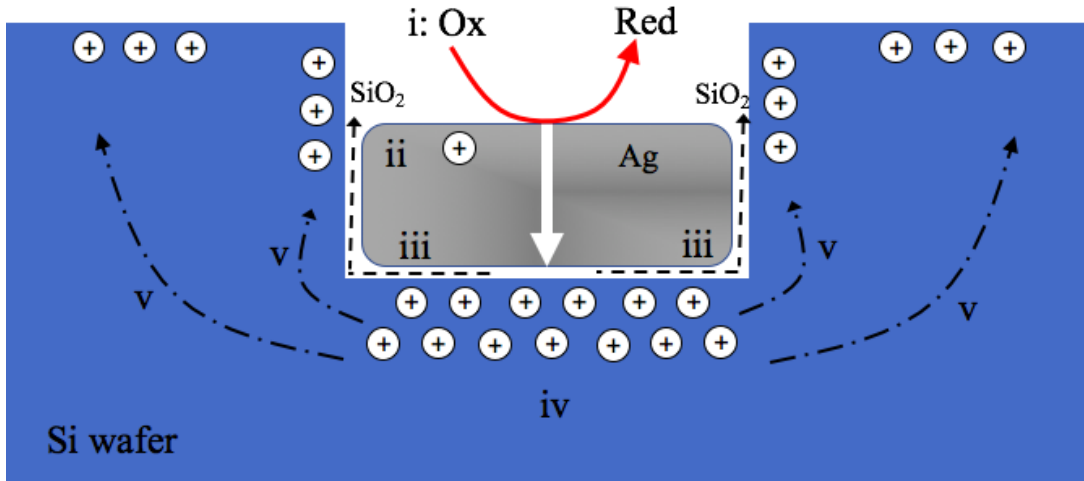


Figure 6: Scheme of processes involved in metal-assisted chemical etching of Si. The numbers indicate the steps mentioned in the text [10].

Unfortunately, after deposition on the Si substrate, dendritic structures of the metal are also formed [14]. These structures must be removed through additional chemical processes which are detrimental to both the optical and electrical properties of SiNWs.

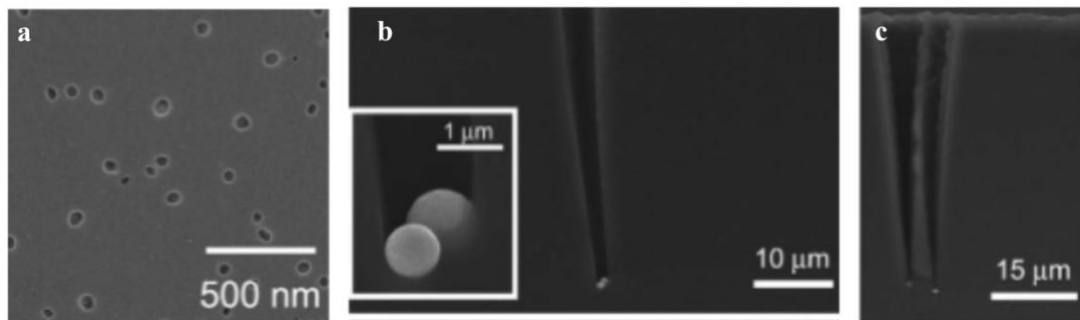


Figure 7: Typical morphologies of etched structures with: (a) Ag particle [15]. Copyright 2007, Elsevier. (b-c) Au particle [16] Copyright 2008, RSC.

Furthermore, by using an Ag mesh, since it can be slowly dissolved by the etching agent, new pores can form leading to unintentional silicon nanowires at the location of these pores. Moreover, there is a limitation to the size of the structures obtained by MACetch, due to the presence of a space charge of width W_{sc} localized at the solution / Si interface [17].

1.4 Principles of vapor liquid solid mechanism (VLS)

The most common and more efficient method to synthesize SiNWs, is the Vapor-Liquid-Solid (VLS). This is a bottom-up technique described for the first time by Wagner and Ellis in the '60s [18]. VLS is an unidirectional growth [19] that uses metallic particles as nano-catalysts for the NWs growth. The most efficient metal is gold. This method exploits the formation of a *eutectic* between silicon and certain metals, for instance Au, Cu, Pt, Zn, Sn.

An eutectic (from the Greek εὖ, eu- = good and τήκω, tēkō = to melt) is a liquid blend of elements or compounds whose melting point is lower than that of the single substances that compose it. The eutectic works as a catalyst (a substance that lowers the activation energy of a reaction increasing its speed, but remains unchanged at the end) in the VLS process for the growth of SiNWs.

The VLS techniques can be summarized in the following steps.

1. A thin (~1–10 nm) metal film is deposited onto a Si wafer substrate (typically by sputter deposition or thermal evaporation).
2. Then the wafer is annealed at temperatures higher than the metal-Si eutectic point, creating metal-Si alloy droplets on the wafer surface. The temperature at which the eutectic is formed is lower than the melting temperature of bulk silicon and of the bulk metal and this significantly lowers the energy required in the process.
3. At this stage a Si precursor from the vapor phase (V) is supplied, once decomposed, it releases the silicon atoms that are absorbed by the eutectic. The liquid alloy drop acts as 'catalyst' for this 1D growth, since it lowers the activation energy for the precursor breaking allowing the reaction to occur just on top of it.
4. Now these atoms can diffuse into the liquid phase (L), which is formed at the Si/metal interface, until the supersaturation.
5. At this point the Si begins to precipitate out of the supersaturated liquid-alloy droplet at the liquid-alloy/solid-Si interface, because it has a much higher melting point (~1414 °C) than that of the eutectic alloy (~363 °C for Au/Si);
6. The nucleation occurs and the growth of the nanowires starts (S) rising the droplet from the surface.

During the growth the interface between Si and the metal continuously shifts and the NW can grow axially [20].

At the end of the process the gold dot rests linked at the NW tip, proving that the growth mechanism is that just described.

Figure 8 sketches the described steps.

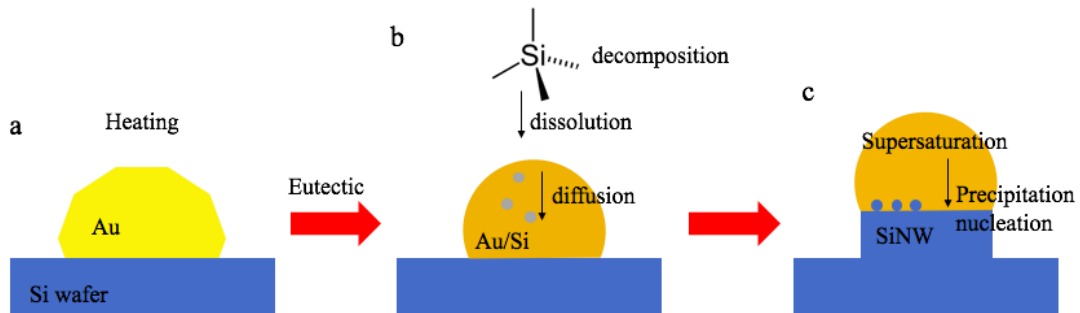


Figure 8: Schematic illustration of metal-alloy catalyzed SiNWs growth depicting the pathway of source materials through the droplet to the growing interface [18].

It should be highlighted that the droplet size of the liquid catalyst is a key parameter to control the NW diameter [21]. The thicker is the initial metal film deposited, the larger the alloy droplets.

The drop should wet the solid substrate surface with a contact angle (β_0 , the angle subtended by the liquid at the line where it meets the solid) less than 90° (see Figure 9).

The actual conditions during growth are very difficult to measure experimentally, the droplet dimensions can be mathematically described.

The shape and dimension of the liquid particle are determined by a balance of surface forces, surface tension at the liquid-vapor (σ_{VL}) and the liquid–solid (σ_{VS}) interfaces. The radius of the droplet depends on the contact angle (β_0) [22-23].

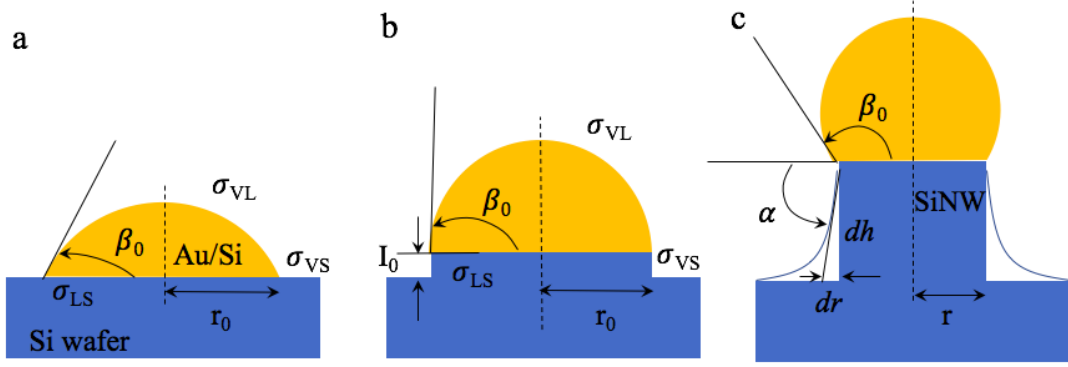


Figure 9: Scheme of the initial stage of crystal growth of a columnar crystal via the VLS mechanism. Schematic illustration of metal-alloy catalyzed wire growth depicting the catalyst droplet formation during the early stages of whisker growth [23].

The NW diameter depends on the properties of the alloy drop. The growth of nano-sized wires requires the presence of nano-sized droplets on the substrate. It is demonstrated that the minimum radius of a metal drop is given by [24]:

$$R_{min} = \frac{2V_l}{RT \ln(s)} \sigma_{lv}$$

Where V_l is the molar volume of the droplet and s is the degree of supersaturation [25] of the vapor. This relation shows that, under equilibrium conditions, a critical diameter of the droplet exists, below this critical diameter the growth is impossible. This limitation is related to surface curvature and depends on surface tension (the Gibbs-Thompson effect) [26]. Au-catalyzed growth of Si NWs with diameters below 10 nm was observed when the seeds were as small as 3 nm [27]. This is considered to be the thermodynamically allowed minimum diameter for the VLS growth mode [28].

As a nanowire begins to grow (I_0), its height increases by an amount dh and the radius of the contact area decreases by an amount dr (see Figure 9 c). As the growth continues, β_0 and the inclination angle at the base of the nanowires (α , set as zero before whisker growth) increase.

The kinetics of NWs growth is discussed in the classic work of Givargizov [29]. The SiNWs growth rate is dependent on the supersaturation of the metal-alloy catalyst that

is the main driving force. The smaller is the drop diameter, the smaller is the driving force of the process; therefore, the larger is the whisker diameter, the faster the nanowire grows axially.

The process rate can be adjusted by acting on the temperature and the degree of supersaturation.

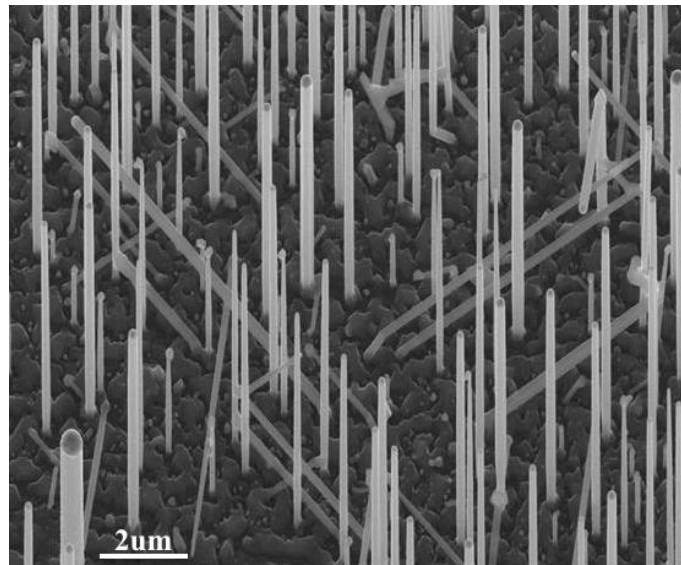


Figure 10: Si NWs ARRAY fabricated by VLS, some are slanting with respect to the surface [30].

SiNWs growth direction, and thus their final orientation, is strongly influenced by the surficial crystal structure of the substrate. The final length of the wires can be tuned by simply extending or decreasing the growth time since the growth stops by deactivating the supply of the silicon gas precursor into the reaction chamber. The typical aspect of a SiNWs array obtained by the VLS process is shown in Figure 10.

Gold is the most widespread metallic catalyst to produce nanowires through the VLS process, because it allows:

- low eutectic temperature (363°C),
- easily formation of alloys with silicon precursors (SiH_4 or Si_2H_6),
- rapid inter-diffusion of Si into Au,
- chemical inertness.

Au has to be present on the surface of the substrate in nanoparticle form to be useful for the growth. It can be prepared in many ways: as an evaporated, as colloidal nanoparticles or, as sputtered thin film followed by a thermal annealing.

However, Au also suffers some issues; for instance, its presence introduces defects in the NW final structure. A drawback of VLS-type grown Si NWs is diffusion of metal from the droplet into the wire during the Si NWs growth at the VLS growth temperature, as shown in the TEM image of Figure 11.

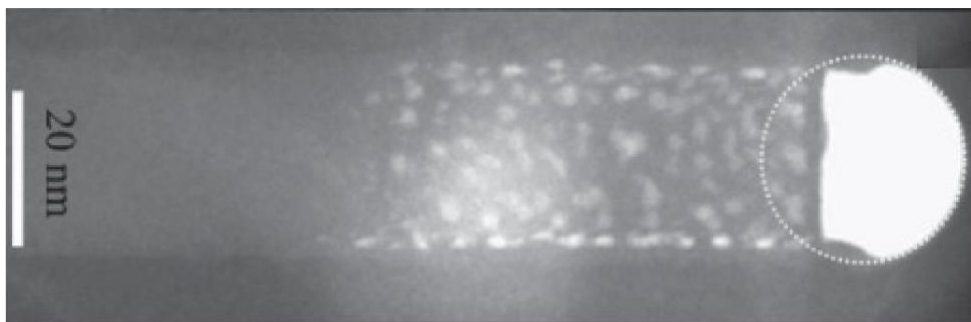


Figure 11: A dark field TEM image showing the gold diffusion from the droplet into the VLS type NW during the growth [31].

We will see in a later section of this manuscript how this limitation was addressed and solved in a non-invasive way.

The Si/Au ratio of the alloy is a most important parameter for the growth as said. This percentage of Si/Au is described by the binary alloy phase diagram (blue curve).

A phase diagram (see Figure 12 for the Au/Si binary system) is a graph referred to a pure substance or a blend in which each point represents a phase (or state), where by 'phase' we mean that part of the system having constant chemical and physical characteristics, in which the system can be found when two or more thermodynamic quantities (like Temperature, Pressure, Volume, composition n) vary. In the phase diagram the eutectic is identified by a point that corresponds to an invariant liquid equilibrium. A eutectic mixture, at a certain constant pressure value, is characterized by a well determined weight ratio between its constituents and by a well-defined temperature [32]. Hence, the knowledge of phase diagrams is a fundamental prerequisite to set the experimental conditions.

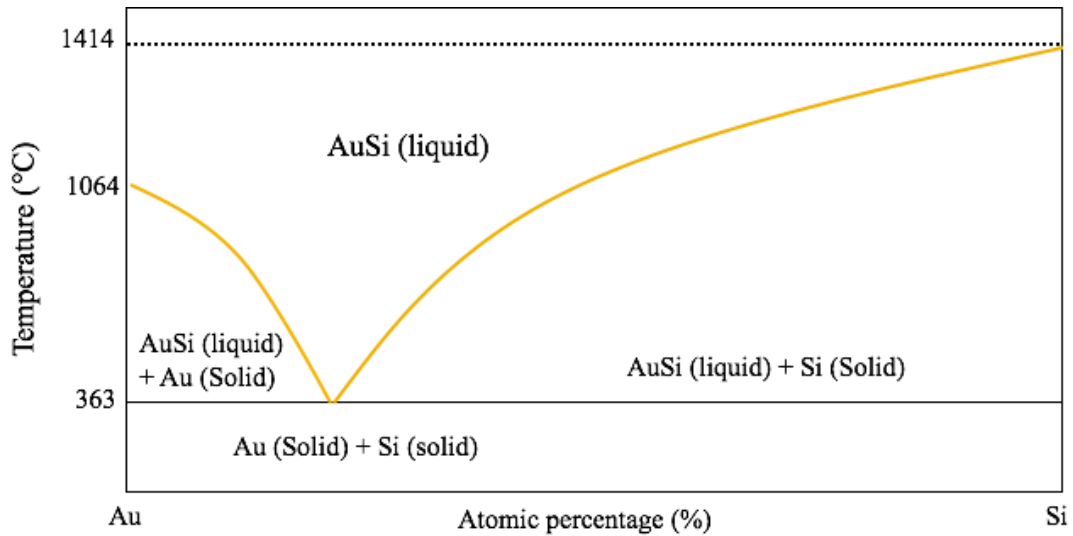


Figure 12: Phase diagram of Au/Si system [32].

The region in Figure 12 below the yellow curve is the silicon supersaturation zone, corresponding to a temperature over 363° C and a Si percentage higher than 18.6%. Only in these thermodynamic conditions the SiNW growth occurs, because only in this case the Si atoms, adsorbed by the vapor phase into the liquid eutectic, can precipitate at the alloy/substrate interface [33]. The supersaturation condition in VLS mechanism involves Si atoms absorption from the vapor phase and Si ad-atoms diffusion from the Si surface of the substrate through the sidewalls of the NWs. These mechanisms are schematized in Figure 13; they do not have the same weight in the process.

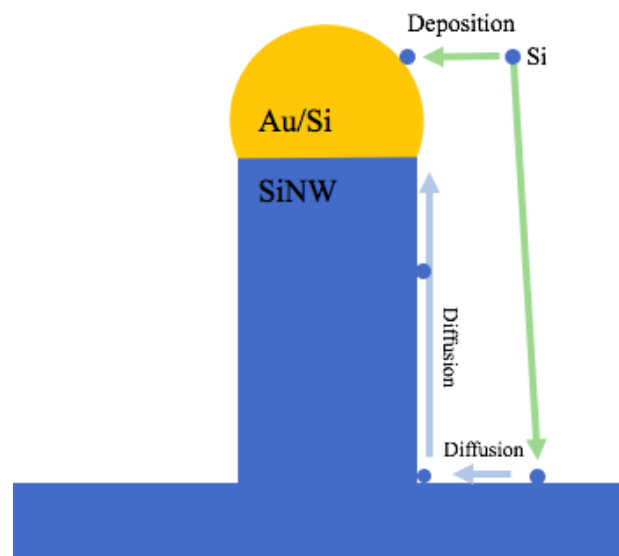


Figure 13: (a) Gold/silicon alloy binary phase diagram. (b) VLS growth process of Si NWs [34].

For instance, in the physical vapor deposition (PVD) techniques, such as evaporation, sputtering, sublimation, Molecular Beam Epitaxy (MBE) [35] and Electron Beam Evaporation (EBE) [36], the contribution to supersaturation by the diffusion of ad-atoms is prevalent; while in the chemical vapor deposition (CVD) techniques the Si atoms absorption from the vapor phase is the main one.

In this thesis the use of the CVD technique was chosen for the synthesis of SiNWs via VLS. The principles of this technique are described below.

1.5 Principles of Chemical Vapor Deposition (CVD)

Chemical vapor deposition (CVD) is defined as a process whereby, by a chemical reaction a deposit (generally a thin solid film [37]) is synthesized from gaseous phase with different characteristics:

- Epitaxial layers;
- Amorphous layers;
- Polycrystalline layers;
- Polymeric materials.

CVD is a reactive process that distinguishes it from physical deposition processes in which no chemical reaction occurs. CVD has some advantages over PVD techniques, namely:

- High deposition rate
- Conformal step coverage
- Capability to coat complex shapes
- Adaptability to large scale processing
- Simplified apparatus

CVD is a very versatile technique because it not only allows depositing thin films but also producing nanostructures of several materials and shapes and it has become the most common technique for SiNWs VLS growth. This is because it allows to have:

- high yield
- high growth rate
- morphology control
- crystalline and straight wires
- controllable diameter dimensions
- controllable length
- quantum size diameters (even below 5 nm)

Moreover, CVD is a bottom-up technique and allows in situ doping during the growth of the nanowire structure.

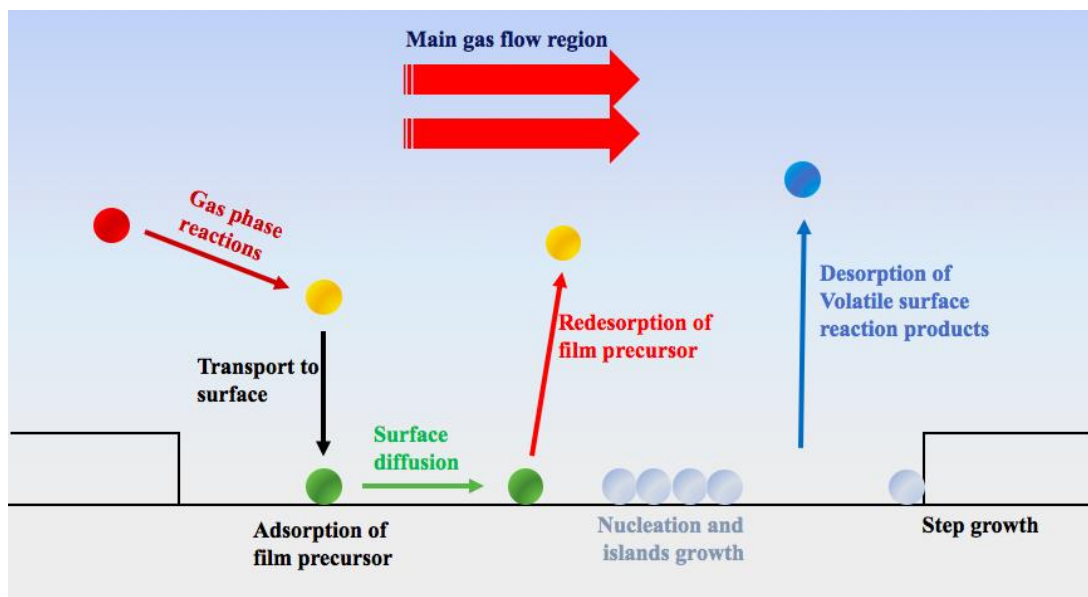


Figure 14: Representation of the transport and reaction process in a CVD deposition [37].

One relevant issue of SiNWs grown by CVD is that they exhibit a certain variation of the growth direction [38]. This aspect, however, is overcome when the nanowires are grown in a template, such as anodic aluminum oxide (AAO) [39]. In this method the metal catalyst is deposited into the pores of an AAO membrane, so that wire growth is confined into it. Thereby, the wire is forced to grow along the pore direction. For SiNWs grown through CVD, a wafer of Si, with gold droplets deposited on top, is introduced into a CVD reactor with a pressure between 10^{-8} and 10^{-4} Torr. Then the system is heated up to the growth temperature (363° C), and at this point a transfer gas is introduced into the reaction chamber, generally Ar, but H_2 or N_2 can also be used.

Now the precursor gas is introduced into the reactor, to provide chemical species that have to be deposited, silicon in our case. The precursor gas partial pressure spans between 10^{-5} and 1 Torr, while the total pressure can be from one up to three orders of magnitude more. The main mechanisms involved in the CVD process are depicted in Figure 14.

Metal-organic precursors are often used in solution phase and supercritical fluid phase which makes their use difficult and expensive. More versatile precursors typically used in the CVD depositions are metal hydride, since this compound family exists as a gas phase at room temperature [40]. Among the metal hydrides, we chose the silane (SiH_4). At the interface between the metallic droplet and the vapor phase, the following reaction occurs:



Overall stoichiometric equations for CVD processes are considerably complex. A simplified reaction scheme which takes in account the main gas-phase reactions for polysilicon deposition from silane occurring in a general CVD process is shown in Figure 15.

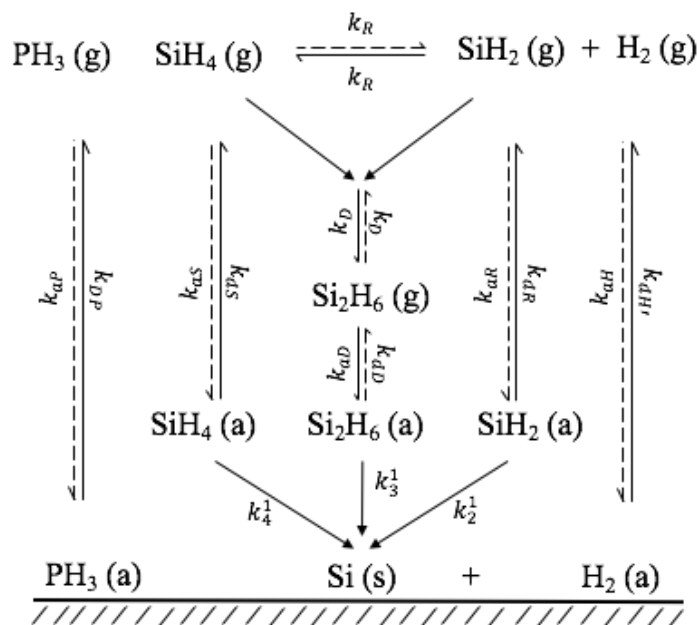


Figure 15: Reaction scheme for Si deposition (Hitchman et al., 1987).

The chemical reactions involved in the growth of SiNWs growth, and in general in any CVD process, need energy to occur. We can identify the following processes:

- gas phase reactions;
- adsorption/desorption processes;
- surface diffusion;
- surface reactions;
- nucleation;
- growth;

A non-catalyzed CVD process allows different nucleation and growth modes that take place on the surface of the bare substrate and can be classified as follows:

- Island growth or Volmer-Weber growth;
- layer-plus-island growth or Stransky-Krastanov growth;
- layer-by-layer growth or Franck-van der Merwe growth.

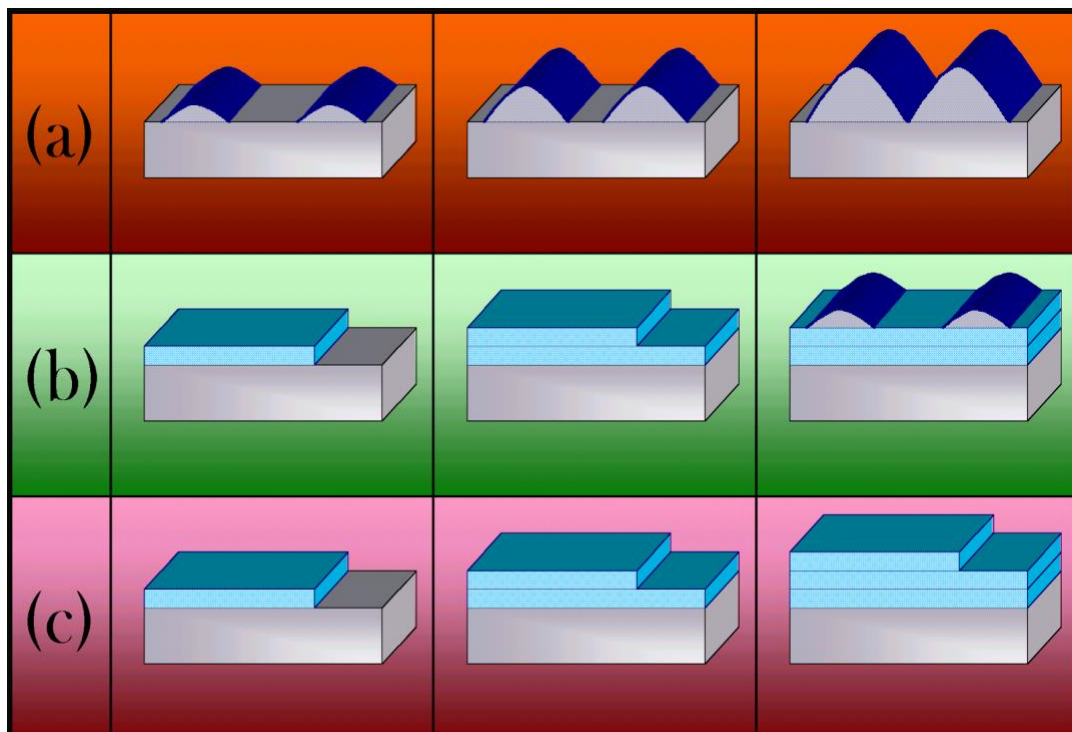


Figure 16: Possible growth mechanism in a CVD process: Island growth or Volmer-Weber growth (a); layer-plus-island growth or Stransky-Krastanov growth (b); layer-by-layer growth or Franck-van der Merwe growth (c) [41].

In the island growth, small clusters nucleate directly on the substrate surface; this mechanism occurs when the atoms of the material to be deposited have a greater affinity to form bonds with atoms of its own element than atoms of the substrate. In this case the product grows into islands, which eventually coalesce to form a continuous film. Two-dimensional layer-by-layer growth occurs when the film atoms are equally or less strongly bonded to each other than to the substrate. The layer plus island growth is a combination of the other growth modes. After a certain number of monolayers, i.e. exceeding a certain thickness, the growth per layer becomes unfavorable and the islands are formed above the initial layers [41].

A variety of derivatives of CVD methods exist. These can be classified by parameters such as the base and operation pressure or the method used to supply energy.

The chemical reactions involved in a CVD can be activated in different ways. Depending on the energy input method we distinguish different CVD processes:

- **Thermal CVD** if heat is used;
- **Plasma CVD**, known as plasma-enhanced CVD (PECVD) or plasma-assisted CVD (PACVD) if using a plasma;
- **Photo CVD** if using UV or laser lamps (LCVD);
- **Acoustic CVD** when using pressure waves.

Another distinction related to CVD processes is based on operating conditions:

- **Atmospheric pressure CVD (APCVD)**;
- **Reduced pressure CVD (RPCVD)**: typical pressure range 100 Torr-1Torr;
- **Low Pressure CVD (LPCVD)**: typical pressure range 1 Torr-10 mTorr;
- **Ultrahigh vacuum CVD (UHVCVD)**.

Furthermore, the configuration of the CVD reactor system is not fixed and depending on the geometry of the reaction chamber we have:

- **Horizontal reactors**;
- **Vertical reactors**;
- **Industrial reactors**.

As mentioned In a CVD process two types of growth can take place: not-catalyzed (2D) and catalyzed (1D). As revealed by the SEM in Figure 17.

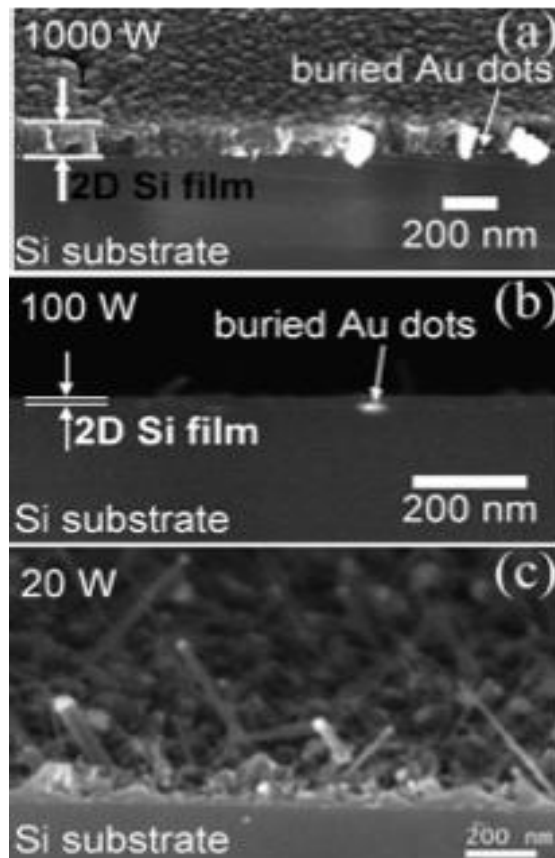


Figure 17: Sequence of SEM micrographs in cross view on samples deposited at 1000W (a), 100W (b), and 20W (c) for 15min [42].

At the low temperature adopted for catalytic SiNWs growth (c.a. 360°C), the probability that the non-catalyzed chemical reactions occur at the bare substrate surface is generally low. This causes the NW to grow faster than the substrate where a two-dimensional film would be made. [36, 43].

However, the temperature is not the only determining parameter in influencing the type of growth. For instance, in a plasma-based tool (PECVD), the plasma power plays a key role in influencing the growth. The graph in Figure 18 reports the growth rate of NWs as a function of the plasma power [42]. Three regions can be identified: the low plasma power region from 0 up to 60 W, where only the 1D growth is obtained and the 2D growth is suppressed. Here the growth rate presents a maximum value of about 17 nm/min at about 20 W; an intermediate region at 100 W where both 1D and 2D growth are present; a third region at high power, at 1000 W, where the 1D growth is

absent and continuous films are grown. The line is a guide to the eye. It has been found that at 20 W, the NWs formation process is most efficient.

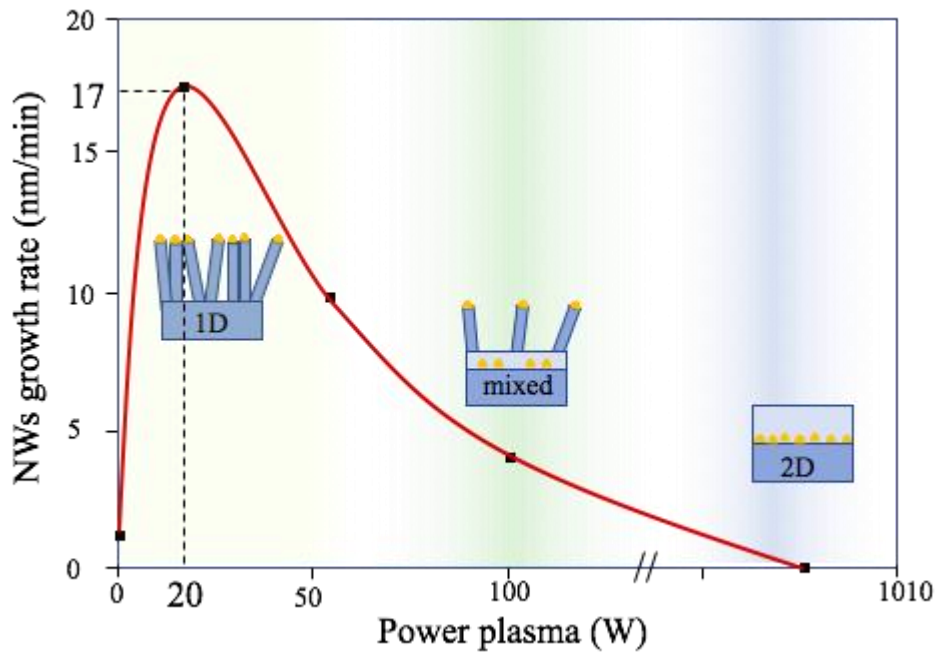
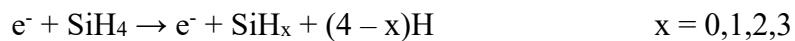
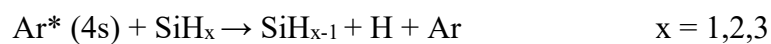


Figure 18: SiNWs growth rate vs the plasma power. Three regions are identified: the low plasma power (1D growth); intermediate plasma power (simultaneously 1D and 2D growth); high plasma power (2D growth) [42].

To understand this evidence the authors considered the chemistry of plasma constituted by the gas carrier and the vapor precursor (Ar/ SiH₄). At low power the dissociation reactions of the SiH₄ due to the electron impact are the most relevant:



However, when P increases radical-radical reactions become progressively more important. In particular the excitation transfer reactions:



It can be observed that the experimental conditions when the uncatalyzed deposition is suppressed, i.e., $P = 0 - 60$ W (Figure 18), are in the power range when the density of excited species (of $x < 3$ radicals) is low .

The uncatalyzed growth requires the presence of a high concentration of very reactive species, and the abundance of such species, like radicals and of Ar^* and Ar^{**} excited atoms increase rapidly with the plasma power. Since the type of growth depends on the concentration of reactive species and since the concentration of these in turn depends on the plasma power, the growth regime also depends on the plasma power. The SEM image depicted in Figure 19 shows an example of typical Au-catalyzed SiNWs grown by CVD technique on a (111) Si substrate at 360-390 °C by using an atmosphere SiH_4 as precursor obtained after suppression of not-catalyzed growth.

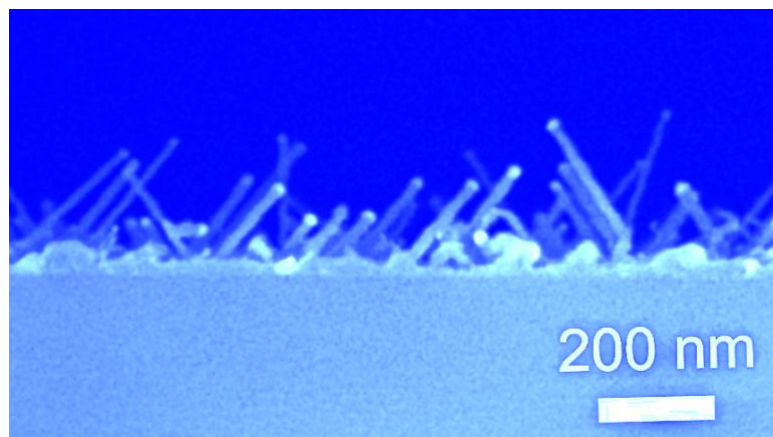


Figure 19: typical SiNWs array grown by CVD technique on a (111) Si substrate at 360-390 °C by using an atmosphere SiH_4 as precursor by suppressing the non-catalyzed 2D growth.

1.6 SiNWs applications

Silicon nanowires find applications in several fields, charge trapping behavior and tunable transport properties of SiNWs make this kind of nanostructures very interesting. They find application in many fields of newest technology such as field effect transistors [44], catalysis [45] chemical or biological sensors [46], energy conversion [47, 48] or energy storage. In this latter play a key role is the ability for lithium ions to intercalate into Si making SiNWs suitable for anodes in Li-ion batteries (LiBs). Concerning this application, it should be noted that SiNWs exhibit significant lithiation while maintaining structural integrity and electrical connectivity [49]. Still in nano-optics as resonant nanocavities, exploiting their plasmons to obtain lasers

[50]. Also, flash memory [51] and logic devices [52] are fields of application of SiNWs.

1.7 Conclusions

This chapter began by looking at some of the aspects that make the nanoworld increasingly interesting by analyzing the reasons why nanostructures in general and silicon nanowires in particular are so useful. Thanks to the material they are made of, and to their elongated shape, these interesting one-dimensional nanosystems find applications in many fields of science and technology. The most widespread and convenient methods for their synthesis were discussed focusing on the chemical vapor deposition / vapor liquid solid technique as it is the one chosen for their production in this thesis work. Theoretical aspects such as the thermodynamics and kinetics of some of the processes involved were also briefly addressed, discussing their advantages and disadvantages.

Bibliography

- [1] J. K. W. Yang et al. - Understanding of hydrogen silsesquioxane electron resist for sub-5-nm-half-pitch lithography - *Journal of Vacuum Science and Technology B* (2009) vol. 27 p. 2622
- [2] S. Walavalkar et al. - Tunable visible and near-IR emission from sub-10 nm etched single-crystal Si nanopillars - *Nano Letters* (2010) vol. 10 p. 4423
- [3] I. Haller, M. Hatzakis, R. Srinivasan. (1968). High resolution positive resists for Electron beam exposure. *IBM Journal*
- [4] Tyona, M. D. "A theoretical study on spin coating technique." *Advances in materials Research* 2.4 (2013): 195
- [5] M. Henry et al.- Alumina etch masks for fabrication of high- aspect-ratio silicon micropillars and nanopillars - *Nanotechnology* (2009) vol. 20 p. 4
- [6] *J. Micromech. Microeng.* 6 (1996) 14–28
- [7] F. Roozeboom et al 2015 *ECS J. Solid State Sci. Technol.* 4 N5067
- [8] S. Walavalkar et al. - Tunable visible and near-IR emission from sub-10 nm etched single-crystal Si nanopillars - *Nano Letters* (2010) vol. 10 p. 4423
- [9] D. D. Malinovska et al. - Preparation of thin porous silicon layers by stain etching - *Thin Solid Films* (1997) vol. 297 p. 9
- [10] Z. Huang et al. - Metal-assisted chemical etching of silicon: a review - *Advanced Materials* (2011) vol. 23 p. 285
- [11] K. Q. Peng et al. - Metal-particle-induced, highly localized site-specific etching of Si and formation of single-crystalline Si nanowires in aqueous fluoride solution - *Chemistry European Journal* (2006) vol. 12 p. 7942
- [12] K. Q. Peng et al. - Simultaneous gold deposition and formation of silicon nanowire arrays - *Journal of Electroanalytic Chemistry* (2003) vol. 558 p. 35
- [13] Z. Huang et al. - Metal-assisted chemical etching of silicon: a review - *Advanced Materials* (2011) vol. 23 p. 285
- [14] K. Q. Peng et al. - Metal-particle-induced, highly localized site-specific etching of Si and formation of single-crystalline Si nanowires in aqueous fluoride solution - *Chemistry European Journal* (2006) vol. 12 p. 7942
- [15] K. Tsujino, M. Matsumura, *Electrochim. Acta* 2007, 53, 28]
- [16] C. L. Lee, K. Tsujino, Y. Kanda, S. Ikeda, M. Matsumura, *J. Mater. Chem.* 2008, 18, 1015

- [17] Z. Huang et al. - Metal-assisted chemical etching of silicon: a review - *Advanced Materials* (2011) vol. 23 p. 285
- [18] R. Wagner et al. - Vapour-liquid-solid mechanism of single crystal growth - *Applied Physics Letters* (1964) vol. 4, p. 89
- [19] B. A. Wacaser - Preferential Interface Nucleation: An Expansion of the VLS Growth Mechanism for Nanowires - *Advanced Materials* (2009) vol. 21 p. 153
- [20] R. Wagner et al. - Vapour-liquid-solid mechanism of single crystal growth - *Applied Physics Letters* (1964) vol. 4, p. 89
- [21] S. Barth et al.- Defect transfer from nanoparticles to nanowires - *Nano Letters* (2011) vol. 11 p. 1550
- [22] Rogachev AS, Mukasyan AS. *Combustion for materials synthesis*. New York, NY: CRC Press/Taylor & Francis; 2015 p. 44–204
- [23] Mukasyan, Alexander S. "Vapor-Liquid-Solid Mechanism of Structure Formation." *Concise Encyclopedia of Self-Propagating High-Temperature Synthesis*. Elsevier, 2017. 418-420
- [24] Wang, Ji-Tao (2002). *Nonequilibrium Nondissipative Thermodynamics: With Application to Low-pressure Diamond Synthesis*. Berlin: Springer Verlag. p. 65.
- [25] Wang, Ji-Tao (2002). *Nonequilibrium Nondissipative Thermodynamics: With Application to Low-pressure Diamond Synthesis*. Berlin: Springer Verlag. p. 65.
- [26] Mukasyan, Alexander S. "Vapor-Liquid-Solid Mechanism of Structure Formation." *Concise Encyclopedia of Self-Propagating High-Temperature Synthesis*. Elsevier, 2017. 418-420
- [27] Y. Wu et al. - Controlled growth and structures of molecular-scale silicon nanowires - *Nano Letters* (2004) vol. 4 p. 433
- [28] T. Y. Tan et al. - On the thermodynamic size limit of nanowires grown by the vapor-liquid-solid process - *Applied Physics A* (2004) vol. 78 p. 519
- [29] Givargizov EI. Fundamental aspects of VLS growth. *J Cryst Growth* 1975;31:20–30
- [30] Hourlier, Djamilia, and Pierre Perrot. "Au-Si and Au-Ge phases diagrams for nanosystems." *Materials Science Forum*. Vol. 653. Trans Tech Publications Ltd, 2010
- [31] M. Den Hertog et al. - Control of gold surface diffusion on si nanowires - *Nano Letters* (2008) vol. 8 p. 1544

- [32] Croker, M. N., R. S. Fidler, and R. W. Smith. "The characterization of eutectic structures." *Proceedings of the Royal Society of London. A. Mathematical and Physical Sciences* 335.1600 (1973): 15-37
- [33] Growth and Characterisation of Gold-seeded Indium Gallium Arsenide Nanowires for Optoelectronic Applications phd thesis Amira Saryati Ameruddin
- [34] V. Dubrovskii et al. - Growth kinetics and crystal structure of semiconductor nanowires - *Physical Review B* (2008) vol. 78 p. 235301
- [35] L. Schubert et al. - Silicon nanowhiskers grown on (111)Si substrates by molecular beam epitaxy - *Applied Physics Letters* (2004) vol. 84 p. 4968
- [36] A. Irrera et al. - Control of growth mechanisms and orientation in epitaxial Si nanowires grown by electron beam evaporation - *Nanotechnology* (2009) vol. 20 p. 135601
- [37] binti Hamzan, Najwa, et al. "Controlled physical properties and growth mechanism of manganese silicide nanorods." *Journal of Alloys and Compounds* 851 (2021): 156693
- [38] *Nano Lett.* 2005, 5, 5, 931–935
- [39] Shimizu, Tomohiro, et al. "Synthesis of vertical high-density epitaxial Si (100) nanowire arrays on a Si (100) substrate using an anodic aluminum oxide template." *Advanced Materials* 19.7 (2007): 917-920
- [40] W. Lu et al. - One-dimensional hole gas in germanium/silicon nanowire heterostructures - *Proceedings in National Academic Science U.S.A.* (2005) vol. 102 p. 10046
- [41] Wearing, Lisa. *Formation of metallic overlayers on quasicrystal surfaces.* The University of Liverpool (United Kingdom), 2008
- [42] Garozzo, C et al., *Journal of Applied Physics*, 113(21), 214313 (2013)
- [43] N. D. Zakharov et al. - Growth phenomena of Si and Si/Ge nanowires on Si (111) by molecular beam epitaxy - *Journal of Crystal Growth* (2006) vol. 290 p. 6
- [44] Hofheinz, M., et al. "Simple and controlled single electron transistor based on doping modulation in silicon nanowires." *Applied physics letters* 89.14 (2006): 143504
- [45] *Appl. Catal. B* 184: 258-263 (2016)
- [46] Ouhibi, Awatef, et al. "Functionalized SERS substrate based on silicon nanowires for rapid detection of prostate specific antigen." *Sensors and Actuators B: Chemical* 330 (2021): 129352

- [47] Sahoo, Mihir Kumar, and Paresh Kale. "Integration of silicon nanowires in solar cell structure for efficiency enhancement: A review." *Journal of Materiomics* 5.1 (2019): 34-48
- [48] Puglisi, Rosaria A., et al. "Molecular doping applied to Si nanowires array based solar cells." *Solar Energy Materials and Solar Cells* 132 (2015): 118-122
- [49] Chan, C., Peng, H., Liu, G. *et al.* High-performance lithium battery anodes using silicon nanowires. *Nature Nanotech* 3, 31–35 (2008).
<https://doi.org/10.1038/nnano.2007.411>
- [50] *Nanophotonics* 8.12: 2091-2110 (2019)
- [51] Mikolajick, Thomas; Heinzig, Andre; Trommer, Jens; et al. (2013). "Silicon nanowires—a versatile technology platform". *Physica Status Solidi RRL*. 7 (10): 793–799. [Bibcode:2013PSSRR...7..793M](#). [doi:10.1002/pssr.201307247](#)
- [52] Daniel, Shir; et al. (2006). "Oxidation of silicon nanowires". *Journal of Vacuum Science & Technology*. 24 (3): 1333–1336. [Bibcode:2006JVSTB..24.1333S](#). [doi:10.1116/1.2198847](#)

Chapter 2

Introduction to Plasmon Resonance (PR)

At optical frequencies the free electrons of a conductive material, like a metal, behave as a plasma, a charged particle gas globally neutral. For this reason, in certain contexts these are named plasmonic materials. Plasma is the most common state of matter in the universe, found in stellar nebulae, lightning, stars, flames, and the outer earth's atmosphere. A plasma can absorb energy, get excited and swing collectively. To this excitation a quantum is associated: the plasmon, i.e. a quasiparticle resulting from the quantization of plasma oscillations. The existence of plasmons is peculiar to the interaction of metal with optical radiation so that the term plasmonic automatically calls to mind metals. Nevertheless, semiconductors can also support plasmons. Plasmonics in semiconductors is taking an increasingly prominent role in the optoelectronic field [1, 2]. Already from the past decade surface plasmon resonance (SPR) at semiconductor/dielectric interfaces have received considerable interest, since the use of a semiconductor/dielectric interface to support optical plasmons has been shown possible [3]. SiNWs also support plasmon resonance (PR) [4].

Historically, PR is that electromagnetic phenomenon first understood by the physicist W. Otto in 1968 [5]. It is the response of the electron plasma motion to a perturbation of the charge distribution. It can be imaged as a coupling between an external oscillating force (the incident electromagnetic field with right features), and the collective oscillations of electrons.

PR is a versatile phenomenon because it is tunable by modulating the nanosystem geometry, the medium covering or surrounding it and its shape. Its wide versatility is also due to the fact that PR dramatically enhances the local electrical field, by concentrating electromagnetic energies into subwavelength volumes. [6,7].

When PR is inducted in nanostructures, electromagnetic energy is harvested, confined at the nanoscale and locally amplified by several orders of magnitude. These very special features allows a wide spectrum of interesting optical applications like imaging below the standard diffraction limit [8], efficient optical mixing [9], fluorescence [10] Raman scattering [11], absorption and circular dichroism [12] single molecule

detection [13]. Moreover, PR can catalyze chemical reactions [14]; in mechanical it allows manipulation of nano objects [15]; it is useful also in nanomedicine because it makes possible, for instance, selective heating of nanoscale areas and enhanced near-field heat transfer [16]. PR is also useful in photovoltaics; indeed, it is an effective solution to increase the photoconversion efficiency of solar cells thanks to its photon-harvesting action [17]. It should be noted that the term plasmon resonance refers to different kinds of excitations. Indeed, free electrons collective motions in a plasma can exist in 3D (bulk plasmon) and 2D at the interface between two media (surface plasmon SPR). Finally, plasmons can be confined into a nanostructure, producing the so-called “localized surface plasmon resonance” (LSPR).

2.1 Lorentz model

A general model to describe plasmon resonance in solids involves the understanding of material’s interaction with electromagnetic radiation. The Drude model proposed by Paul Drude in 1900 is the most common approach to explain the transport properties of electrons in metals. It considers the valence electrons of the atoms to be free and allows to define some physical quantities involved in the material/electromagnetic waves interaction such as the dipole moment, the polarization, the susceptibility, the dielectric function and the resonance plasma frequency.

The equation describing the motion of a free electron in a metal subjected to an external electric field \mathbf{E} is:

$$m\ddot{\mathbf{x}} + m\gamma\dot{\mathbf{x}} = q\mathbf{E}.$$

where q is the electron charge, m is the effective mass of the electron.

Now we suppose the electron is connected to the nucleus via a hypothetical spring with elastic constant c i.e. that the electron is subjected to a recall elastic-type force by adding in the last equation this elastic term ($-c\mathbf{x}$). We compare the system to a damped harmonic oscillator. The model can describe bounded electrons and thus it becomes suitable for the description of insulators and semiconductors.

Semiconductors can also support SPPs when free carriers are excited either thermally or by doping, with a resulting plasma frequency typically in the terahertz (THz) domain. [18].

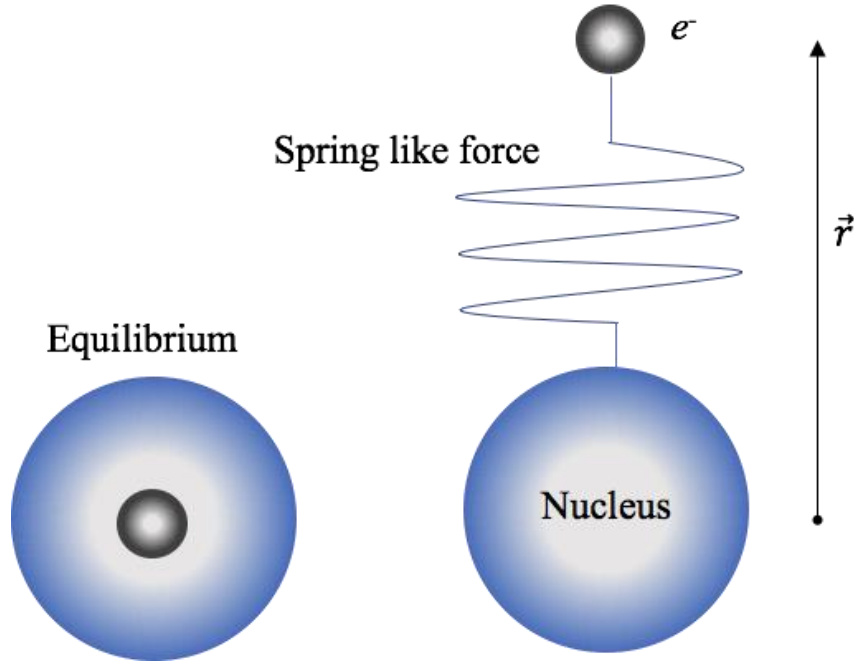


Figure 1: An atom in equilibrium (a) and after the action of a perturbing force (b).

Consider an atom whose centers of positive charge, given by the nucleus, and negative charge, given by the electrons, are initially coincident, at the center of the atom itself (Figure 1a). Now assume that each electron is subjected to a perturbation due to an oscillating electric field:

$$E = E_0 \cos(-\omega t)$$

Electrons are forced and they are damped by resistance to the motion exerted by the medium through collision force velocity-dependent, described by the coefficient $\gamma = 1/\tau$. So we can write the general forces balance:

$$F_{perturb} + F_{elastic} + F_{damp} = m\ddot{x}$$

substituting values of each term in the last expression, we obtain the new motion equation for the electron:

$$qE_0 \cos(-\omega t) - Cx - \gamma m \dot{x} = m \ddot{x}$$

By dividing by m and rearranging:

$$\ddot{x} + \gamma \dot{x} + \frac{C}{m} x = \frac{qE_0}{m} \cos(-\omega t)$$

and defining:

$$\omega_0 = \sqrt{\frac{C}{m}}$$

we obtain the equation to solve to describe electrons behavior:

$$\ddot{x} + \gamma \dot{x} + \omega_0^2 x = \frac{qE_0}{m} \cos(-\omega t).$$

It can be shown that the solution is in the form:

$$x = x_0 \cos(-\omega t + \phi)$$

It can be written also as follows:

$$\tilde{x} = \tilde{x}_0 e^{i\phi} e^{-i\omega t}$$

The fact that it is complex means there is a phase shift between the external electric field and the electron response. Incorporating the phase ϕ into \tilde{x}_0 we find:

$$\tilde{x} = \tilde{x}_0 e^{-i\omega t}$$

By substituting the solution in the Eq. 2.1:

$$(-i\omega)^2 \tilde{x}_0 e^{-i\omega t} + \gamma(-i\omega) \tilde{x}_0 e^{-i\omega t} + \omega_0^2 \tilde{x}_0 e^{-i\omega t} = \frac{qE_0}{m} e^{-i\omega t}$$

Simplify the factors $e^{-i\omega t}$ and put in common factor:

$$\tilde{x}_0 (-\omega^2 - i\gamma\omega + \omega_0^2) = \frac{qE_0}{m}$$

Thus, the complex amplitude of electron motion is:

$$\tilde{x}_0 = \frac{qE_0}{m} \frac{l}{\omega_0^2 - \omega^2 - i\omega\gamma} \quad *$$

Now we get the real and imaginary part:

$$\frac{l}{\omega_0^2 - \omega^2 - i\omega\gamma} \times \frac{\omega_0^2 - \omega^2 + i\omega\gamma}{\omega_0^2 - \omega^2 + i\omega\gamma} = \frac{Nq^2}{m\epsilon_0} \frac{\omega_0^2 - \omega^2 + i\omega\gamma}{(\omega_0^2 - \omega^2)^2 + (\omega\gamma)^2} =$$

$$\tilde{x}_0 = \frac{\omega_0^2 - \omega^2}{(\omega_0^2 - \omega^2)^2 + (\omega\gamma)^2} + i \frac{\omega\gamma}{(\omega_0^2 - \omega^2)^2 + (\omega\gamma)^2}$$

The real part of \tilde{x}_0 is:

$$\tilde{x}_{0r} = \frac{qE_0}{m} \frac{\omega_0^2 - \omega^2}{(\omega_0^2 - \omega^2)^2 + (\omega\gamma)^2}$$

and its imaginary part:

$$\tilde{x}_{0i} = \frac{qE_0}{m} \frac{\omega\gamma}{(\omega_0^2 - \omega^2)^2 + (\omega\gamma)^2}$$

The perturbation due to an oscillating electric field will modify the shape of the charge distribution and the two mass centers will move apart, inducing an instantaneous dipole:

$$\mathbf{p} = q \mathbf{r}$$

where q is the electron charge, and r is the distance; in this case r is the actual oscillation (real part of \tilde{x}_0).

By adding the time dependence in the complex amplitude (Eq *):

$$\tilde{x}_0 = \frac{qE_0}{m} \frac{l}{\omega_0^2 - \omega^2 - i\omega\gamma} e^{-i\omega t}$$

replacing the last expression in the previous one:

$$\tilde{p} = (q) \left(\frac{qE_0}{m} \frac{l}{\omega_0^2 - \omega^2 - i\omega\gamma} e^{-i\omega t} \right) \hat{x}$$

we obtain the complex dipole moment:

$$\tilde{p} = \frac{q^2 E_0}{m} \frac{l}{\omega_0^2 - \omega^2 - i\omega\gamma} e^{-i\omega t}$$

By considering the whole material, the complex polarization (\tilde{P} , vector) is the dipole moment per volume. If we assume that there are N electrons per volume, each acting with the same dipole moment, the complex polarization is given by multiplying the last equation by N :

$$\tilde{P} = \frac{Nq^2}{m} \frac{l}{\omega_0^2 - \omega^2 - i\omega\gamma} (E_0 e^{-i\omega t})$$

$$\tilde{P} = \frac{Nq^2}{m} \frac{l}{\omega_0^2 - \omega^2 - i\omega\gamma} \tilde{E}$$

Since the susceptibility (χ), vector that measures how much a material polarizes in response to an electric field, is related to the polarization (P):

$$P = \varepsilon_0 \chi E$$

Then:

$$\tilde{\chi} = \frac{Nq^2}{m\varepsilon_0} \frac{l}{\omega_0^2 - \omega^2 - i\omega\gamma}$$

The factor $\frac{Nq^2}{m\epsilon_0}$ has units of squared frequency and the square root is the plasmon resonance:

$$\omega_p = \sqrt{\frac{Nq^2}{m\epsilon_0}}$$

where ϵ_0 is the free space permittivity. ω_p play a key role in designing plasmonic-based devices. It is associated with the plasmon and describes a traveling wave with a well-defined wave vector and has the oscillation in the direction of the electric field and hence it is a longitudinal mode.

Because q and m are constants the only parameter that influences the plasma frequency is the electron density n , which varies by changing the material.

The susceptibility (and also the electrical polarization) is related to the electrical permittivity (or dielectric function) ϵ_r :

$$\epsilon_r = I + \chi$$

$$\tilde{\chi} = \frac{\omega_p^2}{\omega_0^2 - \omega^2 - i\omega\gamma}$$

so:

$$\tilde{\epsilon}_r = I + \frac{\omega_p^2}{\omega_0^2 - \omega^2 - i\omega\gamma}$$

This quantity describes the behavior of a material in the presence of an electric field; it quantifies the tendency of the material to contrast the electric field intensity within it.

We see that the permittivity is a complex quantity (and thus the refractive index is complex too): its real part describes the strength of the polarization induced by the external electric field, while the imaginary part describes the losses encountered in polarizing the material:

$$Re[\tilde{\epsilon}_r] = I + Re[\tilde{\chi}] (\equiv \epsilon_1) \text{ and } Im[\tilde{\epsilon}_r] = Im[\tilde{\chi}] (\equiv \epsilon_2)$$

Thus, a low loss material is associated with small values of ϵ_2 [19].

The permittivity has frequency dependence and the curve representing it is called *dispersion*.

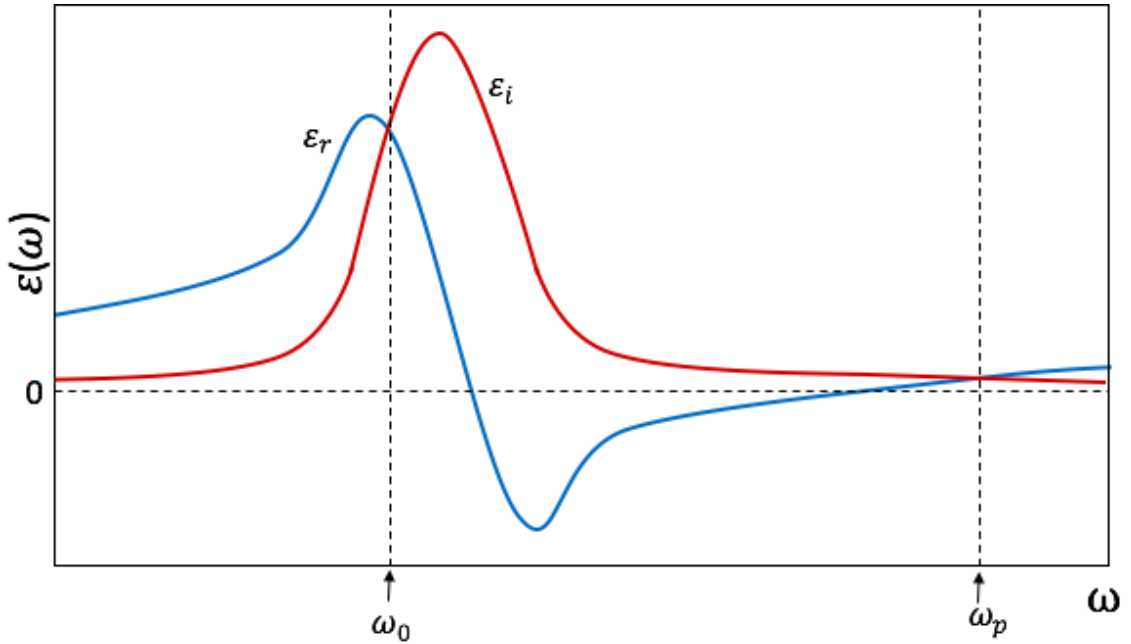


Figure 2: The real (ϵ_r) and imaginary (ϵ_i) parts of the dielectric function [20].

To generalize the findings to a whole material we consider a system with many electrons by introducing a summation:

$$\tilde{\epsilon}_r = 1 + \sum \frac{\omega_{p,i}^2}{\omega_{0,i}^2 - \omega^2 - i\omega\gamma}$$

Here $\omega_{p,i}$, $\omega_{0,i}$ and γ are respectively the plasma frequency, the resonant frequency, and the damping coefficient, respectively, for the i^{th} electron.

By introducing the *oscillator strength* (f_i) which describes the fraction of electrons with the same oscillation frequency:

$$f_i = \frac{N_i}{N_{tot}}$$

the expression can be written in the form:

$$\tilde{\epsilon}_r = 1 + \omega_p^2 \sum \frac{f_i}{\omega_{0,i}^2 - \omega^2 - i\omega\gamma}$$

The plasma bulk frequency ω_p here is defined by the total number of oscillating electrons per volume.

2.2 Plasmon resonance in metals

The valence electrons in metals are not bound to the nuclei but they still respond to the electric field and experience damping in the same way as the electrons in insulators (Lorentz model above). To describe the metals, it is possible to modify the model by simply set $\omega_0 = 0$ to account for no restoring forces. Setting 0 in the Lorentz oscillator model (commonly called Drude model) results in:

$$\tilde{\epsilon}_r = 1 - \frac{\omega_p^2}{\omega^2 + i\omega\gamma}$$

In some metals the high frequency dielectric constant does not go to 1. To account for ϵ_r not going to one, it is use to change the 1 to a different constant called ϵ_∞ , such that

$$\tilde{\epsilon}_r = \epsilon_\infty - \frac{\omega_p^2}{\omega^2 + i\omega\gamma}.$$

2.3 Surface plasmon resonance (SPR)

It has been anticipated that plasmons can be confined in 2D and in particular at the interface between a conductive material and a dielectric. In this case we speak of surface plasmon resonance.

It is not uncommon to find in the literature that surface plasmons and surface plasmon polaritons are interchangeably talked about and this can lead to lack of clarity. They differ formally and it may be appropriate to speak briefly about the differences.

Polaritons are quasiparticles associated to the coupled dipole-electromagnetic propagating wave that exists when an EM mode is strongly coupled to some other type

of mode. When light is strongly coupled to a physical excitation, whatever it is, then the particle picture is inaccurate by treating the two degrees of freedom separately. So instead of representing the excitation by describing photons and other particles separately, it is preferred associating to the excitation a single hybrid particle simply called 'polariton'. Because there are lots of types of excitations, there are lots of types of polaritons too (phonon-polariton, plasmon polariton, ...).

Surface plasmon polaritons (SPPs) are the quasiparticles of the coupled modes of an EM field and a surface plasma oscillation. It is the fundamental optical excitation that is confined to a conductive/dielectric interface [21].

Surface plasmons (SPs) are quasiparticles associated to electromagnetic excitations of a plasma that propagate along the interface between a conductive and a dielectric medium. They are surface waves that have been trapped at the interface and the electric field associated with them decays exponentially with distance from the interface with different rates, in both directions [22]. Although surface plasmons are not the same as surface plasmon polaritons, from the context the two are rarely confused. In addition, the charge oscillations will create an EM field, and so you can't create a SP without it automatically being part of an SPP. For this reason, often the term SP is used even when it is referring to the entire excitation itself and therefore, they technically mean SPP.

Plasma oscillations are in general longitudinal waves, i.e. the displacement of the electrons (relative to a uniform positive background formed by positive ions) are parallel to the direction of propagation of the waves.

Since plasmons will only couple to photons when both their wave vectors and frequencies are the same, thus normally they cannot be excited by a transverse wave like electromagnetic radiation. The wavevector of SPP is larger than that of the light at the same energy. This momentum mismatch means that SPP cannot be triggered directly by light. In order to excite SPPs, an extra momentum has to be added to the photons. Therefore, a variety of strategies were developed to launch SPPs with different coupling efficiencies.

A classical method used to trigger a surface plasmon wave in macroscopic systems is the Kretschmann configuration, the first setups with which SPPs were observed. [23].

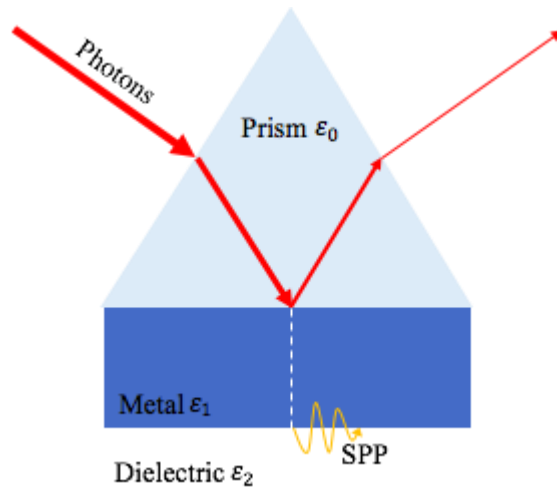


Figure 3: Kretschmann setup used to excite surface plasmons [24].

In the Kretschmann configuration (Figure 3), a thin metal film is deposited on the base of a dielectric prism. A p-polarized light beam is transmitted through it. Since the prism dielectric permittivity (ϵ_0) is greater than that of the dielectric (ϵ_2), a critical angle exists at which total internal reflection occurs. At slightly larger angles, a sharp minimum is observed in the reflection coefficient (Figure 4).

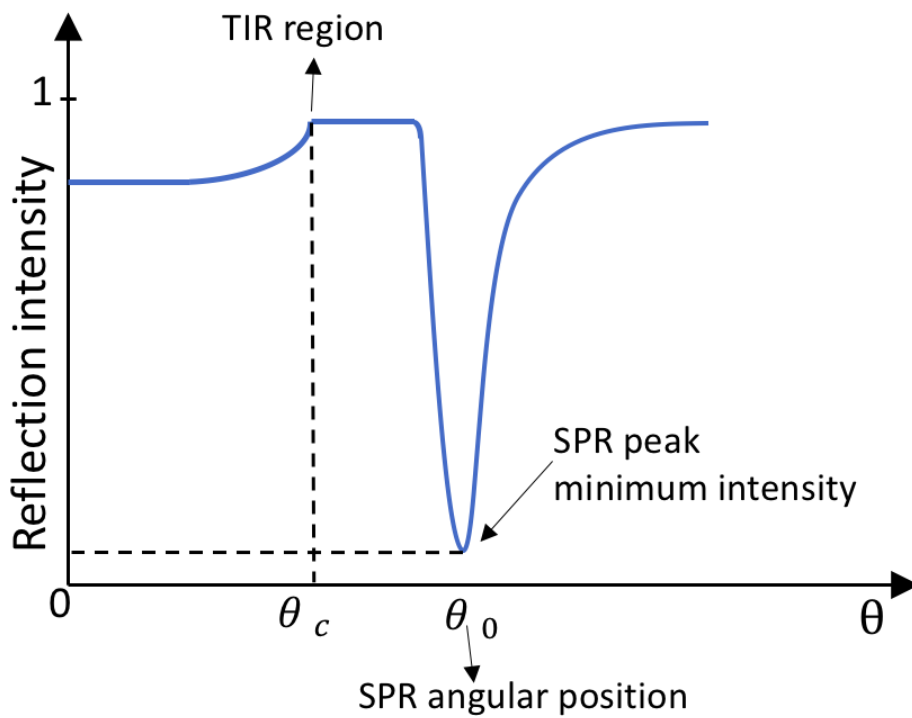


Figure 4: The intensity of the reflected light plot from a monochromatic light source is measured as a function of incident light angle (θ) in Kretschmann configuration [24].

This phenomenon is referred to as attenuated total reflection (ATR) and excitation of the SPP is assumed to be the cause of this loss in the metal [24]. The physical reason that allows the photon to trigger an SPP anyway is the fact that the wave vector of the incident light beam (or electric field) can be decomposed into two components, one perpendicular (k_z) to the metal / dielectric interface and the other parallel (k_x) to the latter, as shown in Figure5.

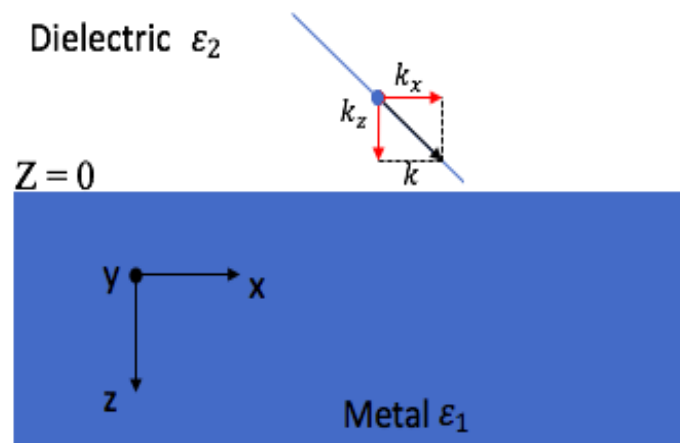


Figure 5: interface along the plane between a dielectric (top), and a conductive (bottom) media. The wave vector components of the incident electric field are shown [25].

The parallel component is a longitudinal wave and if k_x matches the wave vector of the surface plasmon wave (k_{sp}) traveling along the interface, a SPP is excited [25]. In this way one obtains a system composed by a wave in the dielectric medium and an oscillating electron plasma in the metal (Figure 6a). Both modes have an exponentially decay into the respective half spaces (see Figure 6b), i.e. they are evanescent waves.

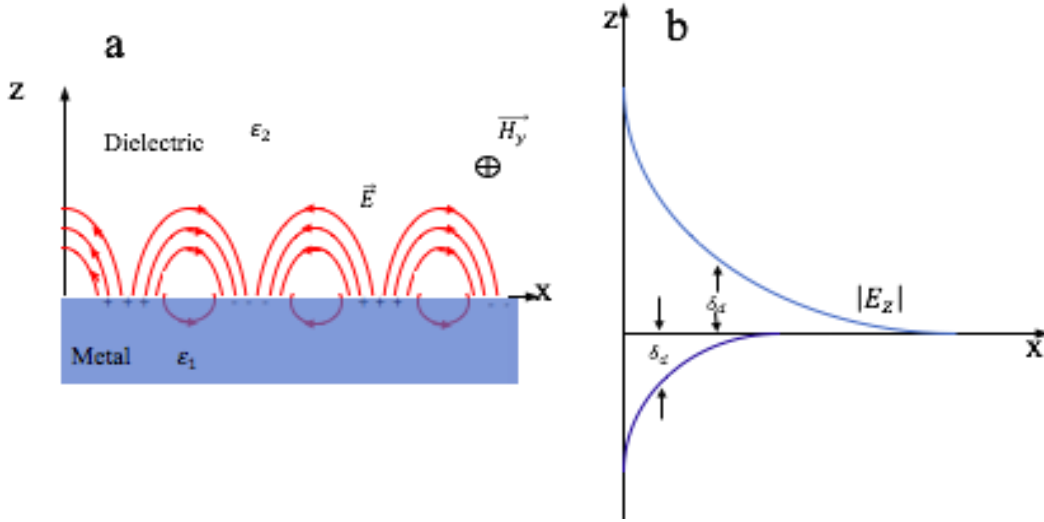


Figure 6: (a) Schematic representation of the electromagnetic field associated with a surface-plasmon polariton propagating along a metal–dielectric interface. + and – represent the regions with lower and higher electron density, respectively. (b) The field strength E_z decreases exponentially with the distance from the surface [25].

The wave vectors of the incident light and the SPP in the metallic films are [26]

$$K_x = \frac{2\pi}{\lambda} \eta p \text{sen}(\theta)$$

$$K_{sp} = \frac{2\pi}{\lambda} \sqrt{\frac{\varepsilon_1 \varepsilon_2}{\varepsilon_1 + \varepsilon_2}}$$

Where ε_1 , ε_2 and ηp represent the complex dielectric function of dielectrics, of the metal and the refractive index of the prism, and λ the wavelength of incident light respectively. The matching relationship, can be expressed as follows:

$$K_{sp} = K_{sp} ; \theta_{sp} = \frac{2\pi}{\lambda} \sqrt{\frac{\varepsilon_1 \varepsilon_2}{\varepsilon_1 + \varepsilon_2}}$$

where θ_{sp} is the resonant angle.

Thus, to observe a SPP we can monitor absorption of an incident EM wave of constant frequency as a function of the angle of incidence on the interface (see Figure 4). For nanosystems this setup is not usable, so for them an effective and convenient way to

excite a plasmon is to use an electrons beam. Electrons penetrating a material can transfer momentum and energy to the material [27]. This momentum can compensate for the momentum difference and excite PR. The loss in energy of the electron primary beam is exhibited by a peak in the electron energy loss spectrum (commonly known as EELS).

The derivation of the physical quantities involved in SPPs begins with Maxwell's equations, which have to be separately solved for the conductive and dielectric parts. It can be demonstrated, by considering the conditions for the continuity of the normal and transverse field components on the interface [28], that SPs only exist if the solutions satisfy the following condition $\epsilon_1 + \epsilon_2 = 0$. It follows that the interface must consist of materials with opposite signed permittivities i.e. $\epsilon_1 = -\epsilon_2$. Surface plasmons can thus only exist at the interface between a material having $\epsilon < 0$ and a material with $\epsilon > 0$. The positive-permittivity material is the dielectric material. The negative-permittivity material, often called the plasmonic material, may be a metal or other material like semiconductors.

The dispersion relation for the SPP is:

$$k_x = \frac{\omega}{c} \sqrt{\frac{\epsilon_1 \epsilon_2}{\epsilon_1 + \epsilon_2}}$$

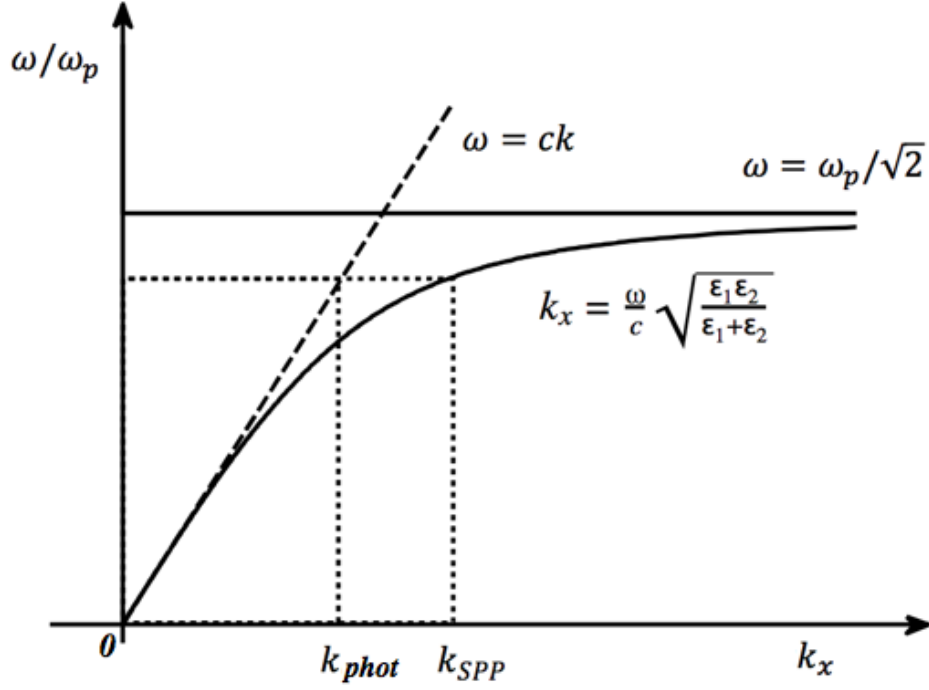


Figure 7: SPP dispersion curve in a metal / air interface. The figure points out the problem of the mismatch between the moments, which must be overcome to allow the coupling of the light with the excited plasmon. Plasmon resonance always lies beyond the line of light [29].

Figure 7 shows the SPP dispersion curve in a metal / air interface. We see that at low k , the SPP behaves like photons, but by increasing k , the curve bends over and asymptotically tends the limit called the "surface plasma frequency" [29]. Notice that the SPP dispersion curve is on the right side with respect to that of the photons, $\omega = k \cdot c$, it means the SPP has a shorter wavelength than free-space radiation. The surface plasma frequency is the asymptote of this curve, and is given by:

$$\omega_{sp} = \sqrt{\frac{\omega_p^2}{1+\epsilon_d} - \gamma^2} \approx \frac{\omega_p}{\sqrt{1+\epsilon_d}}$$

indicating that SPPs always occur at frequencies smaller than bulk plasmons and when the dielectric medium is air, $\epsilon_d \approx 1$ and the relation becomes simply:

$$\omega_{sp} = \frac{\omega_p}{\sqrt{2}}.$$

2.4 Localized surface plasmon resonances

The localized surface plasmon resonance (LSPR) is the result of the confinement of a surface plasmon in a nanoparticle of size comparable to the wavelength of the beam used to excite it. They are non-propagating stationary waves which therefore cannot be described through a wave vector and light can trigger it directly without the need of special configurations.

To predict the LSPR frequency, we have to calculate the nanoparticle polarizability α :

$$\alpha = 4\pi\epsilon_2 R^3 \frac{\epsilon_2 - \epsilon_1}{\epsilon_2 + \epsilon_1}$$

where ϵ_1 and ϵ_2 are the dielectric function of the particle and the medium in which the particle is embedded, respectively.

That is, it is still necessary to know the involved dielectric functions. For "common" plasmonic materials such as metals, using the bulk permittivity works quite well to get the LSPR frequency, except for very small nanoparticles. For "unconventional" plasmonic materials such as semiconductors or p-block elements the situation is less clear as there are not so many studies till now on the topic. However, starting with the bulk dielectric function is always a wise choice.

The resonance condition occurs when the polarizability assumes its maximum value. For a spherical nanoparticle this condition is true when the denominator of the previous relation is zero, that is:

$$\epsilon_1 = -2\epsilon_2$$

and the plasma frequency, for the system in vacuum (ϵ_2), has the following expression:

$$\omega_{lsp} = \frac{\omega_p}{\sqrt{3}}.$$

As we can see, also the LSPR of nanoparticles does not peak at the bulk plasma frequency.

Effect of the dimension

The surface plasmon resonance frequency of a nanoparticle depends on the size and in general shifts towards lower wavelengths (or higher energies, commonly called blue shift) as the size decreases and vice versa when the size increases (Figure 8).

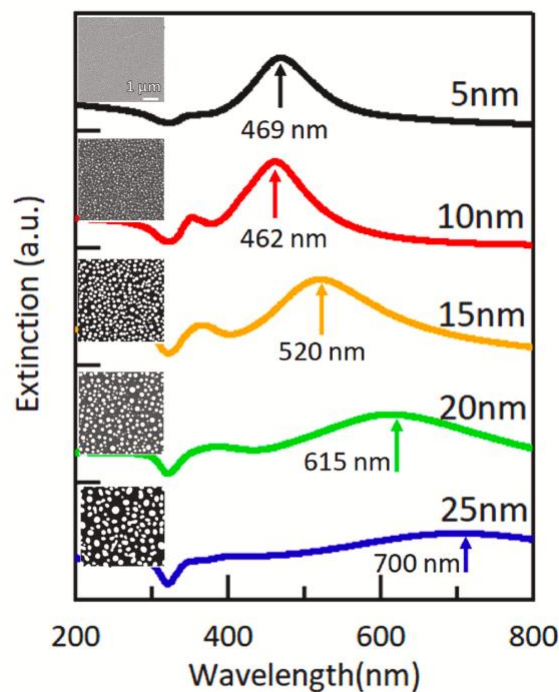


Figure 8: Extinction spectra of the Ag NPs with different average diameter. The main peak position of the extinction was indicated by the arrow and it shifts toward red as the diameter increases [30].

Effect of the external environment

The frequency nanoparticle's surface plasmon resonance also depends on the surrounding environment through the dielectric constant ϵ_2 . As the surrounding dielectric constant ϵ_2 increases, the SPR peaks shift to longer wavelengths (called red shift).

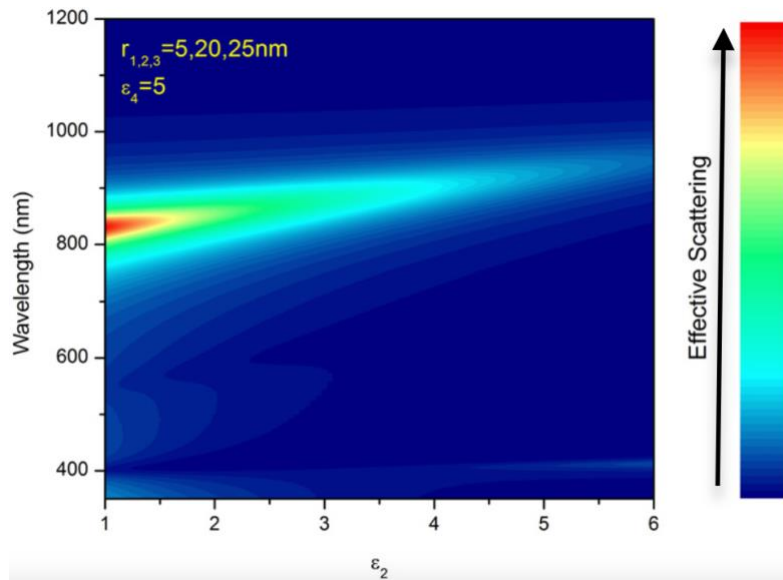


Figure 9: The effect of ϵ_2 on the effective scattering spectra of Au-Di-Ag nanoshells [31].

Effect of geometry

Frequency, intensity, width to half height and peak shape of LSPR also depend on particle geometry. As we can see in Figure 10. The spectral look considerably varies by changing the particle shape.

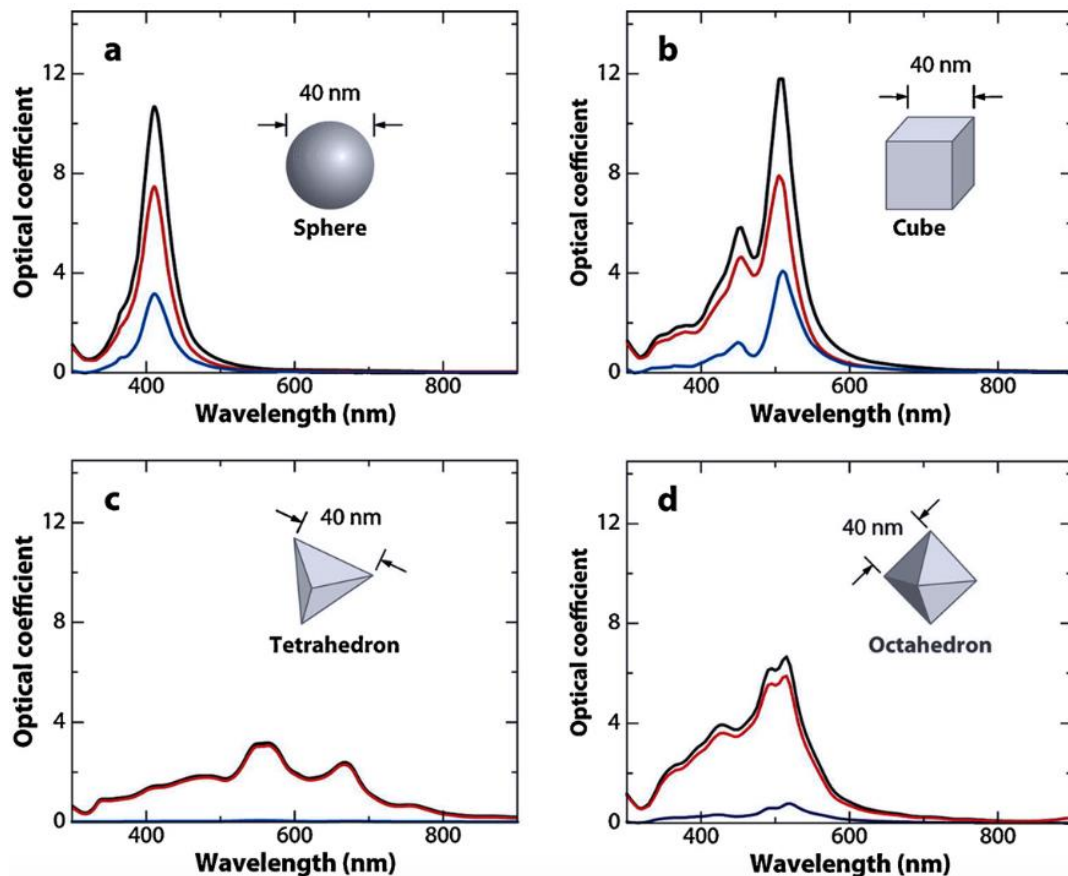


Figure 10: Extinction (black), absorption (red), and scattering (blue) spectra calculated for Ag nanoparticles of different shapes: (a) a sphere displaying a single dipole resonance peak and (b) a cube, (c) a tetrahedron, (d) an octahedron [32].

2.5 PR in cylindrical system

Plasmonics in particles with anisotropic geometries typically exhibit complex spectra with multiple peaks (Figure 11).

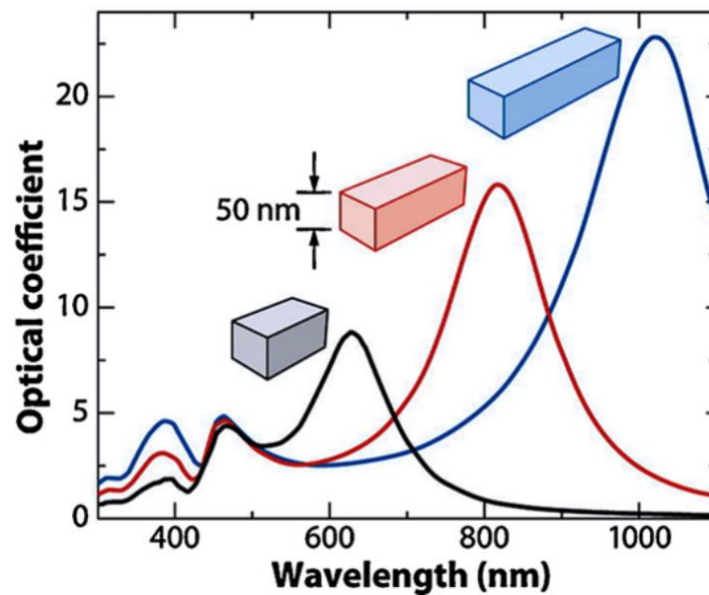


Figure 11: Extinction spectra of rectangular Ag bars with aspect ratios of 2 (black), 3 (red), and 4 (blue). Note that the nonspherical particles typically exhibit multiple, red-shifted resonance peaks [32].

As a consequence, the analytical description of the spectra becomes more difficult than in the case of spherical particles.

To obtain the resonance frequency value for elongated nanosystems like that wireshaped, the length- to-diameter ratio $R = d/(2r)$ must be considered, that's it the *aspect ratio* of the particle. It can be demonstrated that the plasmon resonance can be approximated by the expression:

$$\omega_{lres} = \frac{\omega_p}{2\sqrt{2}} \frac{1}{R}.$$

Again, we see that the surface resonance occurs at lower energy than the bulk one. It must be said that this is a very simple model so we cannot expect the result to quantitatively reproduce the exact resonance frequencies for any wire thickness. Moreover, it does not explain the additional resonances that are observed in the extinction spectra for elongated geometries in Figure 11. However, it qualitatively reproduces the experimental trend observed, i.e. that the resonance frequency is inversely proportional to the system aspect ratio R [33].

To obtain a more accurate model than the previous one for elongated nanostructures, they are geometrically assimilated to prolate spheroids, although nanowires are quasi-cylindrical structures [34, 35].

For this shape the dipole mode splits into two distinct surface dipolar modes, as it happens for cylindrical geometry (Figure 12), with respect to that of a sphere of equivalent size.

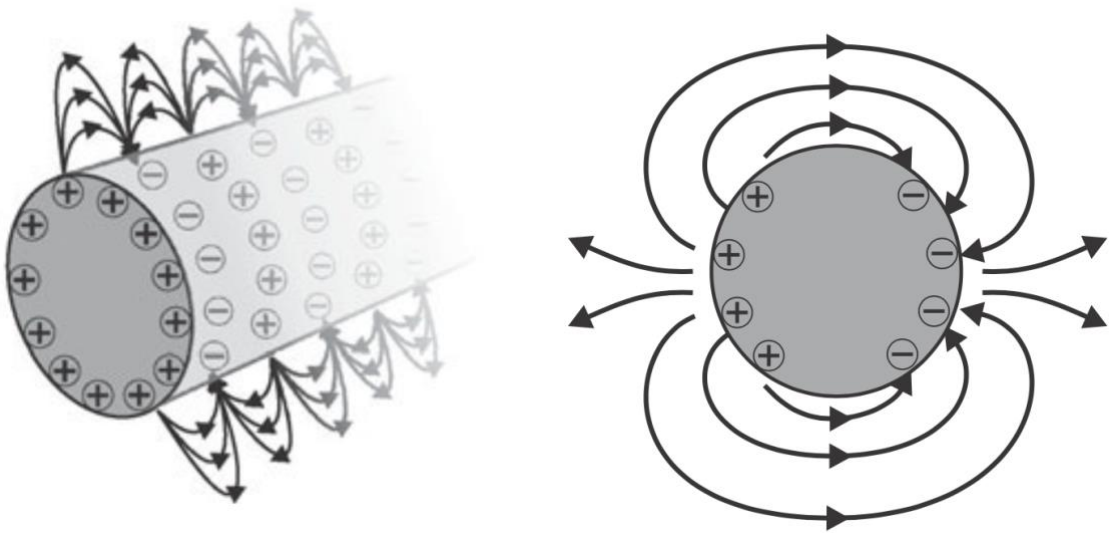


Figure 12: Charge distribution and field lines for SPP modes (a) A propagating wire plasmon (TM₀ mode). (b) A transverse wire plasmon with a dipolar field pattern [36].

The two eigen directions are the axial (major a axis) direction and the transversal-radial (minor b, c axes) direction on which electron oscillations lie along i.e. exist two plasmon resonance frequencies ω_{sp1} and ω_{sp2} . [37] This means that the response

depends on the incident electric field polarization direction and this fact potentially allows adaptable frequency modulation with respect to the specific application.

Moreover, if its major axis is greater than the wavelength of the SPR, SPP can propagate along the major wire axis and the longitudinal modes become multipolar Fabry–Perot (FP) type resonances. The transverse one instead remains a quasistatic LSPR.

A FP-type resonance is triggered on a nanowire, when two counter-propagating short-range SPP waves meet and set up an interference pattern. Since these modes can be effectively excited via electron-SPP inelastic scattering [38], they appear in EELS as multiple antinodes [39-40]. The wavelength of the m^{th} mode is

$$\lambda_{\text{sp}} = 2L/n$$

Where L is the length of the nanowire and n is the mode number.

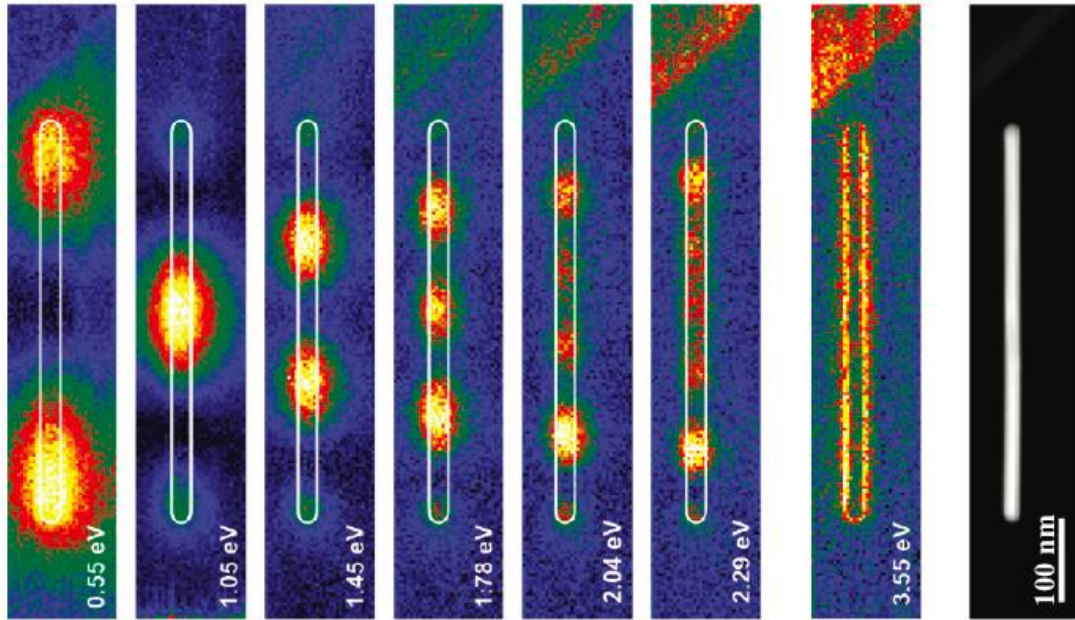


Figure 13: Energy-filtered plasmon maps of Ag NW extracted at resonance energies extracted at local energy loss maxima resolve Fabry Perot type resonant modes from $m = 1$ to 6 showing nodes and antinodes. Confined surface plasmon mode at 3.55 eV [40].

To obtain the FP plasma frequencies, one must start from the expression of polarizability. For a prolate spheroid in the quasi-static limit ($\lambda \gg \text{dNW}$) it is [41; 42]:

$$\alpha_j = 4\pi abc \frac{\varepsilon_l - \varepsilon_2}{3\varepsilon_2 + 3L_j(\varepsilon_l - \varepsilon_2)}$$

where $j = a, b$ or c are the semiaxes of the ellipsoid ($a > b = c$), ε_l is the permittivity of the material, ε_2 is the permittivity of the surrounding medium, and V is the particle volume. L_j are the depolarization factors, given by [43]:

$$L_a = \frac{1 - e^2}{e^2} \left(-1 + \frac{1}{2e} \ln \frac{1 + e}{1 - e} \right)$$

$$L_{b,c} = \frac{1 - L_a}{2}$$

$$e = \sqrt{1 - \left(\frac{1}{R}\right)^2}$$

Where e is the object ellipticity and R is the aspect ratio, defined as the ratio of the long-axis (a) to the short-axes (b and c) length. The plasmon resonance condition ($\rightarrow \infty$) occurs when the denominator in Equation 1 is equal to zero:

$$\varepsilon_2 + L_j(\varepsilon_l - \varepsilon_2) = 0$$

ε_{lr} denotes the real part of ε_l . Rearranging equation the last equation gives:

$$\varepsilon_{lr} = \left(\frac{-1}{L_j} + 1 \right) \varepsilon_2$$

The real part of the permittivity is approximated as a function of the incident light frequency, ω , via the Drude model:

$$\varepsilon_r = 1 - \frac{\omega_p^2}{\omega^2 + \gamma^2}$$

Combining the last two equation yields:

$$\omega_{sp} = \sqrt{\omega_p^2 \cdot L_j - \gamma^2}$$

with $\omega = \omega_{sp}$ is the LSPR frequency that is a function of ω_p , L_j and γ [42].

If $L_j = L_a$ and $L_j = L_{b,c}$ we get two families of LSPRs frequencies depending on the permittivity.

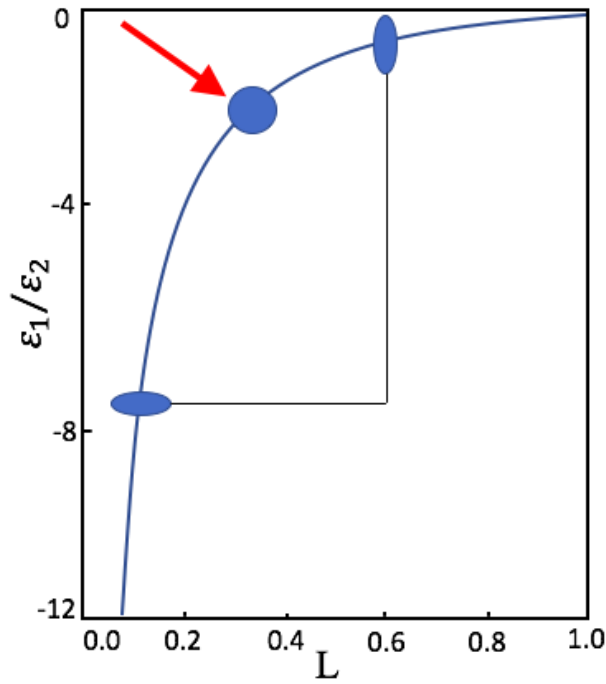


Figure 14: Two modes split out from the spherical point when the degeneracy between collective electron oscillations along different directions is lifted due to the elongated geometry [42].

For a sphere, the single plasmon mode occurs corresponding to $L=1/3$. When the degeneracy between collective electron oscillations along different directions is lifted, the two modes split out from the point indicated by the red arrow in Figure 14. The transverse mode asymptote towards $L=1$, giving a peak at the wavelength where $\epsilon_1=0$ and the transverse band blue shifts slightly as the rod grows. Conversely the longitudinal mode continues to slide to more negative values of ϵ_1/ϵ_2 corresponding

to longer wavelengths. Notice that small changes in aspect ratio leads to drastic changes in spectral behavior.

2.6 Surface plasmon resonance in SiNWs

Since plasmon resonance is a collective phenomenon involving the free electric charges present in a conductive material, therefore to observe plasmons it needs that the system have unbound charge carriers, i.e. have electrons in the conduction band and / or holes in the valence band. SiNWs produced in this work were not doped in the growth phase, therefore it could be expected that they do not support plasmonic phenomena as opposed to what happens instead. The reason is mostly due to the fact that the nanowires intrinsically possess structural defects that act as dopants. Moreover, we must consider that such thin wires, with a diameter of the order of 10 nanometers, have a high surface to volume ratio. By now we know that the surface of a material is a region that differs considerably from the bulk due to the very high defects that are concentrated in it, even more so in cylindrical nanostructures such as nanowires due to the high curvature radius that stresses the chemical bonds.

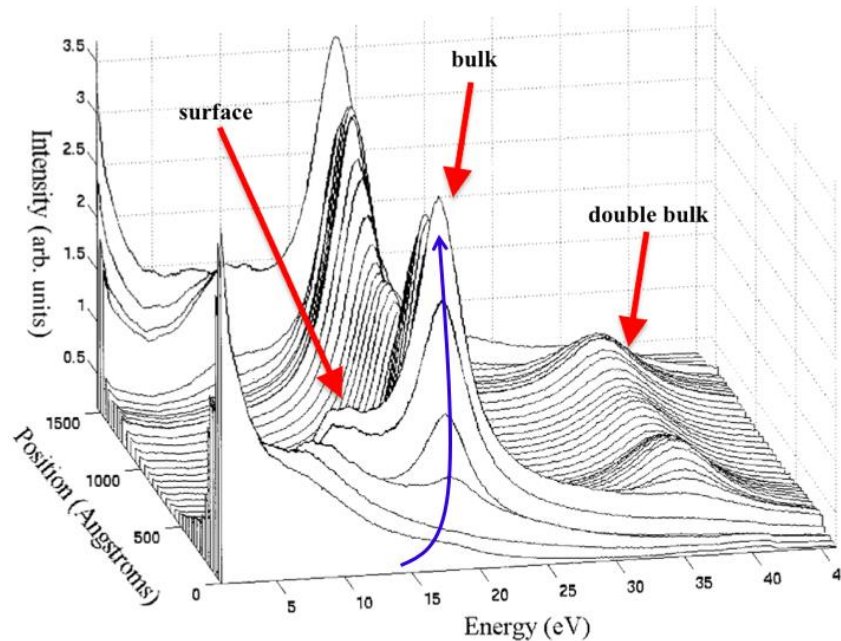


Figure 15: Energy loss spectra scan across 130 nm diameter Si cylinder. with a diameter of roughly 130 nm starting from the outside inwards (see the black arrow). Surface, bulk, and double bulk plasmon losses are clearly visible [4].

However, from literature it is known that SiNWs show the bulk plasmon resonance at 17 eV. We also see a surface plasmon at 11 eV. Eventually, the double bulk plasmon loss at 33 eV is found. A narrow peak at 5 eV and, sometimes, another at about 8 eV are detected. These peaks are described in works [4, 45, 46, 47]. These are the only significant low-energy peaks the authors encountered and of some the origin is not unambiguously explained. In our work we will demonstrate that the SiNWs actually show other peaks, as anticipated in the previous paragraph, and we will also re-discuss the low energy peak (5 eV) attribution made so far. Furthermore, as the Figure 15 suggests, there is a spatial dependence of the spectrum: the curve varies its characteristics if acquired outside the wire, in the edge or in its center (see the blue arrow). This dependence will be addressed in detail.

2.7 Conclusions

In this chapter has been introduced that branch of physics of matter commonly known as plasmonics. The most relevant aspects have been discussed in a simplified way, starting from the simplest and most ancient model commonly used: the Drude-Lorentz model, distinguishing between bulk, surface and localized resonances. We have seen how the plasmonic characteristics depend on the material, the environment in which it is embedded, the size and shape of the nanosystem. In particular, we focused more on the spheroid shape as this well describes the SiNWs. Finally, the main results of the few experimental works available on the plasmonic behavior of SiNWs were discussed.

Bibliography

- [1] Eldlio, Mohamed, Franklin Che, and Michael Cada. "Drude-Lorentz model of semiconductor optical plasmons." *IAENG Transactions on Engineering Technologies*. Springer, Dordrecht, 2014. 41-49
- [2] Yao B, Fang ZB, Zhu YY, Ji T, He G (2012) A model for the frequency dispersion of the high-k metal-oxide semiconductor capacitance in accumulation. *Appl Phys Lett* 100: 222903/ 1–3
- [3] Cada M, Pištora J (2011) Optical plasmons in semiconductors. In: ISMOT conference, June 20–23
- [4] Reed, B. W., et al. "Fabrication and STEM/EELS measurements of nanometer-scale silicon tips and filaments." *Physical Review B* 60.8 (1999): 5641
- [5] A. Otto, "Excitation of nonradiative surface plasma waves in silver by the method of frustrated total reflection," *Z. Phys.* **216**, 398–410 (1968)
- [6] Maier S (2007) *Plasmonics fundamentals and applications*, 1st edn. Springer Science and Business Media LLC, Berlin, pp 21–39
- [7] Novotny L, Hecht B (2008) *Principles of nano-optics*, 2nd edn. Cambridge University Press, Cambridge, MA, pp 378–414
- [8] J. B. Pendry, *Phys. Rev. Lett.* 85, 3966 (2000), P. Anger, P. Bharadwaj, and L. Novotny, *Phys. Rev. Lett.* 96, 113002 (2006).
- [9] P. Muhlschlegel et al., *Science* 308, 1607 (2005), E. J. Sanchez, L. Novotny, and X. S. Xie, *Phys. Rev. Lett.* 82, 4014 (1999)
- [10] Mohamed, Mona B., et al. "The lightning'gold nanorods: fluorescence enhancement of over a million compared to the gold metal." *Chemical Physics Letters* 317.6 (2000): 517-523
- [11] Islam, Md Saiful, et al. "Localized surface plasmon resonance biosensor: an improved technique for SERS response intensification." *Optics letters* 44.5 (2019): 1134-1137
- [12] Lieberman, Itai, et al. "Plasmon-resonance-enhanced absorption and circular dichroism." *Angewandte Chemie* 120.26 (2008): 4933-4935
- [13] Santangelo, Saveria, et al. "On the plasmon-assisted detection of a 1585 cm⁻¹ mode in the 532 nm Raman spectra of crystalline α -Fe₂O₃/polycrystalline NiO core/shell nanofibers." *Applied Physics Letters* 118.25 (2021): 251105

- [14] Anderson, Samuel R., et al. "Robust nanostructured silver and copper fabrics with localized surface plasmon resonance property for effective visible light induced reductive catalysis." *Advanced Materials Interfaces* 3.6 (2016): 1500632
- [15] Chaumet, Patrick C., Adel Rahmani, and Manuel Nieto-Vesperinas. "Optical trapping and manipulation of nano-objects with an apertureless probe." *Physical review letters* 88.12 (2002): 123601
- [16] Zheng, Yue Bing, et al. "Molecular plasmonics for biology and nanomedicine." *Nanomedicine* 7.5 (2012): 751-770
- [17] Garnett, Erik C., et al. "Nanowire solar cells." *Annual review of materials research* 41 (2011): 269-295
- [18] A.Sanchez-Gil, Jaime Gomez Rivas (2006), "Thermal switching of the scattering coefficients of terahertz surface plasmon polaritons impinging on a finite array of subwavelength grooves on semiconductor surfaces", *Phys. Rev B* 73,205410
- [19] V. P. Drachev, U. K. Chettiar, A. V. Kildishev, H. K. Yuan, W. Cai, and V. M. Shalaev, *Opt. Exp.* 16, 1186–1195 (2008)
- [20] Kelleners, T. J., et al. "Frequency dependence of the complex permittivity and its impact on dielectric sensor calibration in soils." *Soil Science Society of America Journal* 69.1 (2005): 67-76.
- [21] Ritchie RH (1957) Plasma losses by fast electrons in thin films. *Phys Rev* 106:874
- [22] Wallis and Stegeman, 1986; Fillard, 1996
- [23] E. Kretschmann and H. Raether, *Z. Naturforsch.* 23A, 2135 (1968).
- [24] V. M. Agranovich and D. L. Mills, *Surface Polaritons: Electromagnetic Waves at Surfaces and Interfaces* (North-Holland, Amsterdam, 1982)
- [25] Vinogradov, A. P., et al. "Exciting of surface plasmon polaritons in the Kretschmann configuration"
- [26] J. Homola, S. S. Yee and G. Gauglitz: *Sensor. Actuator. B* 54 (1999) 3–15
- [27] H. Raether. *Surface plasmons*. Springer-Verlag Berlin, 1988
- [28] J.D. Jackson_ *Classical Electrodynamics*
- [29] Maier, Stefan A. (2007). *Plasmonics: Fundamentals and Applications*. New York: Springer Publishing. ISBN 978-0-387-33150-8
- [30] Kiba, Takayuki, et al. "Control of localized surface plasmon resonance of Ag nanoparticles by changing its size and morphology." *Vacuum* 192 (2021): 110432
- [31] Zhu, Jian, and Shu-min Zhao. "Improve The Effective Resonance Light Scattering Of Three-Layered Plasmonic Au@ Dielectric@ Ag Bimetallic Nanoshells." (2021).

- [32] X.M.Lu, M.Rycenga, S.E.Skrabalak, B.Wiley, Y.N.Xia, *Annu.Rev.Phys.Chem.* 60 (2009) 167
- [33] Novotny, Lukas, and Bert Hecht. *Principles of nano-optics*. Cambridge university press, 2012
- [34] Chou, Li-Wei, et al. "Tunable mid-infrared localized surface plasmon resonances in silicon nanowires." *Journal of the American Chemical Society* 134.39 (2012): 16155-16158
- [35] P. B. Johnson and R. W. Christy, "Optical constants of the noble metals," *Phys. Rev. B* 6, 4370–4379 (1972)
- [36] Novotny, Lukas, and Bert Hecht. *Principles of nano-optics*. Cambridge university press, 2012.
- [37] Sambou, A., et al. "Control of the surface plasmon resonance of two configurations of nanoparticles: simple gold nanorod and gold/silica core/shell." *Nanoscience and Nanotechnology Research* 4.1 (2017): 1-6.
- [38] Nicoletti, O.; Wubs, M.; Mortensen, N. A.; Sigle, W.; van Aken, P. A.; Midgley, P. A. Surface Plasmon Modes of a Single Silver Nanorod: An Electron Energy Loss Study. *Opt. Express* 2011, 19, 15371–15379
- [39] Losquin, A.; Kociak, M. Link between Cathodoluminescence and Electron Energy Loss Spectroscopy and the Radiative and Full Electromagnetic Local Density of States. *ACS Photonics* 2015, 2, 1619–1627; *Chem. Rev.* 2018, 118, 2994–3031
- [40] Rossouw, D., et al. "Multipolar plasmonic resonances in silver nanowire antennas imaged with a subnanometer electron probe." *Nano letters* 11.4 (2011): 1499-1504
- [41] Chou, Li-Wei, et al. "Tunable mid-infrared localized surface plasmon resonances in silicon nanowires." *Journal of the American Chemical Society* 134.39 (2012): 16155-16158; R. W. Cohen, G. D. Cody, M. D. Coutts, and B. Abeles, *Phys. Rev. B* 8, 3689 (1973)
- [42] Verma, S.S., Sekhon, J.S. Influence of aspect ratio and surrounding medium on Localized Surface Plasmon Resonance (LSPR) of gold nanorod. *J Opt* 41, 89–93 (2012)
- [43] Jun *et al* 2008 *Chinese Phys. Lett.* 25 4459
- [44] *J. Am. Chem. Soc.* 2012, 134, 39, 16155–16158
- [45] Wang, Juan, et al. "From nanoparticle to nanocable: Impact of size and geometrical constraints on the optical modes of Si/SiO₂ core/shell nanostructures." *Applied Physics Letters* 95.13 (2009): 133102.

[46] Kikkawa, J., et al. "Enhanced direct interband transitions in silicon nanowires studied by electron energy-loss spectroscopy." *Physical Review B* 75.24 (2007): 245317.

[47f] Swain, Bhabani S., Bibhu P. Swain, and Nong M. Hwang. "Investigation of electronic configuration and plasmon loss spectra in Au-catalyzed silicon nanowire networks." *Journal of Applied Physics* 108.7 (2010): 073709.

Chapter 3

Experimental

In this section the experimental procedures implemented to fabricate crystalline SiNWs with controlled characteristics, such as length, thickness and density are discussed. SiNWs have been grown on CZ <100> 13 Ω -cm p-type 6 inches Si wafers. During an IP-CVD/VLS process the Si atoms, after the plasma decomposition, are deposited on the wafer (substrate) where they can interact:

- with the catalyst (eutectic liquid alloy), giving rise to the growth of SiNWs, or
- with the bare Si substrate, where they deposit on it and can diffuse or form a stable two-dimensional (2D) Si layer.

To ensure eutectic formation, the substrate surface has to be clean by impurities or particulates due to volatile hydrocarbons and free of any oxide films like native oxide layer. Thus, a pretreatment procedure upstream of the synthesis is necessary.

3.1 Pretreatment

The pretreatment procedure of each substrate took place entirely in a controlled atmosphere area, in a class 100 clean room, i.e. less than 100 particles larger than 0.5 microns are present for cubic feet of air. Air is recirculated approximately 20-30 times per hour by a constant laminar air flow from ceiling to floor. Air which enters the clean room is continuously filtered to remove dirt and dust particles. The efficiency of the filtering system is automatically monitored to ensure constant performance over time. The clean room is positively pressurized with respect to the adjacent areas, to prevent accidental introduction of contaminants. Air temperature is stable within 1 °C and its relative humidity is maintained at 40 +/- 2% [1].

3.1.1 Sonication

To remove any physisorbed impurities, each substrate has undergone a sonication process in fume hood in 3 different solvents separately and in sequence: acetone, ethyl alcohol and water, for 5 minutes each one. Between one step and the next one the substrates were dried with compressed air. The sequence is established on the basis of

the polarity of the solvents, i.e. from the least polar to the most polar in order to quantitatively remove all the organic pollutants present on the surface.

3.1.2 HF etching

Native oxide is always present on the Si surface, since it forms as soon as wafers are exposed to the atmosphere; thus, once dried, each substrate has undergone a native oxide removal process with hydrofluoric acid (HF). In aqueous solution, the competitive reaction products that can form on the substrate surface are Si-O, Si-F and Si-H bonds. The silicon etching in HF results in a stable surface termination rich in hydrogen dangling bonds [2]. This is due to the fact that the Si-H is a covalent practically unpolarized bond with high degree of chemical stability. In contrast a Si-O bond has 46% ionic character and the Si-F bond has 67% ionic character. The oxygen and fluorine atoms' great electronegativity makes that surface adsorbed ones generate a strong polarization, causing the weakening of the backbonds of the corresponding Si adatom. This makes Si more reactive than it is in the absence of adsorbed electronegative species and more prone to being attacked by a dipolar molecule such as HF. This eventually leads to the formation of the most stable product which is a finished surface H. This is the reason why only a small amount of fluorine is found on HF-etched Si surfaces.

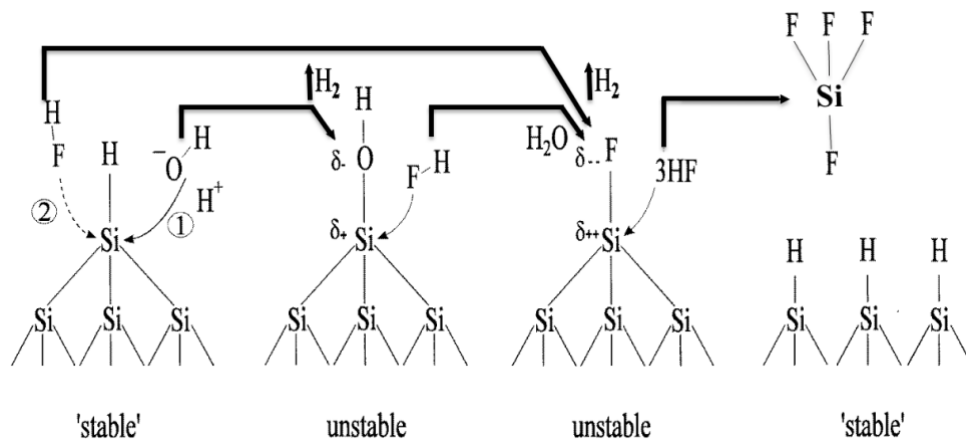
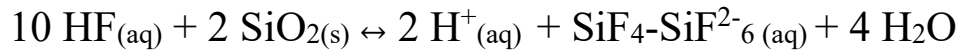


Figure 1. Schematic representation of the likely silicon surface oxidation mechanisms which lead to Si removal and surface hydrogenation. The hydrogenated Si surface may be considered relatively stable against chemical attack. In contrast the strongly polarized Si-O and Si-F bonds are rather unstable. The depicted mechanisms are not

restricted to a monohydride-covered {111} surface adatom but should also apply to other configurations [3].

The global reaction between HF and SiO₂ can be resumed by the following [4]:

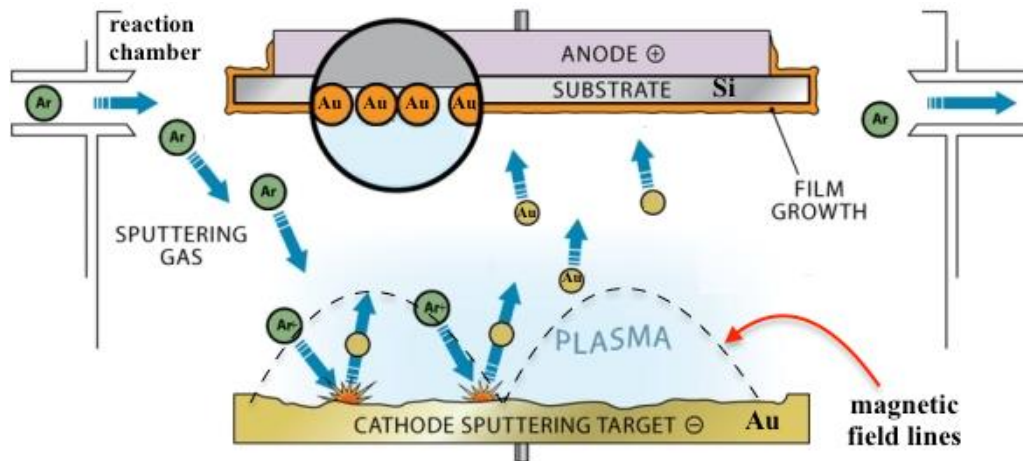


Each wafer treated in this thesis underwent an etching by immersion in a solution of HF concentrated at 16% while stirring for about one minute.

3.2 Catalyst deposition via sputtering

The metal catalyst (Gold) deposition was carried out by sputtering, a widely used technique in industrial processes to obtain high quality thin films at low temperature. Sputtering is also known as cathodic vaporization [5], and consists of a physical vapor deposition (PVD) process whereby particles are emitted from a solid material, called target (a 99.99% pure Au disk in our case), due to the momentum exchange associated with the surface bombardment with energetic ions beam. These particles deposit on the substrate usually located in front of the target inside the reaction chamber, generating the thin films.

Ions are extracted from a cold plasma (0.5-10 keV), triggered by a glow discharge, by applying an electric field between the two electrodes: the target which acts as a cathode and the substrate, placed on the anode. Generally, an inert gas, as argon (Ar), is used for the generation of the ions. The ion's impact leads to the target's atoms vaporization and also causes the emission of secondary electrons from the target surface, which helps to support the plasma. The emitted material is mainly in the form of electrically neutral particles, such as non-ionized atoms, fragments of molecules, radicals and other species which can freely move away from the target. By hitting the substrate surface, particles condense resulting in a thin film.



SEP

Figure 2: Schematic of magnetron sputtering deposition [5].

There are different plasma generation modes, corresponding to three different deposition set ups: Direct Current (DC) sputtering, Radio Frequency (RF) sputtering and Magnetron sputtering.

In our case, magnetron sputtering was used. This tool uses a strong magnetic field parallel to the target surface to capture secondary electrons, keeping them close to the target. One of the advantages of this tool consists of the plasma confinement to an area near the target, so that it cannot cause harm to the thin film being formed on the substrate. A schematic of the deposition system is shown in Figure 2.

In this thesis work the deposition parameters were explored to optimize the morphology of the deposited Au film, that are: chamber pressure (P), process time (t) and current (mA) (related to the potential difference between the electrodes). We found that the best operating conditions to obtain a deposit consisting of an array of nanoparticles with a maximum diameter of a few tens of nanometers are:

- $P = 5 \times 10^{-3}$ mbar
- Current = 10 mA
- time = 80s.

Applying these operating conditions, an array of separate Au nanoparticles is obtained. The equivalent thickness is monitored in situ by a quartz balance coupled to the sputter. The average equivalent film thickness results in around 2-3 nm. The particle size is between 5 and 50 nm with an average size of about ten nm.

The typical system aspect we obtain is shown in Figure 3 which reports a SEM micrograph in planar view.

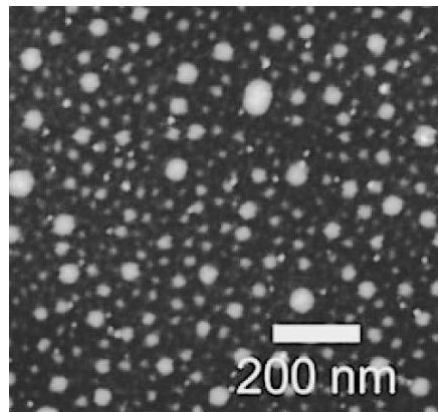


Figure 3: SEM micrograph of Au nanoparticles with diameters of the order of tens of nanometers deposited by sputter on Si wafer.

3.3 Synthesis of SiNWs by CVD via VLS

Once the metal deposition is complete, the process of SiNWs synthesis starts. The samples were transferred into the IP-CVD system, as described in Chapter 1.

Each sample was incubated in a pre-chamber under vacuum for one hour at a temperature $T = 395^{\circ}\text{C}$. This temperature is higher than that of the eutectic Au / Si (363°C) and allows its formation. The temperature ramp was about 1°C per minute starting from about 70°C . After exploring the deposition parameters, the following ones were found as optimal for the SiNWs growth:

- Plasma power = 20 W,
- Pressure = 50 mTorr,
- Precursor flux (SiH_4) = 30 sccm,
- Gas carrier flux (Ar) = 1 sccm,
- Process duration = 1800s.

After the deposition, the samples were cooled with a temperature ramp inverse to the heating one, and finally extracted to be analyzed by some microscopy techniques such as SEM, TEM, STEM. An “as grown” sample is showed in Figure 4.

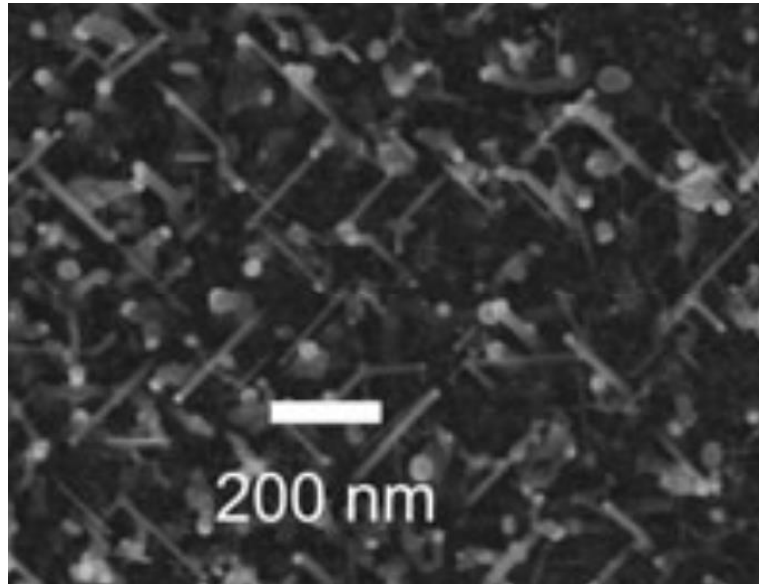


Figure 4: SEM micrograph in planar view; typical aspect of SiNWs array as grown.

3.4 Gold removal

As mentioned, Au is the most commonly used catalyst for SiNWs growth for the several advantages it offers such as low eutectic temperature with silicon (363 °C), fast interdiffusion in silicon and the high solubility allowing the formation of $\text{Au}_{82}\text{Si}_{18}$. However, when VLS/CVD growth ends, Au dots remain linked to the NWs top (see Figure 5). Note that this is a strong proof that the growth occurred through the VLS mechanism. In addition, as mentioned, Au residues are also distributed across the nanowires side walls.

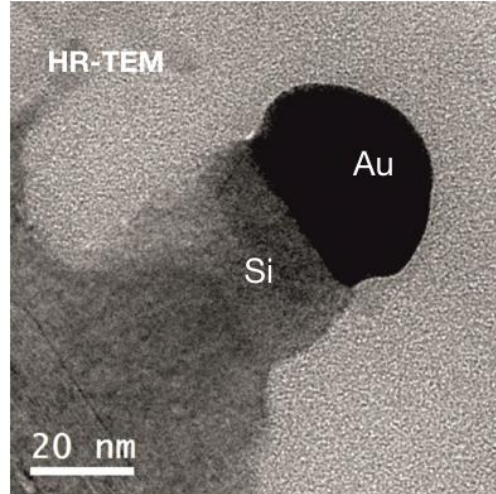


Figure 5: Post growth TEM micrograph acquired in bright field conditions of a single SiNW [6].

Despite these advantages, Au also presents several issues. For instance, Au is detrimental for the minority carriers activity, due to the fact it introduces modifications in the silicon electronic structure. In particular, it generates a deep acceptor state at $E_c - 0.54$ eV in p-type Si and a donor level at $E_v + 0.35$ eV in n-type Si that act as effective charge recombination centers, consequently causing the electronics devices electrical and optical performance degradation. Therefore, it is unavoidable to make a further Au removal step.

However, removing Au by using the classical etching solution, i.e. sodium iodide (NaI) and iodine (I_2), diluted in H_2O (1:10), proved to be ineffective. The reason is the presence of an oxide shell that surrounds the gold seeds, creating a barrier for the chemical etchant (Figure 8). The mechanism of its formation is not yet completely clear.

We have proposed the following scheme (Figure 6) [6]: at the end of the growth Silicon atoms (blue dot) are present in the catalyst (green hemisphere) at a temperature higher than the eutectic point.

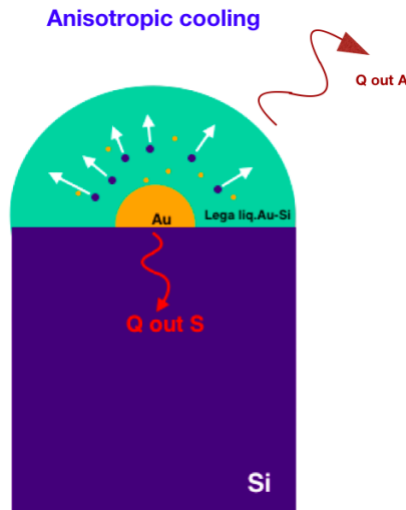


Figure 6: Schematic illustrating the mechanisms of anisotropic cooling leading the SiO_2 layer formation around the SiNWs tip.

The phase separation that occurs in the eutectic during the NW cooling causes the isotropic precipitation of the Si outside the droplet (see white arrows).

To explain how it is possible, we have to consider the kinetics of cooling. We have two heat dissipation fluxes: heat flux $Q_{\text{out-A}}$, that is convective toward the outside of the drop and $Q_{\text{out-S}}$ conductive toward the inner solid silicon. $Q_{\text{out-S}}$ is more efficient than $Q_{\text{out-A}}$. As a consequence, the cooling and the subsequent solidification starts from the inner core of the droplet and moves toward the surface. Thus, Si atoms segregate at the surface that is warmer than the core; by solidifying it generates a thin reactive Si shell on the metal surface, as we can see in the EF-TEM map of silicon in Figure 7 (red arrow).

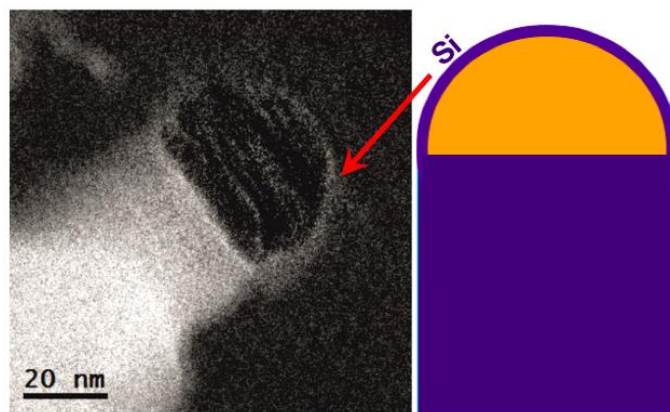


Figure 7: TEM micrograph silicon map (a) Schematic (b) [6].

The air exposure results in its oxidation, thus forming the silicon oxide SiO_2 coat surrounding the gold dot as the oxygen map in Figure 8 shows (see light-blue arrow)

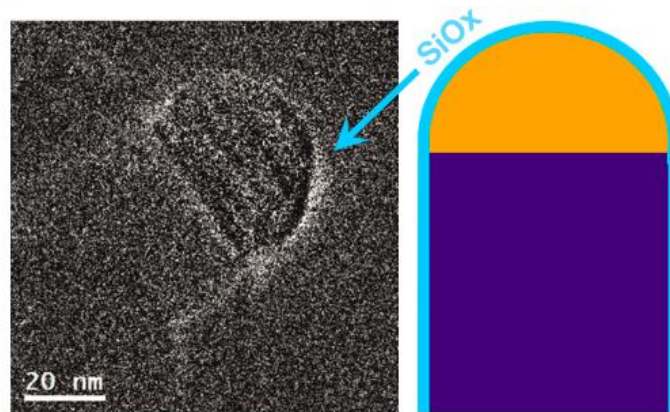


Figure 8: TEM micrograph oxygen map (a) Schematic (b) [6].

Taking into account the above, SiNWs underwent a two-step procedure post VLS growth allowing the effective Au removal: first the sample was immersed for 5 min in a HF buffered solution diluted in H_2O (1:10) in order to allow the SiO_2 shell removal; subsequently it was treated by a commercial gold etch solution (Fujifilm gold etch II w/OHS), containing sodium iodide (NaI) and iodine (I_2), diluted in H_2O (1:10) for 4 min. The whole etching process lasts 9 min.

The TEM images in Figure 9 show two nanowires that have undergone, only the classic gold etching (a) and the new two-step process (b) respectively. As we can see in the first case gold residues are present at the top of the wire, in the second one the gold is removed effectively and no residues are detectable.

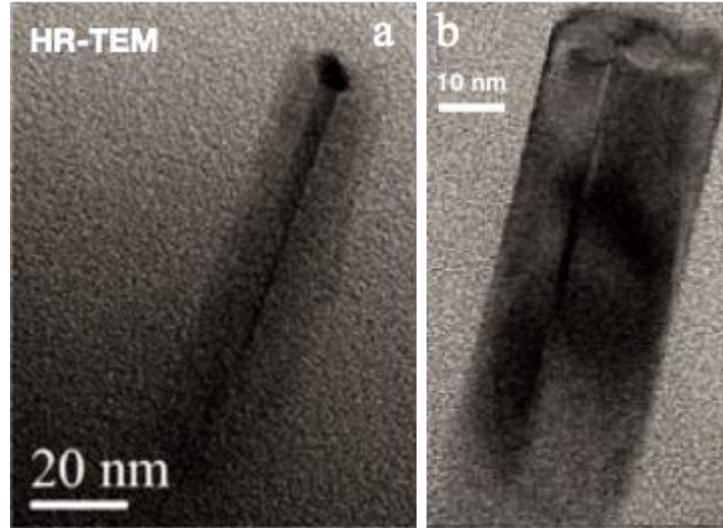


Figure 9: Cross-sectional view of TEM micrographs of SiNWs after the gold removal single step (a), and after the two-step gold etching (b) [6].

To evaluate the developed process efficiency, X-ray photoelectron spectroscopy was performed. In Figure 10 Si and Au spectra are reported for three samples: the as-grown (blue line), a sample which underwent only the Au etching with the classic solution (black line) and the sample obtained after the new two-step procedure (red line). The XPS Si region is shown in Figure 10a. The 2p spectral region of all the samples exhibit a doublet at 99.0 eV attributed to the elemental state of the silicon in the SiNWs. A band centered at 103.5 eV (typical of the SiO₂) is detected in the spectra of both the as-grown sample and in that obtained after the only Au etching step. The SiO₂/Si intensity ratio is comparable in the two spectra, thus indicating that the Au removal process does not remove the oxide. The use of HF in the double step procedure for the third sample (red curve) allows to completely remove the SiO₂, as stated by the absence of a peak in the studied spectral region.

The comparison between the Au XPS signals of all the NW samples is shown in Figure 10b. It presents a doublet due to the Au 4f peaks at 83.4 and 87.0 eV. As it can be noted, the Au signals intensity is low only in the sample treated with the new procedure indicating its Au removal efficiency. The quantitative data obtained after a calibration reveal that the percentage of the gold at the surface after the HF+Au etching is below 0.1%.

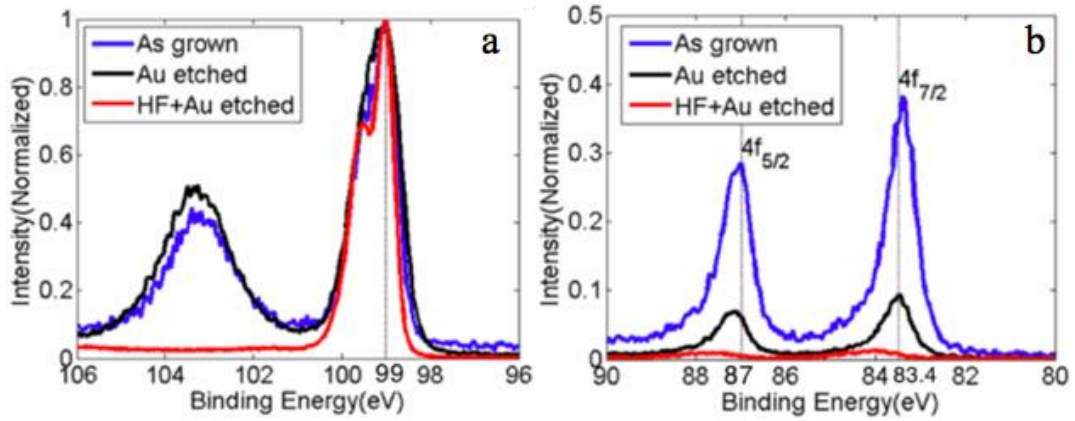


Figure 10: High resolution X-ray photoelectron spectra of the (a) Si 2p and (b) Au 4f of the as-grown nanowires (blue line), the sample obtained after the gold etching (black line) and the sample obtained after the two-step procedure (red line) [6].

The possible changes on the samples in terms of SiNWs density and diameter distribution have been also evaluated after each step of etching using SEM analysis on large statistics.

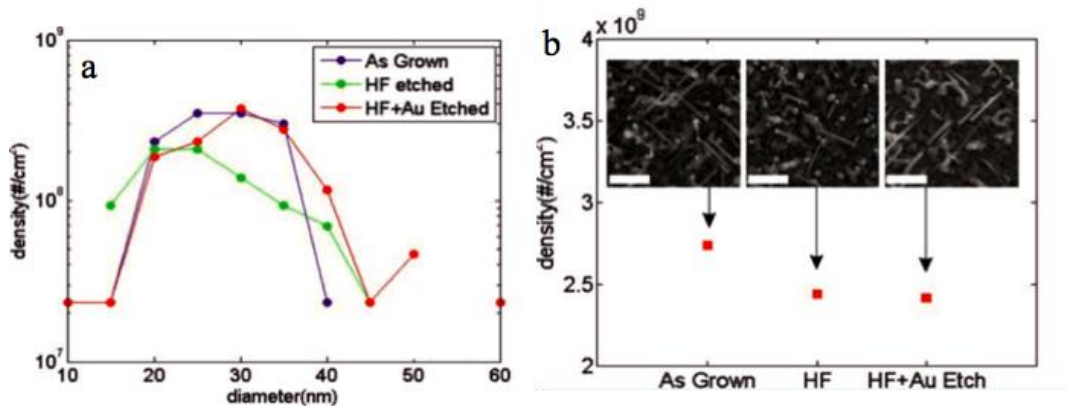


Figure 11: (a) SiNWs density as a function of diameter is reported for as-grown sample (blue circles), after the HF etching (green circles) and after HF + Au etching (red circles). (b) Average SiNWs surface density for the three cases under study. The inset shows the relative SEM micrograph in planar view scale markers corresponds to 400 nm [6].

The results for the as-grown samples (blue circles), for the sample after the single etching step with HF (green circles), and after the double step with HF + Au etching (red cycles) are reported in Figure 11. No significant difference between the diameter distribution of the as-deposited case and after the etching steps is observed. The density

of the structures also remains unchanged and almost fixed at 10^9 wire/cm, as can be seen from the SEM acquired in all three cases, hence the chemical reaction does not damage the samples.

Bibliography

- [1] <https://www.imm.cnr.it/source-sites/catania-hq>
- [2] Lewerenz H J and Bitzer T 1992 Electrolytic hydrogenation of silicon *J. Electrochem. Soc.* 139 L21
- [3] *Semicond. Sci. Technol.* 11 (1996) 415–421
- [4] Somashekhar, Ambika, and Sean O'Brien. "Etching SiO₂ films in aqueous 0.49% HF." *Journal of the Electrochemical Society* 143.9 (1996): 2885
- [5] R. Behrisch (ed.) (1981). *Sputtering by Particle bombardment*. Springer, Berlin. ISBN 978-3-540-10521-3
- [6] Puglisi, Rosaria A., et al. "Study on the physico-chemical properties of the Si nanowires surface." *Nanomaterials* 9.6 (2019): 818

Chapter 4

Plasmonic behavior in 30 nm SiNWs in diameter

It has been said that the nanosystem geometry determines variations in the plasmonic resonance features. However, it is not known how it specifically occurs in the case of SiNWs. Experimental reports on plasmon resonances (PR) in SiNWs are very few in literature, this is mainly due to the fact that is difficult obtain sub nanometer spatial resolution information, for reasons related to the characterization techniques as well as to the semiconductor material involved and the difficulty to fabricate wires with very small sizes.

Moreover, there are some contradictions in literature's works. Previous studies to our one, conducted by electron energy loss spectroscopy (EELS) on SiNWs, indeed revealed contributions at ca. 4-5 eV. They have been attributed to inter-band transitions in some cases [1,2], while in a later paper to plasmon resonance without between longitudinal or transverse nature [3]. There is, however, no direct observation, nor deep understanding in the current literature on low-energy PRs for isolated SiNWs smaller than 100 nm.

In the next sections we report different works we carried with the aim of mapping the localized modes in SiNWs; reveal their localized or propagating features; and monitor the nanostructure geometry role on the spectral behavior. The main technique used is the EELS coupled to the Energy Filtered Transmission Electron Microscopy (EFTEM).

In this chapter we present a study on plasmon behavior of isolated SiNW with Si core diameters of 30 nm and an oxide shell thickness of about 5 nm published in 2021 [4]. The SiNWs length is 420 nm with an aspect ratio of ca. 14. The SiNWs synthesis is conducted according to the procedures described in the previous chapter. The investigation is carried out through the electron energy loss spectroscopy (EELS) coupled to a scanning-transmission electron microscopy (STEM).

First of all, electron microscopy, the analysis technique, will be introduced very briefly.

4.1 Electron microscopy

The main difference between optical microscopy, the classic method for obtaining magnified images of microscopic systems, and electron microscopy is the probe particle used for the images generation. The first uses a beam of light to generate them, that is, photons as probe particles. An electron microscope, scanning (SEM) or transmission (TEM), instead uses an electrons beam. The use of electrons is advantageous as it increases the resolution. Indeed, the microscope resolution increases as the wavelength of the probe particle used decreases:

$$R = \frac{\lambda}{2n \sin\alpha}$$

Where R is the minimum distance at which two points of an object can be seen as separate using a particle beam of wavelength λ ; n is the medium refractive index and α is the lens aperture angle used.

Since the photons have a much longer wavelength than electrons, the resolution increases by several orders using electrons.

On the other hand, the main difference between the TEM and the SEM [5,6] is that, while the SEM generates the images by collecting the secondary, and back diffuse electrons that bounce off the sample, the TEM instead does it by collecting information from the electrons passing through it. Moreover, in the second case, as the name implies, the electrons must “transmit” through the sample and thus require a very thin sample.

4.2 Electron energy loss spectroscopy

Electron energy loss spectroscopy (EELS) [7] measures the energy distribution of electrons that pass through a thin sample to get all sorts of information and also create images. EELS instrumentation is typically incorporated into a TEM or a scanning TEM (STEM) tool, since EELS also uses transmitted electrons. The electrons can interact either elastically (no energy exchange) or inelastically with the sample, and it is these latter interactions that EELS exploits to extract information about the sample. The amount of energy lost can be measured through an electronic spectrometer and interpreted based on what caused the loss compared to the initial beam energy (zero loss peak).

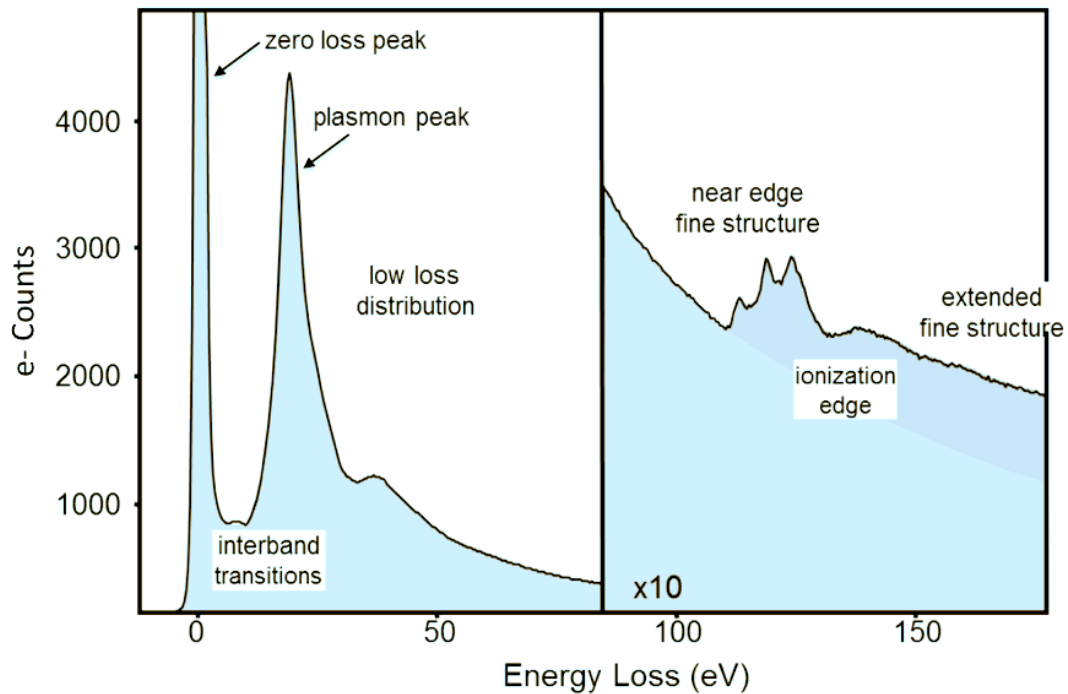


Figure 1: Scheme of a theoretical EELS spectrum, where the zero loss peak, the plasmon resonance and peaks in energy loss caused by core levels (fine structures) are indicated [7].

EELS data consists of both energy loss spectral information from the sample (spectroscopy) or images with contrast created through the material energy loss properties knowledge (energy-filtered, EFTEM). These methods can be combined in a technique called spectrum imaging, in which spectral information is collected in a spatially resolved manner. This data is used to extract a large amount of information from the sample due to inelastic interactions, including phonon excitations, transitions within and between energy bands, inner shell ionizations, as well as that of our interest i.e. plasmon excitation.

4.3 EELS/EFTEM analysis

Mapping the localized modes in semiconductor nanostructures, as SiNWs, helps reveal their localized nature and monitor the nanostructure geometry role. Nevertheless, their experimental investigation in the low energy range has long been a technical challenge due to the lack of suitable techniques. The possibility to acquire EELS spectra with high energy resolution and from nm-sized sample portions allowed us to overcome the old limitations and obtain new information, previously inaccessible.

The sample insertion into the analysis instrument required a particular procedure which consists of a mechanical stripping through which the SiNWs, from the wafer on which they were grown, are collected on a thin round metal mesh grid of a few millimeters square in diameter.

We conducted our STEM/EELS analyses at 200 kV using a JEOL JEM-ARM200F cold FEG microscope and EELS by a Gatan Quantum ER spectrometer. The inherent spectrum image acquisition mode provided a 3D datacube containing the 2D dark-field STEM image of the NW and the low-loss spectrum point by point simultaneously. In our experimental acquisitions, we conducted a 2D primary beam scan across a single NW, using a pixel size of 1.3 nm and 0.25 eV per pixel on the 2 K Gatan camera. The EELS energy range of the EELS spectrum resulted as 50 eV with an energy resolution of 0.45 eV. We applied a standard power-law fitting procedure with slits placed between 1.5 and 2.5 eV to remove the zero loss from all raw spectra.

A 21 pixel-wide binning furthermore reduced the EELS spectra signal-to-noise ratio. The 2D energy-filtered spectrum images (EFSI) consisted of a slice of the background-corrected datacube using a slit of 0.3–1 eV.

Figure 1a shows two EELS spectra, vertically shifted for a clear view, extracted from two different SiNW regions. The images only show half of the SiNW, being resonance symmetric. The blue curve is an extract from the SiNW internal area (blue box) and the red curve from the surface region (red box). The dominant signal in both cases is the one centered at about 17 eV, related to the Si volume PR [8]. Its intensity in the blue curve is relatively greater than that it has in the red one due to the greater Si bulk fraction sampled during the surface area acquisition. A signal at 8.5 eV is present in both cases, whereas at 4.5 eV another signal arises only in the case of the SiNW core scanning (vertical line).

From this result, we observe that the low-energy EELS spectrum characteristics vary according to the sampled region; hence, they spatially depend on the SiNW's spectral behavior during the interaction with the electromagnetic field. Moreover, the spectral

shape, especially in the low-energy region, suggests multiple contributions underneath the one indicated. Therefore, we chose an investigation methodology consisting of the acquisition of two types of EELS scans along the SiNWs' axial and radial directions, using smaller acquisition boxes. Figure 1b shows these axial scan results. The curves are correlated with the equally colored boxes in the energy- filtered transmission electron microscopy (EFTEM) map at 17 eV on the right. To verify the absence of parasitic signals, we started the scan by extracting the data from an external spot (red box lower left and red curve).

The red curve marks the background noise. The green curve, acquired in the external areas of the SiNWs (green box), shows the absence of the 17 eV peak, as expected, and two peaks at energies lower than 6 eV, as discussed later. The two low-energy contributions, at around 4.5 and 8.5 eV (Figure 1a), are now clearly distinguishable, as soon as the scan enters the NW, with modulation in intensity in some cases. The 8.5 eV signal is present, with an almost invariant intensity, for the entire wire length (magenta and ocher arrows), whereas the 4.5 eV signal undergoes an intensity drop near the tip at 55 nm of height taken from the SiNW base (gray arrow). The 4.5 eV signal decreases, confirming a spatial dependence on the spectral behavior. The signal intensity at 8.5 eV appears greater than the 4.5 eV signal intensity all along the NW, also due to the tails of the 17 eV peak. As anticipated above, some signals at energies lower than 6 eV are detectable even when the spectrum is acquired 10 nm away from the NW tip (green curve). This phenomenon is related to the large PR cross section, increasing the probability to generate plasmons also relatively far away from the wire edge and to the delocalized nature of electrons, producing the so-called scattering delocalization. We expect its coupling efficiency to be frequency dependent, with larger extension for lower energies [9]. Indeed, as described earlier, the peak at higher energy, 17 eV, disappears in the green curve.

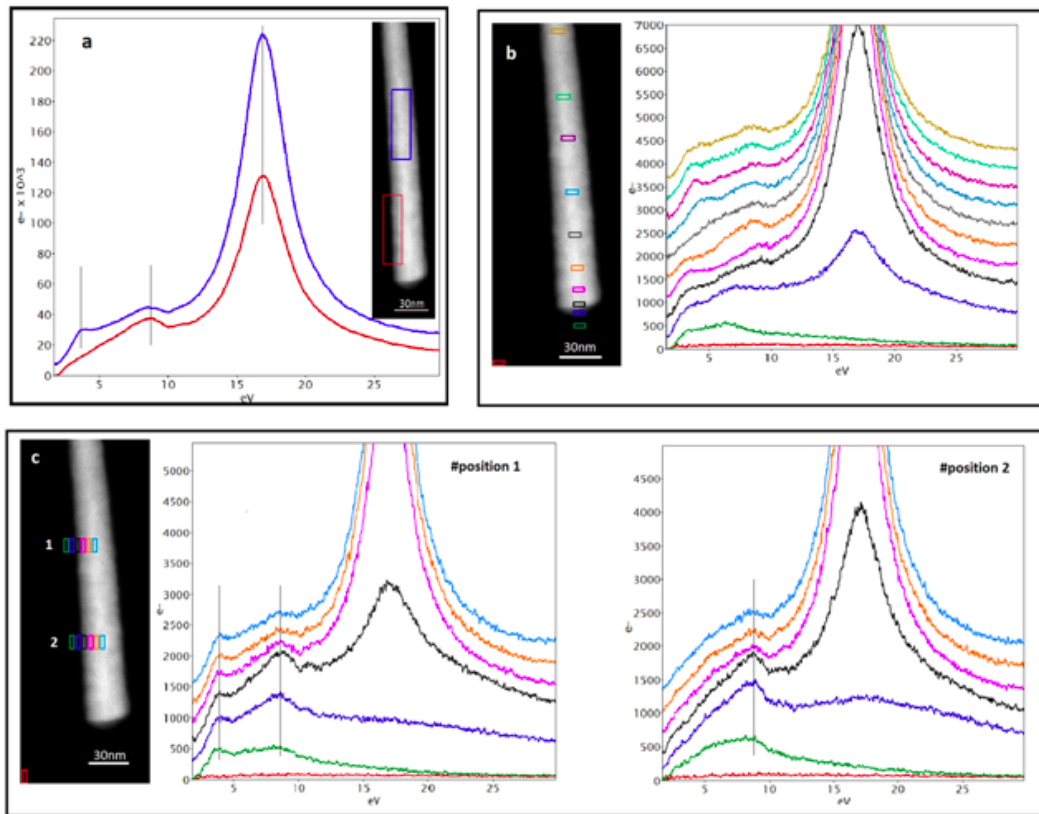


Figure 1: a) EELS spectra acquired on two different areas of the SiNWs, imaged in the inset (vertically shifted for clearview). We Acquired The Blue curve in the NW central region (blue rectangle) and the red one in the surface region close to the NW base (red rectangle). To optimize the analyzed area, we chose rectangle sizes of $63 \times 18 \text{ nm}^2$. The vertical lines depicted on the curves indicate three main peaks. Inset: EFTEM image obtained using the Si bulk plasmon energy loss at 17 eV. b) EELS spectra, acquired in several positions along the NW growth axis. We acquired every curve in the corresponding box with the same color as indicated in the NW EFTEM image on the right. To properly investigate the spectrum spatial dependence, we chose a box size of $12 \times 3 \text{ nm}^2$ as a compromise between the spatial resolution and the signal noise. Magenta and ocher arrows indicate a peak at 8.5 eV always present inside the NW; a peak at about 4.5 eV disappears (grey arrow) in the area near the wire end (gray box in the EFTEM). c) Spectra from radial scans acquired at two different heights: positions 1 and 2, corresponding to regions 1 and 2 in the EFTEM map reported on the right. The vertical lines highlight the significant contributions.

Figure 1c shows the graphs with the radial scans acquired at two different NW heights: positions 1 and 2 (regions 1 and 2 in the EFTEM map on the right), chosen in correspondence with the high intensity and intensity drop of the 4.5 eV contribution. The vertical lines highlight the significant contributions. At position #1, both peaks are present, whereas in position #2, only the 8.5eV peak appears. At position 1, the difference concerning the axial scan is evident: the 8.5 eV signal is present along the entire wire radius but with decreasing intensity (black to light-blue curve), whereas the 4.5 eV signal exhibits an almost invariant intensity. At position 2, the disappearance of the 4.5 eV signal confirms the spatial dependence of the spectral behavior. Figure 1c, green lines, corresponding to the green boxes in the relative EFTEM, acquired radially outside the wire, shows the delocalization effect. The data shown in Figure 1 indicate that the peaks, confined in a small energy range, are not energetically isolated from each other.

4.4 Peak fit

We conducted the EELS spectra peak fitting with the freely available software Fityk [10]. After normalization and background removal, the EELS spectra- extracted pure signals revealed their peak position, amplitude, and line width. We chose Lorentzian fitting because it is a standard empirical approach [11]. Figure 2 reports the experimental axial (a-d) and radial (e-f) spectra (green curves) selected among the most important ones from the scanning results reported in Figure 1b-c, with relative peak fit (red curves). We selected the axial spectra (a-d) at four significant heights along the NW axis, as indicated in (g, horizontal rectangles): 8 nm, 55 nm, 140 nm and 210 nm, measured from the NWs base along the red arrow. The radial spectra (e-f) were selected at two heights on the NW surface (vertical rectangles): 140 nm and 55 nm. Vertical lines (light blue and magenta) in the spectra highlight the most significant peaks (position #1 and #2 of Figure 1c). The signals at 10.7 – 12.4 eV correspond to the Si surface signal, the peak at about 22.3 eV, relative to the SiO₂ volume PR and the 33.3 eV peak relative to the Si bulk plasmon second order [12].

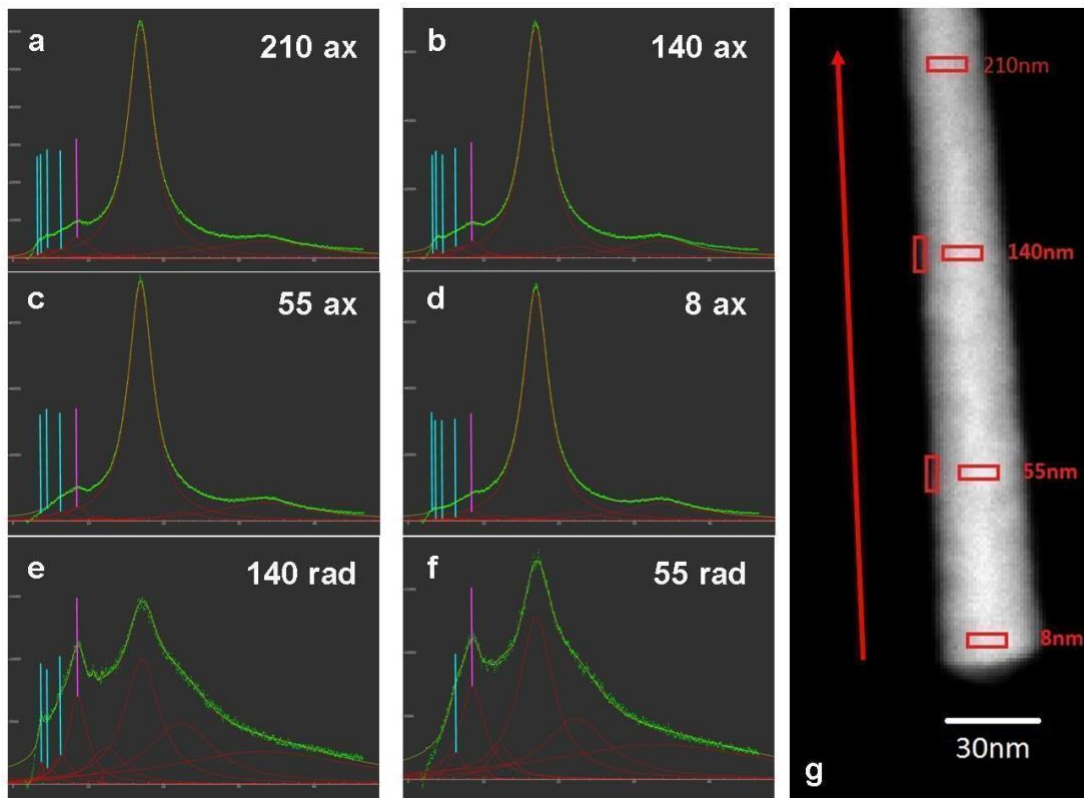


Figure 2: Axial (a-d) and radial (e-f) spectra (green curves) selected from the scanning results reported in Fig.1(b-c), with relative peak fit (red curves). The axial spectra (a-d) were selected at four significant heights along the NW axis, as indicated in (g): 8 nm, 55 nm, 140 nm and 210 nm (horizontal rectangles), measured from the NWs base. While the radial spectra (e-f) were selected at two heights on the NW surface (vertical rectangles): 140 nm and 55 nm. Vertical lines in the spectra highlight the most significant peaks.

The most interesting region is the low energy range, where several longitudinal PR modes, characteristic of the traveling waves, can be identified from 3.7 up to 6.4 eV, corresponding to the several harmonics, together with the localized surface plasmon, characteristic of the transverse resonant mode at 8.5 eV. In the axial spectra, acquired at 210 and 8 nm of height, the peaks relative to all the harmonics are visible, while at 55 nm some contributions exhibit low intensity, thus confirming the observations made in Figure 1b, grey box. In the radial spectra the harmonics and the localized mode appear with high intensity, also due to the lower intensity of the bulk signals and the high surface signal sampling. Our data match well with the harmonics observed by STEM in silver nanoparticles. The resonance spots showed in that case

different spectral energy responses depending on the position: tip, side or nanostructure center.

The PR can also be visualized by keeping track of a particular mode over the entire SI mapping, to directly plot the signal intensity falling into a particular energy slice over the EFSI [11]. The resultant PR map can be considered as the amplitude distribution of this particular resonant mode. When analyzing metallic nanostructures, the density of free electrons is very high and as a consequence the plasmon signals, both in energy and in the maps are intense and well separated. In semiconductors the resonance spots are expected to be less intense and more spatially and energetically diffused, due to the fact that the signal comes from the valence band electrons.

4.5 EFSI spatial maps

After peak analysis, EELS maps were acquired to visualize the EELS signal spatial distribution with subnanometer resolution within and around the nanostructure at relevant energy values. Figure 3a shows the energy-filtered spectroscopic image (EFSI) maps acquired at four different energies.

Here only four energies are shown and not five as in figure 2a-b-d, we will see later why.

The yellow regions, indicated by the white arrows, and corresponding to the higher electron intensity, showcase discrete spots attributable to a nano-resonator's harmonic behavior. They reveal the fundamental harmonic at 3.7 eV with one spot (and the other one symmetrically at the other tip, not imaged), the second harmonic at 4.5 eV with three spots (close to the ends and at the center of the SiNW), and the third one at 5.8 eV with four spots in total. The spots are located along the long NW axis, indicating the waves traveling back and forth between the NW ends. Hence, the surface PR modes represent an interplay between a traveling surface plasmon, also referred to as the SPP, and the resonator, induced by the NW length. The positions of all the experimental spots appear slightly shifted toward the NW end. We address this effect to the reflection mechanism of the SPP wave at the NW ends, as observed in silver nanorods [13]. At the tip, supposedly playing the oscillator node's role, there is an omnipresent, low, but nonzero signal that we address to the well-known point effect causing field enhancement.

At 8.5 eV, a strong signal located at the Si/SiO₂ interface along the NW walls is evident. We attribute this resonance to the transverse PR, also referred to as LSP, as occurring in spherical particles, too [3, 14]. The interface plays the role of a confining well for radial resonance. The comparison between the first three images and the last one teaches the difference in the spatial charge distributions between longitudinal and transverse modes. The map at 8.5 eV also reports a graph with a red curve showing the signal profile intensity acquired in correspondence to the black box along the indicated portion of the NW wall. The signal profile intensity shows peaks and valleys. We observed this result systematically on all of the NWs analyzed. This phenomenon has never been reported nor theorized so far in the literature, and it suggests a discrete modal behavior also for the LSP. It could be due to periodic charge distribution along the NW walls, probably related to a constructive/destructive interference mechanism; so, it is interesting to conduct deeper investigations in the future. The colored rectangles in Figure 3a indicate the regions from which the EELS signal profiles reported in (b) are radially extracted, at the significant heights along the NW. As is evident, all the profiles are flat except the 8.5eV, corresponding to LSP, which present two peaks at the NW walls, corresponding to the harmonic oscillator wells. Figure 3c shows the EELS signal profiles acquired axially at the same energies as in (a). It displays the signal profiles mediated on the entire NW surface (white rectangle) along the axial direction for fixed energy values. Several intensity spots appear at different positions for several energies, clearly indicating the harmonic peaks, whereas, as expected, the intensity remains constant all along the SiNW for transverse excitation. Our experimental data on the propagating SPPs match well with the harmonics observed by STEM in silver nanoparticles [15, 11]. The interplay between the SPPs and the resonator observed in our SiNWs is similar to the observations in metallic NWs [16]. When analyzing metallic nanostructures, however, the density of free electrons is very high, and as a consequence, the plasmon signals, both in energy and in the maps, are intense and well separated. In semiconductors, on the contrary, one expects the resonance spots to be less intense and more spatially and energetically diffused as the signal comes from the valence band electrons [17]. Our experimental findings confirm these expectations. Some literature findings regarding PR in semiconductor NWs anticipated the longitudinal modes' appearance [1,2, 14]. Nevertheless, these studies highlighted only two peaks in the spectra, at 4.2 and 8.2 eV, with the data not resolved enough to identify other peaks. Moreover, the spot

visualization in the maps was not clear for low spatial resolution of the technique used, so the article discusses a uniform intensity along the longitudinal direction. Our work demonstrates that it is possible to identify the resonance spots using proper characterization, acquisition scanning, and data analysis. Moreover, the literature attributes a peak at 8.2 eV to the multipolar mode of a longitudinal oscillation with the charge distributed in alternate ways along the radial direction, even though the authors attributed the peak to a longitudinal wave. Due to our observations, the 8.5 eV mode has a maximum intensity in correspondence with the NW walls, and we consequently ascribe it to the LSP. In contrast, the multiple lower-energy modes' intensity is distributed along the axial direction, pertaining them to the longitudinal waves. This evidence indicates that the harmonics originate from traveling charge oscillations along the longitudinal direction on the SiNW surface. On the contrary, the 8.5 eV mode originates from localized charge oscillations oriented transversely and then blocked by the NW walls, acting as quantum wells.

These results evidence the fundamentally different nature of these two classes of resonances, correlated with these Si nanostructures' two orthogonal dimensions.

At the end of the SiNWs' growth process, there may be gold atoms coming from the catalyst residues inside the NWs. For this reason, to exclude false conclusions from our energy maps, we subjected the materials to a chemical removal process of gold, which has an efficiency better than 99.9%, before the TEM [18] analysis. We investigated the role these gold atoms might play on the PRs. In literature, the PR peak of SiNWs grown by gold catalysis, referred to as the Au—Si plasmon, is found at 11–12.5 eV [19], significantly different from that at 4 or 8.5 eV, as visible in our experiments. Moreover, previous authors expected that the PR effect is due to an extended interface between a metal film and the semiconductor. Here we did not observe any metallic films on the SiNWs, and we expect any gold residuals to take the form of dispersed atoms exclusively. Therefore, it could be excluded that the observed signals are due to gold.

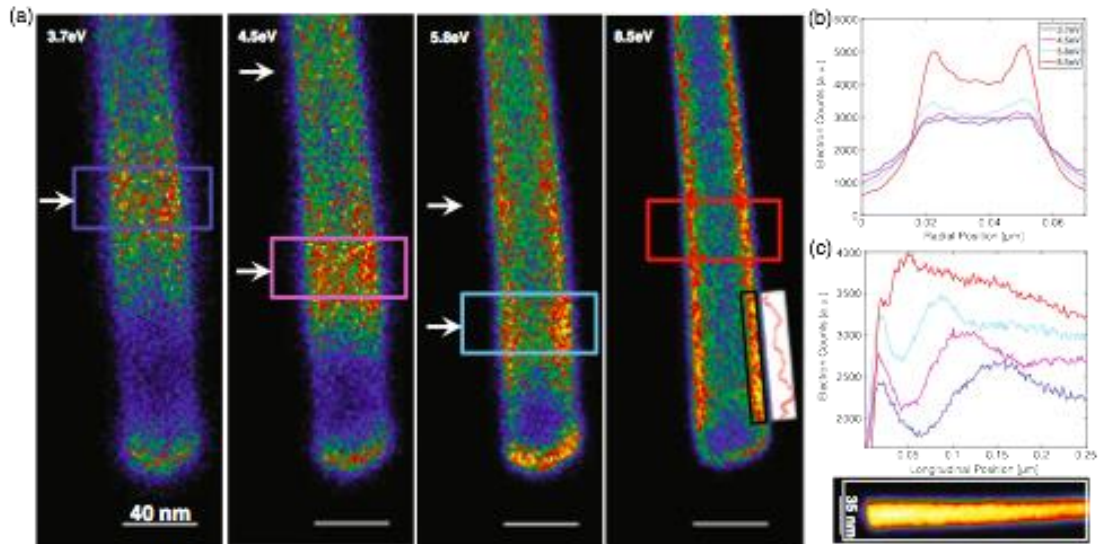


Figure 3: (a) EFSI maps acquired at four different energies, only half of the NW imaged. The second harmonic at 4.5 eV with two visible spots, and the third at 5.8 eV. The resonance at 8.5 eV corresponds to the transverse PR. Colored rectangles indicate the areas from which the EELS signal profiles in (b) are radially extracted, at different heights. (c) EELS signal profiles axially acquired at the same energies. Inset in (c): Intensity map acquired at 17 eV; the white rectangle indicates the signal extraction area.

4.6 Theoretical simulations

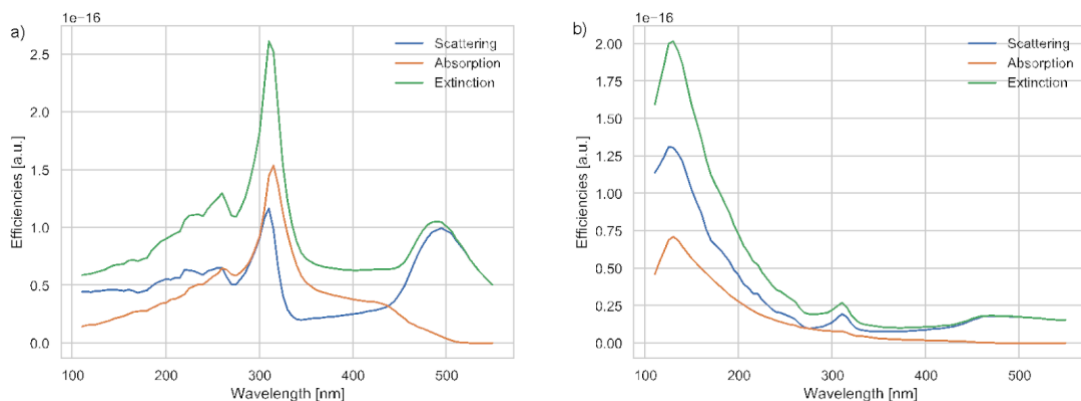


Figure 4: DFT-calculated complex dispersion data for bulk silicon: a) complex refractive index (n) versus wavelength, and b) corresponding complex relative electric permittivity versus photon energy. The real part (blue curve) reveals a negative real part for energy levels beyond 4 eV, a well-known prerequisite for the existence of

surface plasmons, with a decaying imaginary part, corresponding to optical losses, towards higher energies.

We performed numerical simulations to deeply understand and verify our experimental findings, modeling the optical dispersion data and the SiNW's resonant behavior under optical excitation. Due to a lack of reliable material data for Si at high energies in the literature, we first performed first-principles density functional theory (DFT) calculations on bulk Si. Subsequently, we extracted the corresponding complex optical dispersion data (Figure 4).

The calculated complex relative electric permittivity reveals a negative real part for energy levels beyond 4 eV (Figure 4b, blue curve), a well-known prerequisite for the existence of surface plasmons [20]. At the same time, its real part (orange curve), corresponding to optical losses, decays towards higher energies.

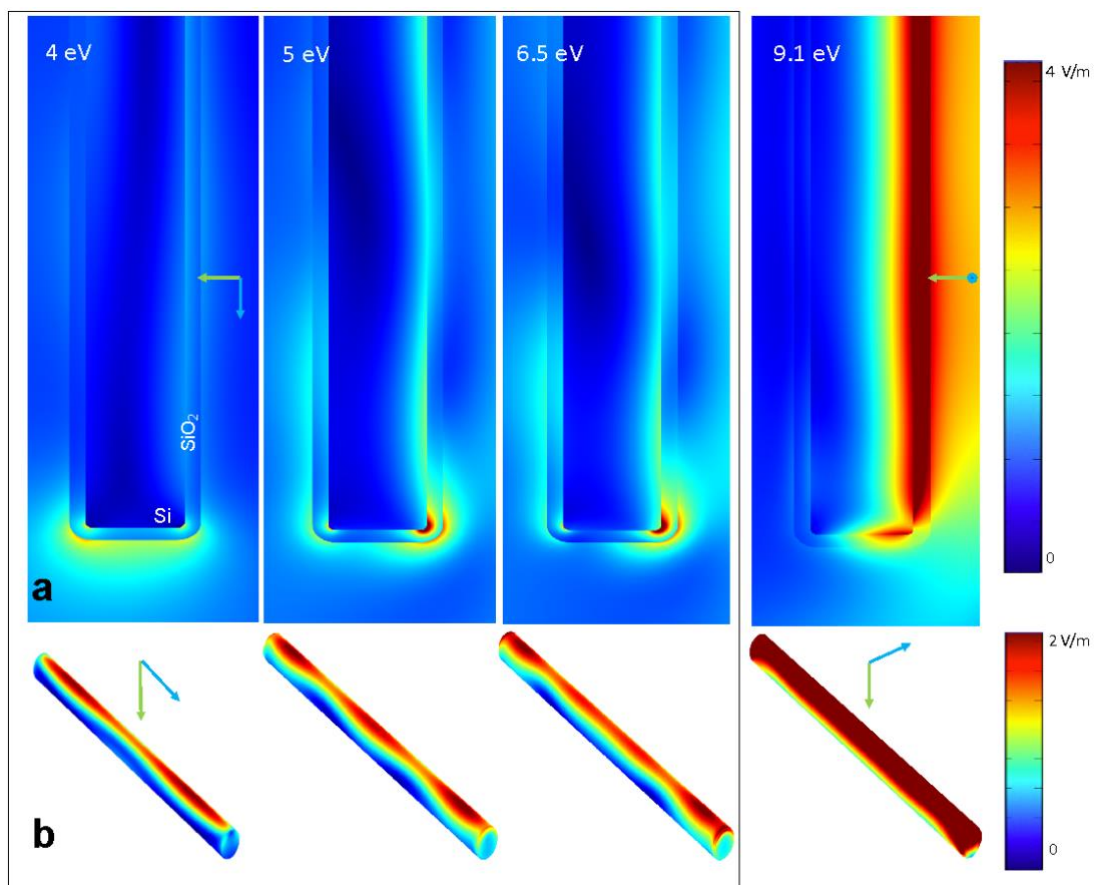


Figure 5: Optical simulations of isolated SiNWs confirm the experimental findings: a plane wave, impinging perpendicularly to the long NW axis (light green arrows), excites the structure. Displayed here are the resulting simulated longitudinal and

transverse resonant energy states (E-field magnitude [V m⁻¹]), between 4.0 eV and 9.1 eV. The images show the resulting electric field magnitudes in and around the nanostructure, in vertical cross-sections (half NW length) displaying the Si core and the surrounding SiO₂ shell and vacuum (a) as well as three-dimensional field intensity plots on the interface between Si core and SiO₂ shell (b). Under longitudinal polarization of the impinging wave (light blue arrow, black box), the excited structure comprises longitudinal standing wave patterns corresponding to the longitudinal harmonics of SPP resonances at discrete energies, with two (4.0 eV), three (5.0 eV) and four (6.5 eV) intensity lobes on the Si-SiO₂ interface, plus a pronounced field enhancement on the NW tips inside the shell region. Under transversely polarized excitation (light blue arrow, 9.1 eV), the structure exhibits the transverse LSP mode at higher energy, well separated from the longitudinal traveling surface modes.

Based on these dispersive material data, our electrodynamic simulations reveal optically excited, discrete surface energy states, corresponding to the above-discussed PR: under a longitudinally polarized impinging plane wave excitation, the structure comprises longitudinal standing wave patterns corresponding to the longitudinal SPP resonance harmonics at discrete energies, with two, three, and four intensity lobes at the interface between the Si core and the SiO₂ shell, at 4.0, 5.0, and 6.5 eV, respectively, alongside the omnipresent strong field enhancement spots located on the NW tips, extending through the shell and the close surroundings. Under transversely polarized excitation, the structure exhibits the LSP mode at high energy (9.1 eV), which appears uniform also inside the nanostructure (Figure 5). We are reminded that, when observed by TEM (Figure 1), the signal intensity is higher at the SiNWs borders than at the center due to the integration effect at the borders. Our numerical results strongly suggest that our experimental observations arise from the (weighed) integration of field profiles perpendicular to the main wire axis, including the evanescent fields stemming from the Si core and the SiO₂ shell, and mainly confined inside the latter. The full spectral extinction profiles for both excitations further support this claim (Figure 4). We address the slight mismatch in resonance energies, as compared to our experimental findings, to the introduced uncertainty via the material models and the shell structure: firstly, the DFT-calculated Si data refers to bulk Si, neglecting confinement effects arising from the NW geometry and lattice

effects arising from the specific NW axis growth. Secondly, the SiO₂ shell parameter choices (stoichiometry, morphology) might further influence the resonance.

Here, for the sake of completeness, we present optically excited near-field maps at the resonance positions for both longitudinal and perpendicular excitations (Figure 4). We note that the momentum conservation necessary to excite the plasmons in the longitudinal polarization case is not directly possible with the applied k-vector perpendicular to the main SiNW axis. Instead, it is established by a tip-induced multi-directional scattering of the incident wave, matching the momentum conservation angle concerning the core-shell interface. This effect, however, also creates a strong tip resonance, clearly visible in the near-field maps (Figure 7), and exaggerated compared to the electrically excited experimental results. Moreover, the numerically calculated optically excited near-fields differ from the experimental results by the directionality induced by the incident field's k-vector.

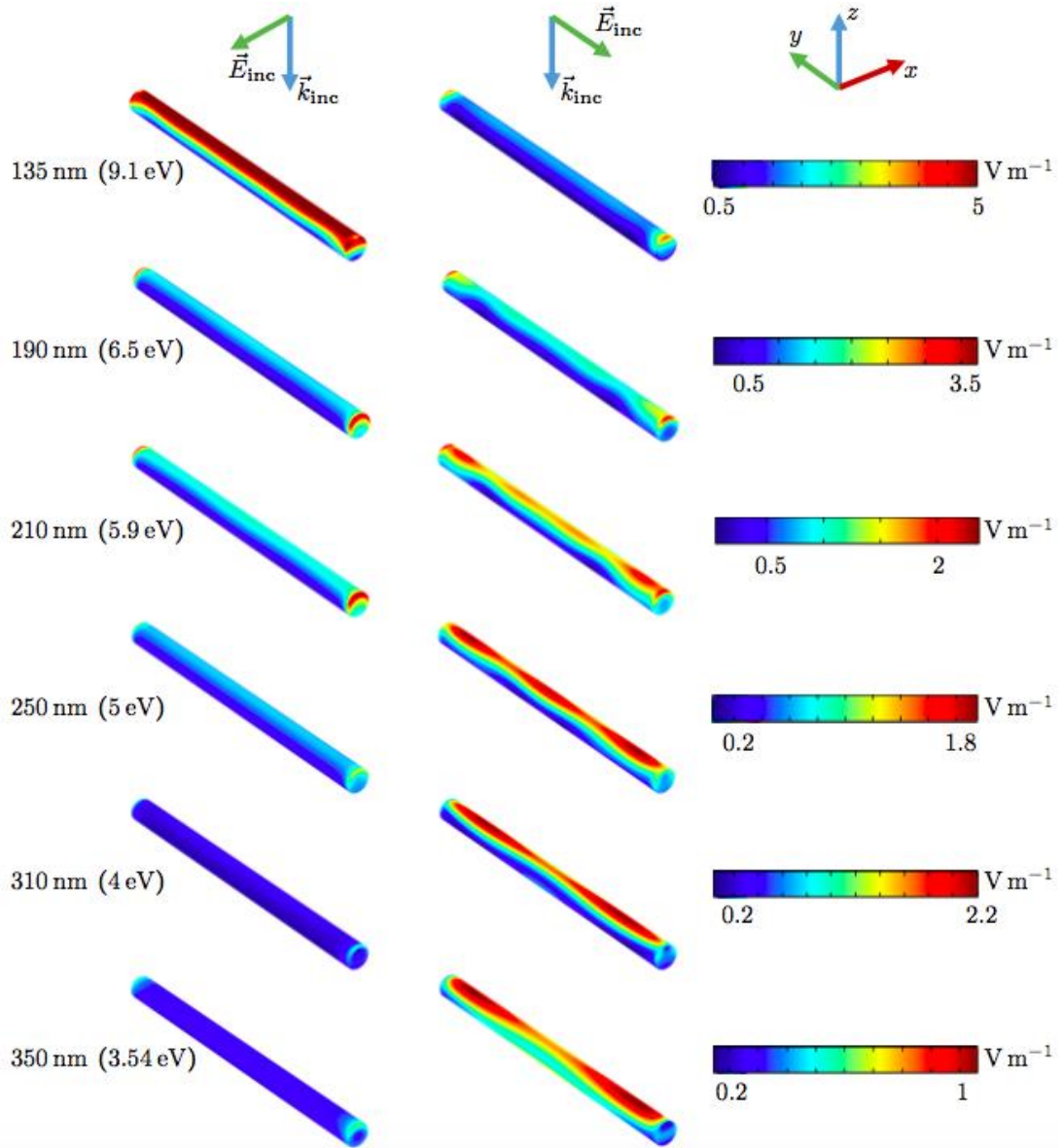


Figure 7: Local electrical field intensities $|E|$ at the interface between the SiNW core and the silicon oxide shell, excited by a linearly polarized electromagnetic plane wave. The incident field k -vector k_{inc} always points in negative z -direction. The rows correspond to the (experimental and numerical) resonance energies discussed in the main text. Left column: Incident electric field E_{inc} linearly polarized perpendicularly to the long SiNW axis. A strong transverse resonance occurs at 9.1 eV (LSP), whereas no further strong resonances occur for lower energies. Right column: E_{inc} polarized along the long SiNW axis, shown for the longitudinal (TSP) resonance energies discussed in the main text. Both polarizations reveal a strong tip effect beyond 5 eV.

While further investigations might lead to a higher-grade quantitative match, our numerical findings qualitatively prove the experimental claims. The experimental and theoretical results illustrated so far and in mutual agreement point to the conclusion that SiNWs exhibit plasmon resonances, similar to those found in metallic NWs. The second evidence is that these electronic oscillations fall in two categories, longitudinal and transversal, confined by the nanostructure geometry.

Optical Simulations

FEM simulations of isolated Si NWs are conducted using the wave optics module of the commercially available FEM solver COMSOL Multiphysics [21]. We modeled the experimentally investigated NW by a 30 nm-diameter Si cylindrical core, surrounded by a 5 nm-thick silicon dioxide (SiO_2) shell. We assumed a total NW length of 420 nm, with slightly rounded tips to avoid exaggerated edge effects. The NW was embedded in a spherical vacuum domain, surrounded by perfectly matched layer (PML) boundaries to mimic an infinite outer domain. We excited the structure with a background electromagnetic plane wave (wavelengths between 110 and 550 nm, corresponding to energies between 11.27 and 2.25 eV, respectively), with an electrical field amplitude of 1 Vm^{-1} , impinging perpendicularly to the long NW axis (green arrows in Figure 5). We conducted separate simulation sweeps with the electrical field polarization in parallel and orthogonal to the long NW axis (blue arrows in Figure 5). The final setup comprised 6 635 940 degrees of freedom (per wavelength). We modeled the crucial Si and SiO_2 material influence on the optical simulations via complex-valued, dispersive refractive index data. The SiO_2 data set was based on literature values [22]. Due to a lack of literature reports on Si dispersion data for energy levels beyond 4 eV, we generated the more critical Si data set via in-house first-principles calculations, using the DFT method (SIESTA package [23], for details on our simulation, we refer to Supporting Information). We subsequently irradiated the structure by an incident unpolarized electromagnetic wave to excite the electronic transitions between orbitals, giving rise to the dielectric function imaginary part from the integral of momentum matrix elements between occupied and empty states around the Fermi level [24,25]. Finally, we deduced the dielectric function real part via the Kramers–Kronig relations [26,27].

4.7 Conclusions

In this section we investigated the plasmon occurrence and behavior in 30 nm- wide SiNWs, through the combination of two powerful characterization techniques, STEM and EELS, providing high spatial and energy resolution. We acquired the spectra as functions of the position inside the SiNWs by scanning the beam along the axial and radial direction. This high-resolution scanning allowed us to identify the spectral response for both traveling and localized resonant modes for these SiNWs in the energy range between 3.7 and 8.5 eV. We classify the observed signals as low-energy plasmonic resonances, further by our dispersive material data calculations. The energy maps clearly show discrete intensity spots with axial symmetries for the longitudinal oscillations. In an energy region well separated from the longitudinal propagating waves, we demonstrated the transverse LSP oscillations existence, visualizing them for the first time to our knowledge. Our electromagnetic simulations on the optical properties and plasmon responses of the SiNWs strongly support our experimental findings of resonant longitudinal surface plasmon states and well-separated transverse localized plasmons. Furthermore, our study unexpectedly revealed fine-scale features, such as intensity modulation along the NW walls, resembling the longitudinal waves' quantization. Finally, our high-resolution methodology revealed that the longitudinal plasmons' wavelength shows a compression toward the NW tips. The possibility of exploiting these SiNWs as resonant cavities represents a great potentiality for advancing nano-optics, and the excellent integration capacity offered by silicon for broad on-chip optoelectronic applications practically sustains this potentiality.

Bibliography

- [1] B. W. Reed, J. M. Chen, N. C. Mac Donald, J. Silcox, G. F. Bertsch, *Phys. Rev. B: Condens. Matter Mater. Phys.* 1999, 60, 5641.
- [2] J. Kikkawa, S. Takeda, Y. Sato, M. Terauchi, *Phys. Rev. B – Condens. Matter Mater. Phys.* 2007, 75, 245317.
- [3] J. Wang, X. J. Wang, Y. Jiao, M. W. Chu, M. Malac, Q. Li, *Nanoscale* 2010, 2, 681.
- [4] Borgh et al. "Surface Plasmons in Silicon Nanowires." *Advanced Photonics Research* (2021): 2100130
- [5] Hayat, M. *Basic techniques for transmission electron microscopy*. Elsevier, 2012.
- [6] Vernon-Parry, K. D. "Scanning electron microscopy: an introduction." *III-Vs Review* 13.4 (2000): 40-44.
- [7] Egerton, Ray F. *Electron energy-loss spectroscopy in the electron microscope*. Springer Science & Business Media, 2011.
- [8] I. Alber, W. Sigle, S. Müller, R. Neumann, O. Picht, M. Rauber, P. A. Van Aken, M. E. Toimil-Molaes, *ACS Nano* 2011, 5, 9845.
- [9] R. F. Egerton, *Ultramicroscopy* 2007, 107, 575.
- [10] Fityk—Curve Fitting and Peak Fitting Software—Fityk 1.3.1 manual, <https://fityk.nieto.pl/> (accessed: April 2020).
- [11] Y. Wu, G. Li, J. P. Camden, *Chem. Rev.* 2018, 118, 2994.
- [12] EELS investigation of luminescent nanoporous p-type silicon I. Berbezier a,* , J.M. Martin b, C. Bernardi c, j. Derrien a
- [13] O. Nicoletti, M. Wubs, N. A. Mortensen, W. Sigle, P. A. van Aken, P. A. Midgley, *Opt. Express* 2011, 19, 15371.
- [14] J. Wang, X. J. Wang, Y. Jiao, Q. Li, M. W. Chu, M. Malac, *Appl. Phys. Lett.* 2009, 95, 133102.
- [15] A. Losquin, M. Kociak, *ACS Photonics* 2015, 2, 1619.
- [16] D. Rossouw, M. Couillard, J. Vickery, E. Kumacheva, G. A. Botton, *Nano Lett.* 2011, 11, 1499.
- [17] R. F. Egerton, *Physical Principles of Electron Microscopy: An Introduction to TEM, SEM, and AEM*, 2nd ed., Springer International Publishing, New York 2016.
- [18] R. A. Puglisi, C. Bongiorno, G. Borgh, E. Fazio, C. Garozzo, G. Mannino, F. Neri, G. Pellegrino, S. Scalese, A. La Magna, *Nanomaterials* 2019, 9, 818.

- [19] B. S. Swain, B. P. Swain, N. M. Hwang, *J. Appl. Phys.* 2010, 108, 073709.
- [20] P. West, S. Ishii, G. Naik, N. Emani, V. Shalaev, A. Boltasseva, *Laser Photon. Rev.* 2010, 4, 795.
- [21] COMSOL—Software for Multiphysics Simulation, <https://www.comsol.com/> (accessed: July 2021).
- [22] L. Gao, R. Lemarchand, M. Lequime, *J. Eur. Opt. Soc.* 2013, 8, 13010. [40] J. M. Soler, E. Artacho, J. D. Gale, A. García, J. Junquera, P. Ordejón, D. Sánchez-Portal, *J. Phys. Condens. Matter* 2002, 14, 2745.
- [23] J. M. Soler, E. Artacho, J. D. Gale, A. García, J. Junquera, P. Ordejón, D. Sánchez-Portal, *J. Phys. Condens. Matter* 2002, 14, 2745.
- [24] A. Shabani, M. K. Nezhad, N. Rahmani, Y. K. Mishra, B. Sanyal, J. Adam, *Adv. Photonics Res.* 2021, 2, 2000086.
- [25] J. P. Perdew, K. Burke, M. Ernzerhof, *Phys. Rev. Lett.* 1996, 77, 3865. [43] J. Zemann, *Acta Crystallogr.* 1965, 18, 139.
- [26] J. Zemann, *Acta Crystallogr.* 1965, 18, 139.
- [27] H. J. Monkhorst, J. D. Pack, *Phys. Rev. B* 1976, 13, 5188.

Chapter 5

Plasmonic behavior of SiNWs between 10 e 30 nm in diameter

This chapter focuses on the size variation effect on the SiNWs plasmonic behavior. The study is still pursued through the coupled STEM / EELS technique.

Isolated SiNWs with medium Si core diameters equal to 12.5, 26.25 and 34 nm and an oxide shell thickness between 1.4 - 2.5 nm are analyzed. Their lengths are respectively 189 nm, 411 nm and 314 nm. We neglect the SiO₂ thickness variation effect for now. Also, in these cases the SiNWs synthesis and collection for analysis occurred according to the procedures described above.

We evaluate the EELS spectral features in the energy range between about 3.7 and 10 eV, the electric field spatial distribution and understand how it varies by changing the wires dimension. In the previous chapter we demonstrated that SiNWs with a silicon core of about 30 nm and an oxide shell of about 5 nm behave as a harmonic nanoresonator, showing multiple nodes/antinodes spots like to nanorods / wires of metallic material, such as Ag and Au [1] or of semiconductor material, such as ZnO although thicker than the wires in this work [2].

5.1 EFSI maps

The Figure1 depicts the EFSI maps acquired for a SiNW with an average Si core diameter of 34 nm, 314 nm long, having a SiO₂ shell thick 1.4 nm. The maps refer to different energies at which the maximum intensity of the nodes are observed: 3.9 eV, 4.5 eV, 5.3 eV, 6.5 eV and 8.5 eV.

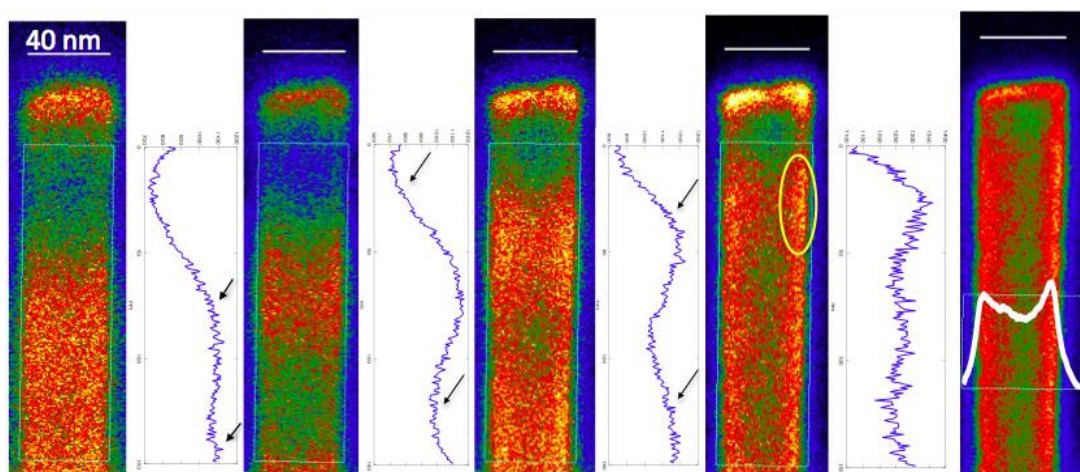


Figure 1: EFSI maps acquired at five different energies, for a wire with Si core diameter of 34 nm, 314 nm long, having a SiO₂ shell thick 1.4 nm. Only half of the NW is imaged depicting the harmonics at different energies: (a) 3.9 eV, (b) 4.5 eV, (c) 5.3 eV, (d) 6.5 eV. The resonance at 8.5 eV (e) corresponds to the transverse PR. White rectangles indicate the areas from which the EELS signal profiles, spectra on the right of each map, are axially extracted.

Figure 1a corresponds to the map at 3.9 eV. It clearly shows an extended area with a relatively intense signal spot distributed symmetrically along the major wire axis. We can note that, also in this NW, a very intense spot is localized on the wire tip and that the intensity signal falls down a few tens of nanometers far from it. Then it starts to get up again by moving towards the wire center. If we look at the signal intensity profile (the blue curve in the graph on the right) we note that this signal spot is the sum of two contributions: a first large peak at the center of the graph completely shown and a part of a second one, noticeable away from the tip, where the intensity curve again rises (see the two black arrows). The signals are attributed to the first fundamental harmonic relative to the longitudinal propagating surface plasmon polariton (SPP). For that first order mode, according to the results discussed in the previous chapter, we expect to observe two intensity spots located axially near the tips, and therefore only one for half NW. In this case, only one spot is observed in the half of the wire and part of the second spot which should not be visible as it is related to the other half of the wire not shown. The second spot appears instead partially because the wire is slightly tapered and, as is known in the literature, this compresses the distribution spots of the field in the thinnest part of the structure, forcing them to move closer towards the wider one, breaking the symmetry of the distribution even if only to a small extent, as we see. The intense signal present on the NW tip is attributed to the tip effect enhancement as for the 30 nm wire previously discussed.

Figure 1b shows the EFSI 4.5 eV map in which we easily note the presence of a lobe and a half along the axis and for symmetry, we deduce the presence of three lobes in total on the entire wire, as expected for the second harmonic of longitudinal SPR. Indeed, in this case we observe two well defined regions where the spot intensity decreases: near the tip and far from it towards the wire center (see the two black arrows). We also note that the first lobe is now closer to the tip as a consequence of the major order of the harmonic mode. The relative signal intensity profile on the right

(blue curve) highlights as said. On the tip the electric field is high also in this case although with smaller intensity.

At 5.3 eV (Figure 1c) we observe the presence of two lobes (see the two black arrows in signal profile on the right) and for symmetry four spots distributed along the major axis, considering the two wire halves as the third harmonic should have. It can be seen quite easily that the spot adjacent to the wire tip is even closer to it than the lower order mode (comparing the intensity profiles of different orders) and that on the tip is present the high intensity signal due to the tip enhancement.

In Figure 1d at 6.5 eV it is possible to glimpse the fourth harmonic with two and a half spots in the middle of the wire, therefore five spots present in the NW entire length. The intensity signal profile helps to figure their distribution. The fourth harmonic spots are less separated and intense than the previous case, as it is known that the intensity decreases as the order increases; moreover, the intensity spots do not appear circular but elongated (see yellow oval) which tend to overlap more as the order of harmonics increases.

For this SiNWs class dimension we can state that the behavior is a little different from that of the wire studied in the previous chapter as expected since the harmonic energy values are slightly shifted. We attribute this to the different wire length that represents the most important parameter that influences the spots intensity distribution in a nanoresonator.

However, we can conclude that the spot harmonic behavior of the longitudinal resonance family is confirmed as expected and that the number of maximum intensity spots density grows with increasing energy.

The map in the Figure 1 extracted at 8.5 eV shows instead the LSPR signal having transversal nature at well separated energy with respect to the longitudinal modes. That plasmonic signal is located at the interface between Si and SiO₂ as shown by the intensity profile (white curve) in the inset in line with what has been observed for the 30 nm wire case.

Neglecting the effect of the variation in the thickness of the SiO₂ shell, it can be stated that the plasmonic behavior for this dimensional class of wires is in line to the class examined in the chapter 4, it is reasonable because the variation in the diameter is equal to about 7.5%.

Figure 2 can be read in the same way to the previous one; the yellow arrows indicate the wire half. The EFSI maps are reported for just over half wire, having an average

diameter of 26.25 nm, at the different most significant energies: 3.9 eV, 4.5 eV, 5.3 eV, 6.3 eV and 8.5 eV.

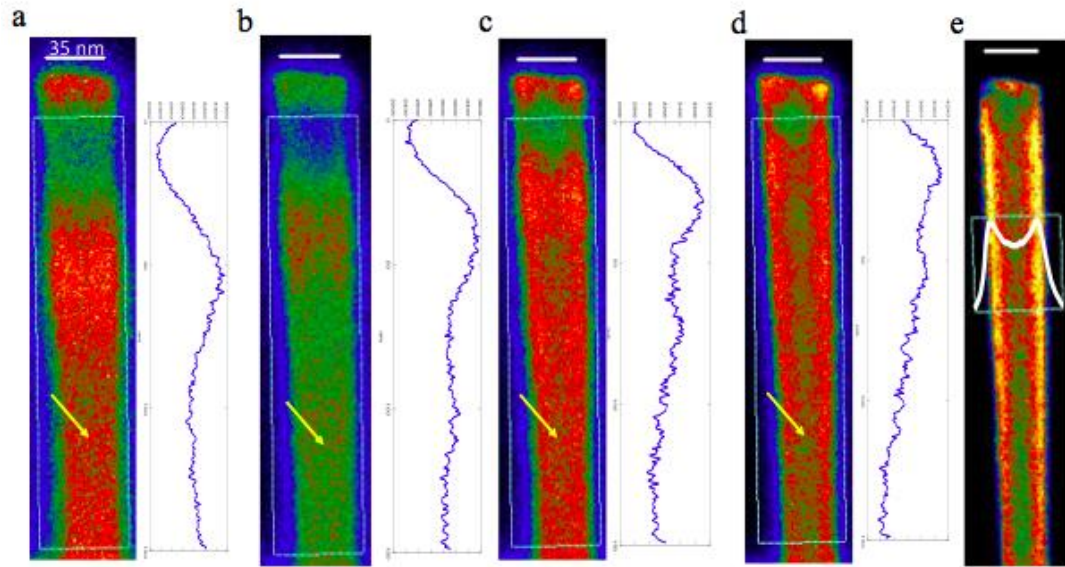


Figure 2: EFSI maps acquired at five different energies, for a wire with Si core diameter of 26.25 nm, 411 nm long, having a SiO₂ shell thick 1.4 nm. Only half of the NW imaged depicts the harmonics at different energies: (a) 3.9 eV, (b) 4.5 eV, (c) 5.3 eV, (d) 6.3 eV. The resonance at 8.5 eV (e) corresponds to the transverse PR. White rectangles indicate the areas from which the EELS signal profiles, spectra on the right of each map, are axially extracted. The yellow arrows indicate the SiNW half.

We can see that also in this case the behavior recorded for the previous two wire classes is observed. At 3.9 eV we find a double spot, one for each of the two halves of the wire, due to the fundamental longitudinal harmonic. If we check the 4.5, 5.3 and 6.3 eV EFSI map in Figure 2b-d and their relative intensity profiles on the right (blue curves) we find exactly the same situation seen for the previous wire cases. We confirm that the intensity spots increase in number with increasing energy and the spatial distribution is unaltered. So, we can state that longitudinal resonant modes continue to manifest themselves with the known harmonic behavior.

Figure 2e shows the 8.5 eV EFSI map, it is again observed that the maximum of the transverse PR peak intensity profile, extracted from the white rectangle, is localized at the interface between the semiconductor and oxide shell (white curve in the inset) confirming the transverse nature of this oscillation. No sensitive energy shifts are detected compared to previous cases for both vibrations families.

Figure 3 shows once again the EFSI maps of the electric field spatial distribution processed for a SiNW with an average diameter of 12.5 nm and 189 nm in length. The maps are readable once again in the same way as in the other cases discussed. The same energies are reported i.e. 3.9 eV, 4.5 eV, 5.3 eV, 6.5 eV and 8.5 eV to compare this result with the other SiNWs classes.

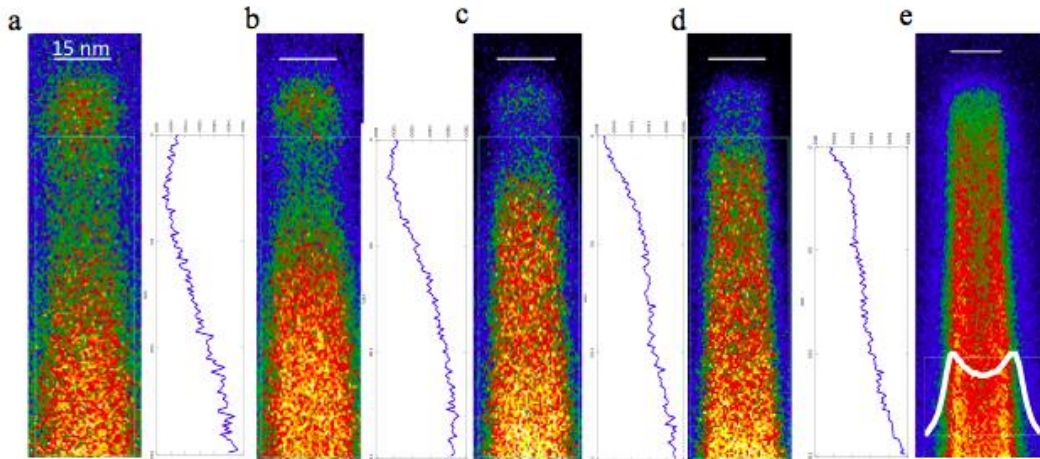


Figure 3: EFSI maps acquired at five different energies, for a wire with Si core diameter of 12.5 nm, 189 nm long, having a SiO₂ shell thick 1.4 nm. Only half of the NW imaged depicts the harmonics at different energies: 3.9 eV, 4.5 eV, 5.3 eV, 6.5 eV. The resonance at 8.5 eV corresponds to the transverse PR. White rectangles indicate the areas from which the EELS signal profiles, spectra on the right of each map, are axially extracted.

At first glance the first four EFSI maps up to energy equal to 6.5 eV (Figure 3a-d) seem to reveal an approximately uniform distribution along the major wire axis relative to the longitudinal plasmon signal despite energy varies. The discrete spots distribution, hitherto always observed, seems to be not present. Thus, the harmonic behavior seems to fail in this SiNWs size class since the well separated spots distribution of the longitudinal modes is not distinguishable.

A possible explanation of this evidence is that although this wire's dimensional class still behaves like a harmonic resonator, the maximum intensity spots are so close that they are not clearly distinguishable as in the previous cases (Figures 1-2). Indeed, if we look at the intensity profile graph at the 5.3 eV we note that the blue curve shows two rises by moving from the tip towards the NW center, though not well defined. It can be speculated that the intensity spots due to the harmonic behavior of longitudinal modes would be spatially compressed, overlapping themselves and appearing as if

they were a quasi single signal. This effect can be attributed to the reduced wire length (189nm) with respect to the previous ones (411 and 314nm), since the resonator length is the main parameter influencing the spatial distribution.

Therefore, we understand that the variation of the NWs radius in the range between 35 and 12 nm, has little influence on the plasmon behavior and on the harmonic intensity spots distribution. On the other hand, the effects of the variation in length are more marked. However, passing from 411 to 314 nm no significant variations are observed while passing from 314 to 189 nm the distribution of the spots considerably varies.

In addition, it is known in literature that Al nanorod dipole modes generally have lower quality factors with respect to noble metals plasmonic wires, for several reasons such as a combination of interband transition or to the presence of a surface oxide layer absent in noble metals. [3]. We can suppose these factors also affect the semiconductor nanostructures, even more it is reasonable that they are more marked in such small SiNWs making their plasmon resonances intensity spots inherently blurry.

However, it cannot be totally excluded that even the small size of the diameter, of the order of ten nanometers, plays some role, given that we are close to the Bohr radius around which quantum effects, not here investigated, begin to appear.

Regarding the transversal plasmon mode acquired at 8.5 eV, Figure 3e reveals the usual spatial distribution observed so far, well localized at the interface between the Si and the oxide, as the signal profile extracted from the white box (white curve in the inset) highlights once again.

5.2 Spectral features

In order to evaluate the size effect on the spectral features, we report in Figure 4 the superimposed EELS curves acquired for different SiNWs dimensions classes: 7.5, 12.5, 19.5, 26 and 34 nm. The spectra are extracted from the area highlighted by the red rectangle in the EFTEM map at 17 eV (Figure 4a) relative to the 12.25 nm wire illustrative of the way they have been extracted for all SiNWs classes. The rectangular area dimensions are different for each NW but with fixed proportion with respect to the wires size; note that the tip is excluded in all cases.

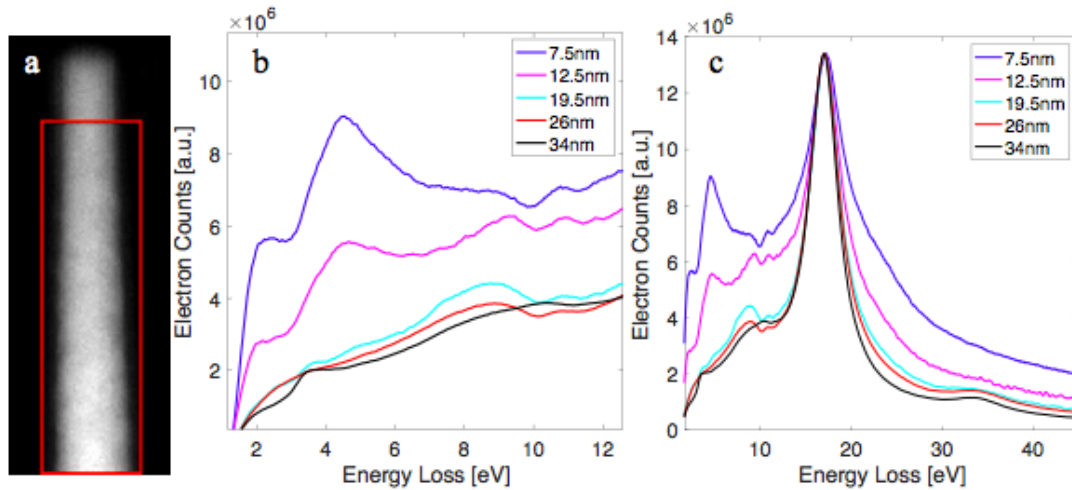


Figure 4: (a) EF-TEM map of a 12.5 nm diameter SiNW acquired at 17 eV. The red rectangle indicates the area from which the EELS spectra shown in (b) are extracted. (b) Superimposed EELS spectra acquired for five different diameter classes of SiNWs: 7.5 nm, 12.5 nm, 19.5 nm, 26 nm, 34 nm. (c) Magnification of spectra shown in (b) in the low energy range between 2 and 12 eV. plasmon peak at about 17 eV; a small shift toward higher energies is observed when the NW diameter decreases.

Figure 4b shows the entire spectral range acquired for the different wires class. All the spectra are normalized to the highest signal i.e. the bulk Si plasmon peak at 17 eV. Immediately catches the eye how the structure size variation affects above all the spectral features in the low energy range i.e. between 2-10 eV. Figure 4c shows a zoom of the same spectra in (a) in the energy range between 2 and 12 eV.

As can be seen, when the SiNW diameter increases, the signal at about 8.5 eV grows up in intensity while that at about 4.5 eV undergoes an attenuation. The dependence of the intensity of these signals on the nanostructures diameter has already been observed in the literature, although in that case a different nature has been indicated for them [4].

5.3 Conclusions

In this work the geometry variations effect on the low energy EELS plasmonic features for SiNWs have been studied. The dimensions, diameter and length, are varied, ranging respectively between about 34-12 nm and 189-411 nm. The results confirm that the SiNWs support two types of SPRs: the longitudinal modes and transverse ones. The longitudinal SPRs show a harmonic behaviour and distributes symmetrically along the major axis of the NWs.

We find that the transversal mode is sustained by the wires at well separated higher energies than the longitudinal ones and it is always located at the interface between Si and SiO₂. We speculate that there exists a sharp energy range, at about 3.9 eV, a few hundred of meV wide within which the SiNWs behaviour is intermediate between metallic and non-metallic.

We have also proposed that by reducing the wire length from 311 to 189 nm, the longitudinal harmonic spots are compressed. Moreover, we note that the relative intensity of the 8.5 eV and 4.5 eV signals are correlated and vary by changing the SiNWs diameter dimension. Finally, by considering the Si bulk plasmon peak we observe a little shift toward higher energies as the diameter wires decrease.

Bibliography

- [1] Qi, Ruishi, et al. "Probing Far-infrared surface phonon polaritons in semiconductor nanostructures at nanoscale." *Nano letters* 19.8 (2019): 5070-5076.
- [2] Wu, Yueying, Guoliang Li, and Jon P. Camden. "Probing nanoparticle plasmons with electron energy loss spectroscopy." *Chemical reviews* 118.6 (2017): 2994-3031.
- [3] Martin, J.; Kociak, M.; Mahfoud, Z.; Proust, J.; Gerard, D.; Plain, J. High-Resolution Imaging and Spectroscopy of Multipolar Plasmonic Resonances in Aluminum Nanoantennas. *Nano Lett.* 2014, 14, 5517–5523
- [4] Reed, B. W., et al. "Fabrication and STEM/EELS measurements of nanometer-scale silicon tips and filaments." *Physical Review B* 60.8 (1999): 5641

Chapter 6: Future perspectives

6.1 Plasmonics on SiNWs below 10 nm

One of the next steps to which this research aims is the understanding of the plasmonic behavior in SiNWs with a diameter of less than 10 nm, a dimension at which quantum effects become non-negligible. For this purpose, it was decided to analyze a wire with a diameter of about 7 nm and Figure 1 shows the EFSI maps for that wire.

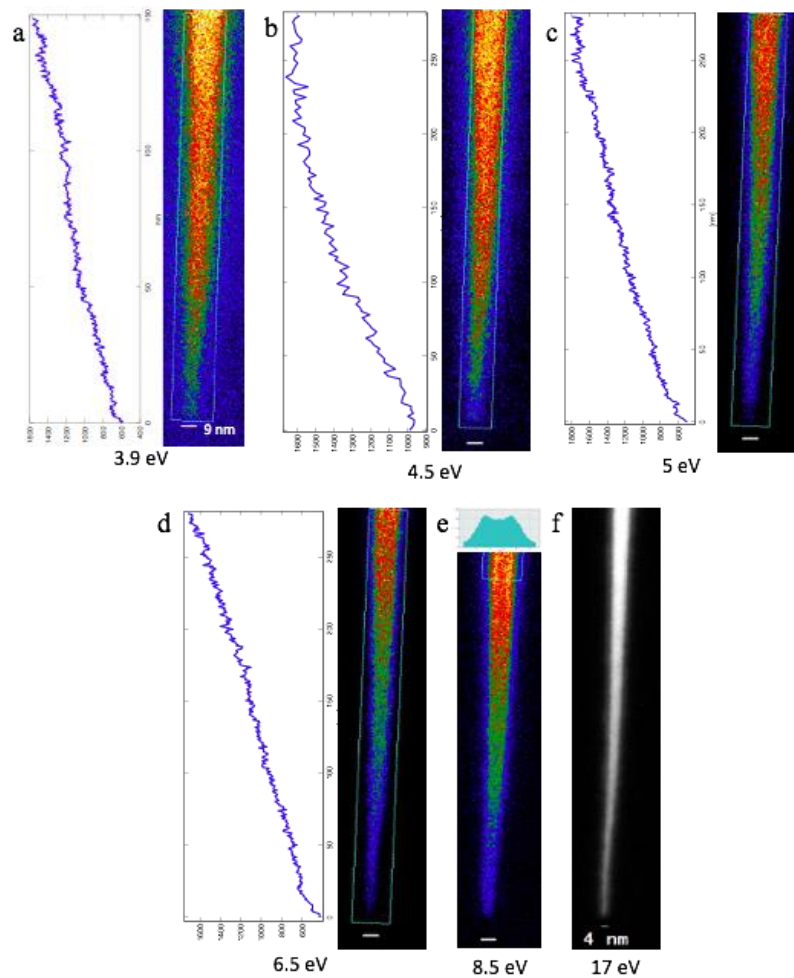


Figure 1: EFSI maps acquired at five different energies, for a wire with Si medium core diameter of 7 nm at different energies: (a) 3.9 eV, (b) 4.5 eV, (c) 5 eV, (d) 6.5 eV, (e) 8.5 eV. Only half of the NW is imaged. The resonance at 8.5 eV corresponds to the transverse PR. White rectangles indicate the areas from which the EELS signal profiles, on the right of each map, are extracted. (f) EFTEM map of the same wire acquired at 17 eV.

As we can summarily verify, it seems that the same behavior reported previously is still observed for the dimensionality class equal to 12.5 nm. This suggests that below a certain diameter, the longitudinal harmonic resonance behavior either does not manifest itself or is made indistinguishable by some not yet well understood phenomenon. While the transverse plasmon once again shows the characteristics always observed up to now, i.e. it is well localized at the silicon / oxide interface. Furthermore, these results lead to the exclusion that the length of the nanostructure plays a decisive role in the observed behavior given that the wire examined is over 350 nm long. This not entirely clear aspect will be the aim of the forthcoming investigations.

6.2 Plasmonics on SiNWs: shell oxide effect

In the first phase of the research, it was decided to neglect the effect of the thickness native oxide variation that encapsulates the nanowires on the plasmonic characteristics. Subsequently it was decided to investigate this aspect as well; however, the work is still in early stages.

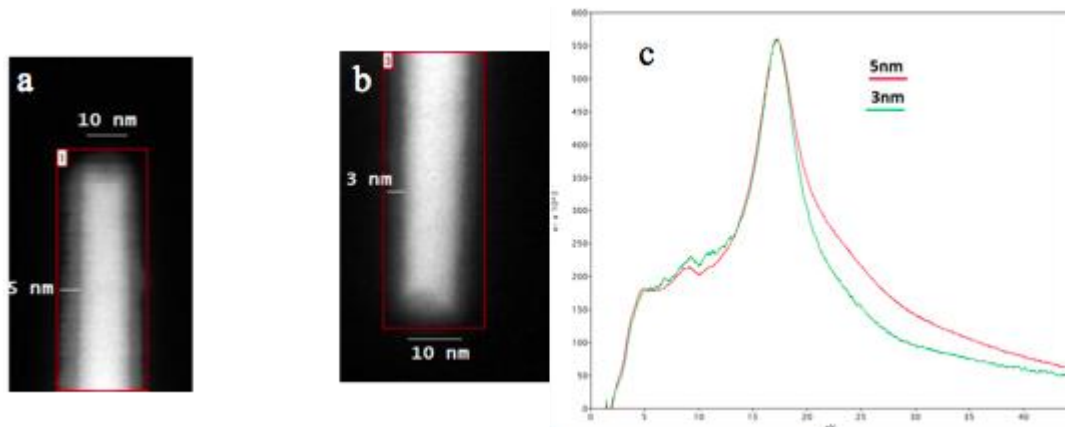


Figure 2: EFSI maps acquired at 17 eV for two different SiNWs with the same Si core diameter equal to 10 nm and different thickness of the oxide shell (a) 5 nm and (b) 3 nm. (c) ELLS spectra of the two NWs extracted from the areas defined by the red rectangles in a and b between 2 and 45 eV. The spectra are vertically aligned with respect to the most intense 17 eV Si bulk plasmon peak.

Figure 2 shows two EELS spectra extracted for two different SiNWs with the same core Si diameter, equal to 10 nm, in which the oxide shell thickness varies: it is equal to 3 nm in one case and 5 nm in the other one; the spectra are vertically aligned for a clear view. The signal at about 23 eV, which represents the bulk plasmon resonance energy of the silicon oxide, is more intense in case 5 nm than in case 3 nm thickness. This is reasonable given that the thickness of the oxide shell is greater in case 5 nm than in case 3 nm. The relative intensity of the spectral range between 2 and about 14 eV is instead inverted: indeed, we observe that the intensity of the spectrum in this range is greater when the thickness of the shell is smaller, this allows us to affirm with confidence that these signals are due to Si and not to oxide. These aspects represent only preliminary results and will also be investigated in the near future.

Chapter 7

Early stages of aluminum-doped zinc oxide deposited by sputtering on silicon nanowires

In this chapter a new investigation related to SiNWs potentialities are presented. The work was carried out in parallel during the PhD period and aims to be useful to the new generation electro-optic devices implementation with greater efficiency than the current ones and represents only the first step of an open line of research.

Aluminum-doped Zinc Oxide (AZO) is an electrically conductive and optically transparent material with many applications in optoelectronics, photovoltaics and in the new field of the plasmonic metamaterials. Most of its applications contemplate the use of complex and nanosized materials as substrates onto which the AZO forms the coating layer. Its morphological characteristics, especially the conformality and crystallographic structure, are crucial because they affect its opto-electrical response. Nevertheless, it is difficult to find literature data on AZO layers deposited on non-planar structures. We study the AZO growth on Silicon-NanoWires (SiNWs) to understand its morphological evolution when it is formed on quasi one-dimensional nanostructures. We deposit by sputtering different AZO thicknesses leading from nano-clusters until the complete SiNWs array incorporation. At the early stages, AZO forms crystalline nano-islands. These small clusters unexpectedly contain detectable Al, even in these preliminary phases, and show a wurtzite crystallographic structure. At higher thickness, they coalesce by forming a conformal polycrystalline shell over the nanostructured substrate. As the deposition time increases, the AZO conformal deposition leads to a polycrystalline matrix growing up between the SiNWs, until the complete array incorporation and planarization. After the early stages, an interesting phenomenon takes place leading to the formation of hook-curved SiNWs covered by AZO. These nanostructures are potentially very promising for optical, electro-optical and plasmonic applications.

7.1 Introduction

Silicon-NanoWires (SiNWs) are also used to engineer the emitter of new photodiodes class with a non-planar configuration [1] and can act as light-trapping structures to improve the optical path [2]. A transparent electrode in many of these technologies is required and the transparent conductive oxides (TCOs) are the most widely used materials [3,4]. TCOs must have a band-gap greater than 3.1 eV to be effective in transmitting photons of visible light without exciting electrons from the valence to the conduction band, granting improved structural, thermal and optical properties [5]. TCOs integration in the final devices is difficult and represents a current challenge, as it must meet some conditions like being conformal to the nanostructure geometry, as well as to ensure at the same time good opto-electrical properties and mechanical resistance. Moreover, it should be made of non-toxic, environmentally friendly, and inexpensive materials. A material that is gaining ground for large scale applications is Aluminum-doped Zinc Oxide (AZO). Solar cells, flat panel displays, light emitting diodes are just some of the devices already present in applications in which AZO is used [6-8]. This is because it improves lateral conductivity while maintaining good optical and surface passivation properties [9]. In AZO some Al^{3+} ions substitute some Zn^{2+} ions in the lattice. This is the reason why the Al doped ZnO has a higher electrical conductivity with respect to the undoped ZnO. Moreover, it has a direct wide band-gap of 3.37 eV and a large exciton binding energy of ~ 60 meV [10]. It is also mechanically resistant [11], exhibits an intrinsic n-type behavior due to crystal defects and allows heavy doping [12] besides being abundant, inexpensive and non-toxic [13]. The TCOs morphology affects the transparency of the component and the excitonic propagation length. Indeed, a good crystallinity is needed for both a good transparency and efficient excitonic propagation which controls the electrical conductivity [14]. Not only good electrical characteristics but also efficient passivation and chemical stability of the active area are essential for large-scale nano electro-optical applications, such as in SiNWs based diodes. Therefore, it is useful to understand the interaction between AZO and the structured substrate and how it evolves on SiNWs since the beginning of the deposition, because they rule the final characteristics of the material. Currently there is no literature available on the early deposition phases, especially when substrates with complex shapes, as in the case of SiNWs, are involved.

In this work we synthesize and study the system composed of the combination of AZO and SiNWs, by focusing on the early stages of AZO formation on the nanostructures. SiNWs arrays are grown via IP-CVD through the VLS mechanism, using Au clusters as catalysts [15]. The coating of NWs with AZO is pursued by sputtering. Sputtering is known to allow for faster processing and lower costs than other techniques, and does not require ultra-high vacuum conditions, indeed it is the most used for the TCO fabrication. We aim at investigating the nucleation and growth mechanisms and how the formation of the layer evolves as the amount of deposit increases. We characterize the materials through scanning SEM, TEM, STEM techniques. TEM Diffraction analysis is used to study the crystal lattice of the deposit. Energy Dispersive X-ray (EDX) Analysis and EELS are chosen for information on the chemical composition of the clusters and of the layers.

We show results on AZO-coated SiNWs in terms of chemical composition of the deposited material and its morphology, evaluating its conformality with respect to the substrates; we analyze the oxide structure at the atomic level, observing its crystalline nature and defining its phase from the first deposition steps up to hundred nanometers. In the early stages, the deposited AZO assembles on the nanowires in the form of nanoclusters decorating them all along their entire length. Characterizations reveal their nanocrystalline nature and phase. This study provides important insights for the application of AZO decorated SiNWs as transparent electrodes or innovative plasmon metamaterials. The plasmonic behavior of SiNWs is not yet completely rationalized in the near UV and visible region. It is known that the plasmonic characteristics and therefore the functionality of devices that exploit this phenomenon are sensitive to the material surrounding the structure through its refractive index. We expect then that it could be possible to modulate the plasmonic resonances of these nanosystems by controlling the morphology and the amount of deposited AZO. The wide application versatility together with the fact that the nanowires of silicon require a low cost to be manufactured, allow in the future, as well as in the already known photovoltaic sector, the use on large scale of such SiNWs / AZO combined systems also for plasmonic functionalities.

7.2 Methods

The SiNWs synthesis is conducted according to the procedures described in chapter 3. Then the wafer is cut into 2 cm² square pieces used for the AZO deposition. Each sample is introduced individually into the sputter deposition chamber. The AZO used as a target is a commercial disk (purity 99.9%). No rotation is imposed to the substrates during the depositions and their surface is parallel with respect to the source. The wafer holder is not purposely heated. The plasma is triggered by Radio frequency (RF). The pressure in the chamber is equal to about 3x10⁻³ mbar, power equal to 50W. The thickness of the deposited material is chosen on the basis of a previous calibration that returned a deposition rate equal to 0.04 nm/s. The process times chosen vary from a few seconds to about 4 hours for the thicker layers. Four different AZO equivalent thicknesses are deposited: 2 nm, 20 nm, 100 nm and 500 nm. The samples obtained are morphologically characterized by SEM, and by the EELS coupled with the TEM and STEM analysis. EDX analysis is performed to study the elemental composition of the samples and their spatial distribution.

7.3 Results and discussion

Figure 1 shows the SiNWs array after the CVD deposition used as a substrate for the AZO depositions. SiNWs have diameters ranging between 5 and 35 nm and lengths between 50 and 500 nm, in some cases reaching the micron. NWs are straight and oblique due to the crystallographic plane orientation effect of the Si substrate on which they are grown [16, 17].

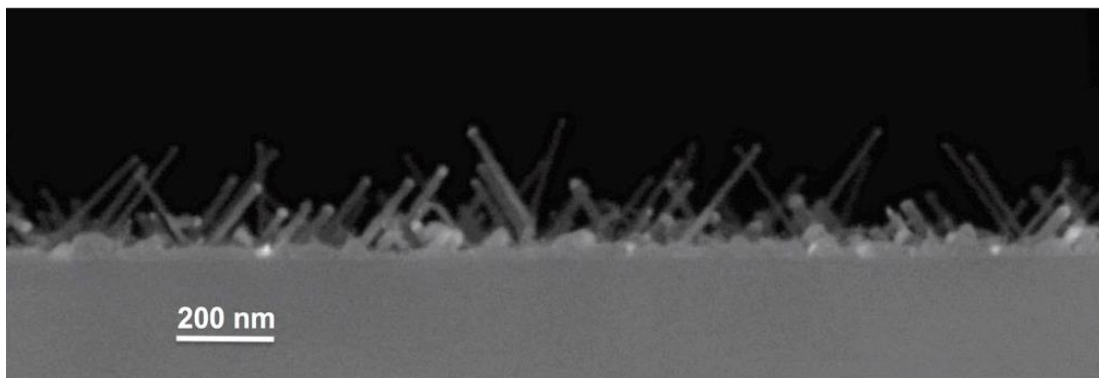


Figure 1. SEM microscograph in cross view of the as grown SiNW array after the CVD deposition used as substrate for the AZO depositions.

Figures 2a-c show one SiNW imaged in HAADF STEM mode from the sample subjected to the AZO deposition of 2 nm equivalent thickness, observed at different magnifications. Figure 2a reveals a clear deposit made of quasi-0-dimensional nano-clusters with sizes smaller than 10 nm and size-distributed on the surface.

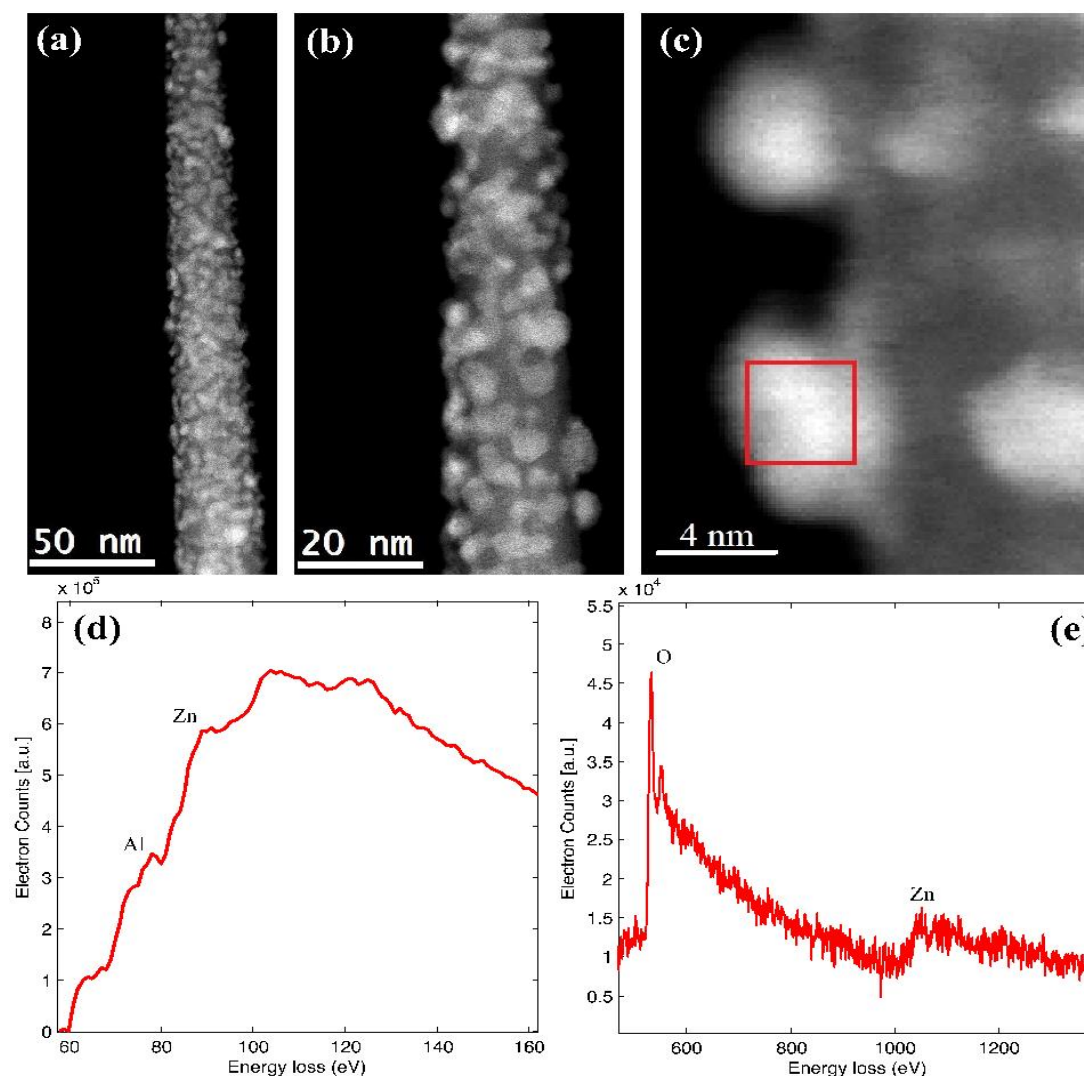


Figure 2. (a-c) STEM images at different magnifications for the AZO/SiNW system. The equivalent thickness of the deposited AZO layer is 2 nm; the diameter of the SiNW imaged is about 20 nm. The AZO cluster's diameter is smaller than 10 nm. (d, e) EELS spectra extracted from a significant region as shown by the red rectangle in (c).

Figures 2d-e report the EELS spectra in the most significant energy ranges i.e. from 70 to 160 eV and from 500 to 1400 eV respectively for the same SiNW, extracted

from the cluster region as indicated by the red box in the dark field STEM image in Figure 2c. The signal in Figure 2d at energies larger than 78 eV is due to Al *L*-edge, while the peak at about 90 eV is relative to the Zn3p [18]. The doublet located at 537 and 556 eV in Figure 2e is due to the O1s and the signals at about 1022 and 1045 eV are due to Zn2p 3/2 and 1/2 respectively [19]. The EELS spectrum backgrounds are subtracted using a power law model.

The data present in literature on the O peak, for planar AZO films, are mainly obtained by XPS analysis, with different energy scale calibration [20]. So our result obtained by EELS spectroscopy provides a new useful reference. The presence of the Zn and O EELS peaks indicates that the grain is composed of ZnO; the Al signal observed in the cluster structure confirms the presence of the metal atoms inside the grain suggesting that the sputtered material is in fact AZO and not simple ZnO, even at this low deposition thickness. This result is not obvious, because given the small size of the AZO clusters and the small amount of dopant it is difficult to characterize them and it is also statistically possible to have undoped nanostructures [21-26]. The Al signal at 78 eV in Fig. 2(d) can be ascribed to the Al-O bond, from literature findings, as expected for the Al doped ZnO which presents an atomic structure where the Al³⁺ ions substitute Zn²⁺ ions in the lattice [19, 27-29].

The lattice parameters and the degree of crystallinity of the deposited AZO are fundamental information because they determine its optical and electrical characteristics. Figure 3a shows the STEM image at high magnification of a NW deposited in the same conditions (as in Figure 2) for the previous sample, i.e. with 2 nm of AZO equivalent thickness. The lattice planes of the clusters are clearly distinguishable (see the inset, which is a magnification of one of the crystalline AZO grains), demonstrating their crystalline nature. The nanocrystals are oriented in different directions from each other. The signal intensity profile shown in Figure 3b is extracted from the light blue box shown in (a). The measured interplanar distance for the specific crystallographic direction results to be 2.48 Å.

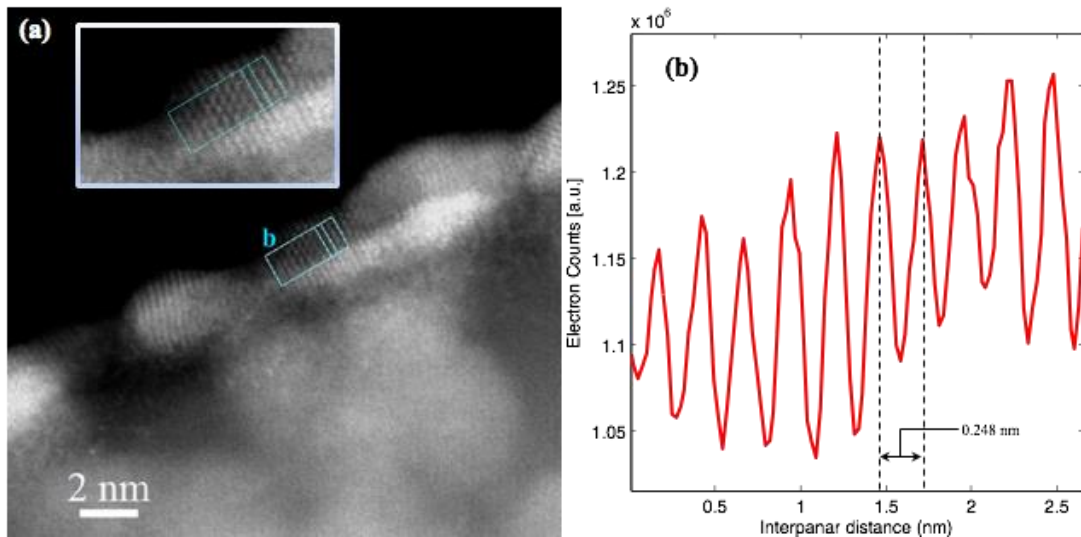


Figure 3. (a) High magnification STEM image for 2 nm thick AZO layer deposited over one SiNW. (b) Signal intensity profile of the AZO signal extracted from the area selected by the light blue box on a grain, the inset is a magnification of one of the AZO crystalline grains.

As far as it is known in the literature [30], AZO exists in two crystal structures: cubic zinc blende and hexagonal wurtzite. Both have a reticular plane with a distance of 2.48 Å. However, the literature data conducted on bulk AZO, indicate the zinc-blende phase as unstable, while the wurtzite one as stable, with the (100) planes having an interplanar distance equal to 2.488 Å [31].

The thickness of sputtered AZO is then increased to study the evolution of the system morphology in the subsequent deposition steps. Figure 4 shows the results for the sample on which the 20 nm thick AZO layer is deposited. The cross SEM micrograph in Figure 4a shows that the NWs maintain their oblique orientation with respect to the substrate when the thickness of material deposited increases up to 20 nm. The polycrystalline Si layer at the base of the SiNWs is covered by a very thin AZO film, as demonstrated by local EDX analysis, not shown here. The blue rectangle indicates the area from which the EDX spectrum shown in Figure 4b is extracted. i.e. from one nanowire. It can be seen that the dominant species is Si, as expected. The presence of Zn, O and Al signals confirms that the deposited shell is composed of AZO. The coverage results in any case uniform and conformal for the entire length of the wires and independent of the SiNWs tilt.

Figure 4(c) is the STEM micrograph taken on the same sample, showing that the layer of AZO coats its entire surface. It allows us to state that the clusters formed in the first deposition steps evolve into a continuous film onto the nanowires surface probably by following a mechanism growth like "Island growth" (Volmer-Weber [9]), where the small clusters, nucleated separately on the NW surface, grow as three-dimensional islands, and eventually coalesce to form a continuous film.

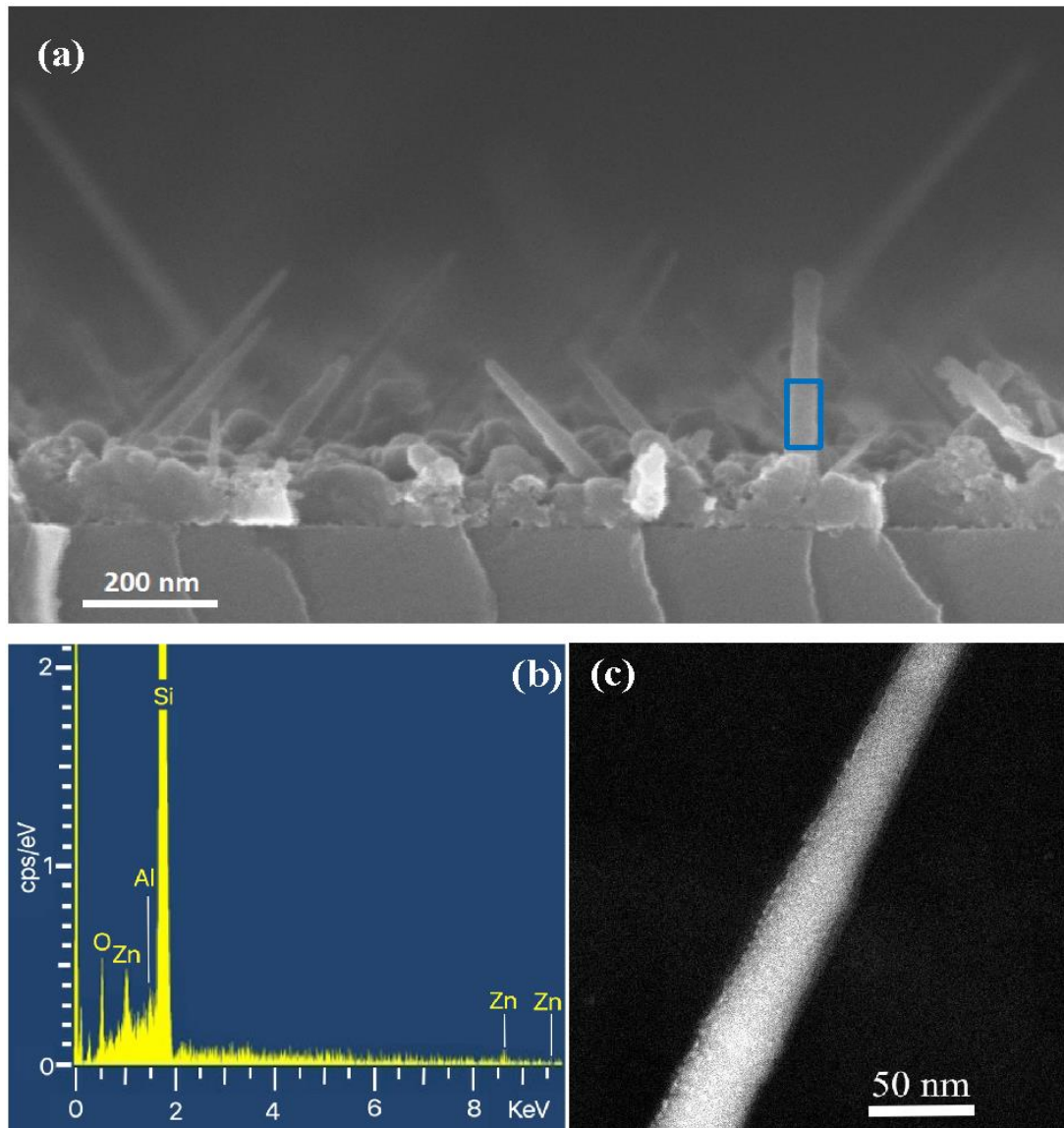


Figure 4. (a) Cross SEM analysis of a 20 nm thick AZO layer deposited on SiNW. (b) EDX spectrum extracted from the NWs area referred to in letter a. (c) STEM micrograph of a single NW coated with the equivalent 20 nm thickness of AZO.

Figure 5 shows the SEM micrographs (a) and TEM (b-c) in cross view of AZO with nominal thickness of 100 nm. It can be immediately observed that there are no empty spaces in the AZO shell. The most striking difference from the previous cases is that the core-shell NWs appear curved. To understand SiNWs bending observed in Figure 5 we explored several possible explanations. The effect of the weight force exerted by the AZO mass deposited (of the order of 10^{-14} g per wire, making the hypothesis of a cylindrical wire 30 nm large, 450 nm long and a total diameter SiNW+AZO equal to 130 nm) can be excluded since the wires Young modulus reported in the literature for silicon nanowires of similar size is of the order of one hundred GPa [32]. Previous work shows the bending of SiNWs after the implantation of Ga ions accelerated at energies of the order of tens of KeV [33]. In that case the bending was attributed to structural changes in crystallinity following implantation and to the momentum transferred from the Ga ions to the wires. In our case the AZO deposition was done at 50 W, with an acceleration voltage of about 0.1 kV, so that a bending of the SiNW as a consequence of the AZO impact is not probable. The possible strain effect exerted by the thick AZO onto the much thinner Si NW, causing the elongation/deformation of the Si crystalline cell could also be excluded because the AZO shell is polycrystalline, as already demonstrated. Another possible explanation could be the effect of the magnetic field on the piezoelectric AZO: its effect could be reset at the end of the deposition on the thin layers, but not on the thick ones, because those could 'encage' the SiNW core inside a rigid shell. However, at present we do not have a unique explanation and we need more investigations.

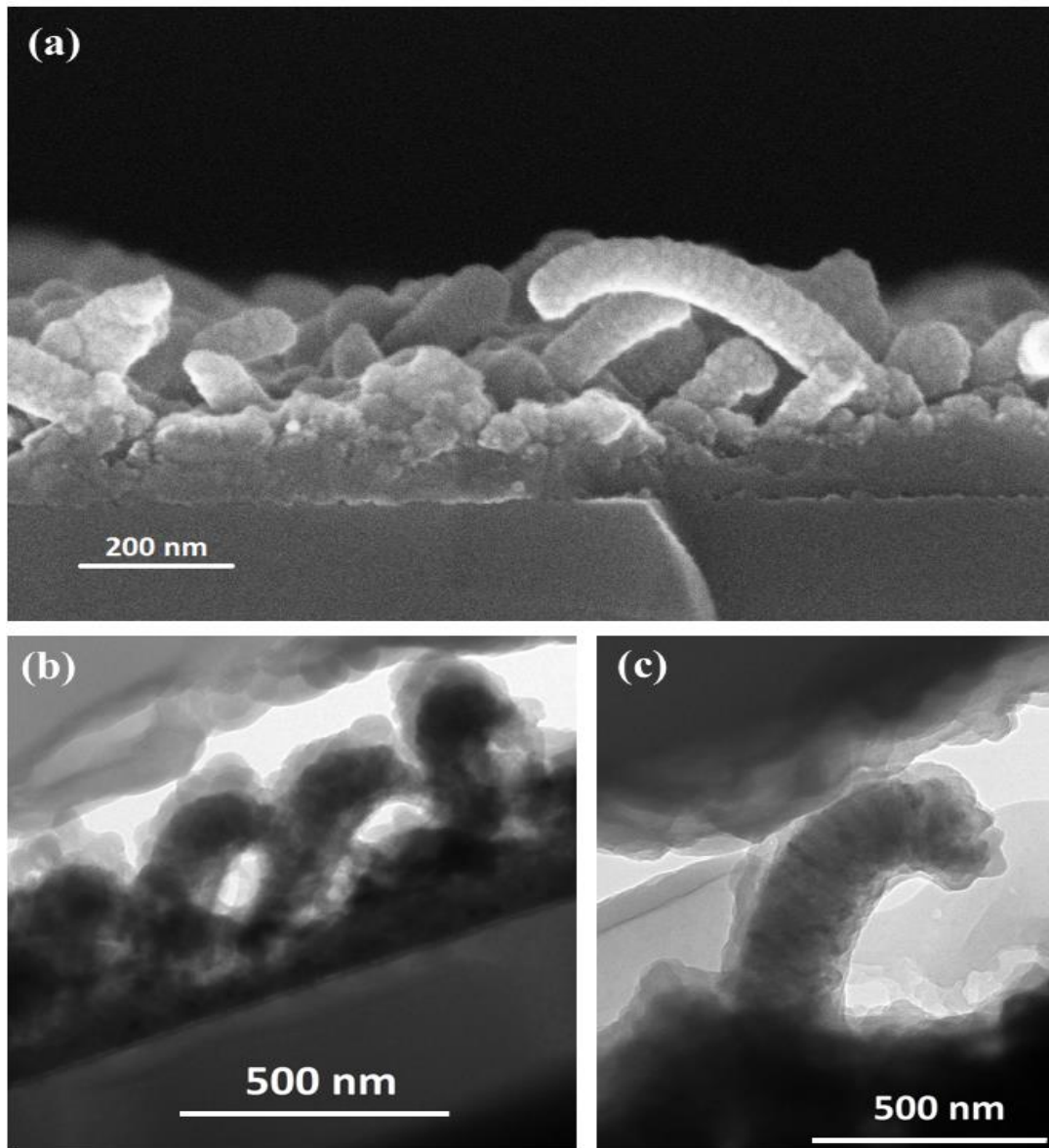


Figure 5. (a) SEM and (b-c) TEM microscopies in cross view of 100 nm thick AZO showing the conformal deposition of the oxide layer, the curved morphology of the nanostructure after the deposition and the inner silicon core with the AZO shell (b and c).

This observed phenomenon could have interesting applications because this particular morphology can be used as a tool to control the system electrical conductivity as well as its optical properties. In literature it is reported indeed that the photo-response performance increases by bending ZnO nanowires and this aspect could be significant for their applications [34, 35].

It should be noted that by increasing the nominal thickness from 20 nm to 100 nm, the two-dimensional AZO film deposited at the interface with the substrate, between the NWs, does not significantly increase in thickness. Given that by decreasing a material dimension to the nanoscale, the system surface / volume ratio, as well as the dangling bond density, increase, the adhesion of AZO on SiNWs could be favored [36,37]. These sites are at higher energy than they have in the ideal crystalline lattice. In this way, it can be explained why the AZO thickness is larger on the SiNW surface than on the substrate. We also point out that, for the application of this material, already in these deposition conditions, without further increasing the AZO thickness, the nanowire array is embedded in the AZO layer. The structure then could guarantee, in a device where the SiNW array works as an emitter, the electrical contact over the nanostructured layer.

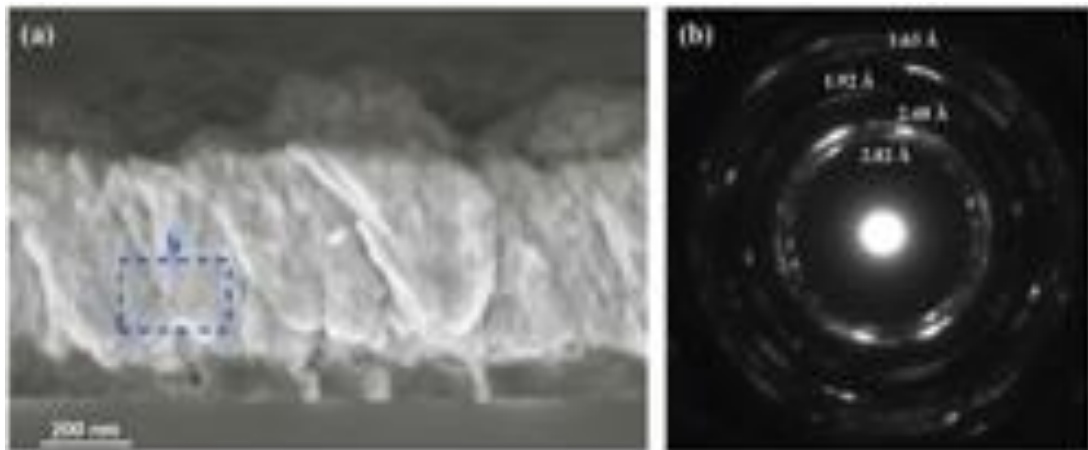


Figure 6. (a) SEM analysis in cross view of 500 nm AZO thick sample. (b) Diffraction pattern by electron beam carried out on to the selected area of the AZO layer as indicated by the dashed box in (a).

As the sputtering time further increases, the amount of material grows up and the morphology of the system changes. Figure 6a depicts the cross SEM of the 500 nm thick AZO sample. A planarized polycrystalline AZO matrix, with the embedded NWs is produced. From these observations it can be deduced that the sputtered material initially settles on the wires and on the Si at the interface, but the production of the thick AZO layer does not start before all wires have been conformally and fully coated. The diffraction patterns shown in Figure 6b are carried out on a large area of the

deposited bulk AZO matrix. Stretched spots inside the diffraction pattern are present, indicating that AZO is poly-crystalline and that the domains consist of several smaller crystals with preferential crystallographic orientation. The interatomic distances measured from the diffraction pattern, 2.82 Å, 2.48 Å, 1.92 Å and 1.63 Å, correspond to those of the ZnO in the wurtzite phase and in particular the distance 2.82 Å ($\langle 101 \rangle$ plane in wurtzite) does not appear among those of zinc-blende, therefore the possibility that the AZO is in this phase can be excluded. The crystallinity obtained is an encouraging result for good electrical conductivity needed for any electronic applications.

7.4 Conclusions

In this work we investigate the morphology of AZO on SiNWs, to understand its morphological and chemical evolution when deposited on substrates with complex shapes. Different nominal oxide thicknesses from 2 nm up to 500 nm are deposited. The 2 nm thick AZO turns out to be composed of nanoclusters distributed on the wire walls. Aluminum is detected even inside these initial small nano-clusters. The structure analysis reveals that the clusters are crystalline with an interplanar distance corresponding to that of the lattice in wurtzite phase. The 20 nm thick specimen shows a conformal two-dimensional AZO shell encapsulating the wires, probably produced according to the Volmer-Weber growth mechanism. By increasing the deposited oxide thickness, the AZO coating on the wires maintains the two-dimensionality without the appearance of empty spaces within it. With increasing the deposition thickness from 20 nm to 100 nm, we find that the thickness of the AZO film, deposited onto the Si substrate between the SiNWs, remains almost constant. This suggests a greater affinity of AZO for the NW surfaces. A noteworthy aspect is that oxide-coated SiNWs, with nominal thickness of 100 nm, appear hook-shaped after the deposition process. In literature it is reported that the photo-response performance increases by bending ZnO nanowires and this aspect could be significant for their applications. The deposited AZO material exhibits a wurtzite crystal structure, from the very early stages up to the bulk deposition. Bent composite structures, as well as the cluster decorated nanowires, can find applications in advanced plasmonic and optical systems.

Bibliography

- [1] T.J. Kempa, J.F. Cahoon, S.K. Kim, R.W. Day, D.C. Bell, H.G. Park, C.M. Lieber, 2012 *Proc. Natl. Acad. Sci. USA* **109** 1407–1412.
- [2] E. Garnett, P. Yang, 2010 *Nano Lett.* **10** 1082–1087.
- [3] D.S. Ginley, C. Bright, 2000 *MRS Bull.* **25.8** 15-18.
- [4] T. Kawashima, T. Ezure, K. Okada, H. Matsui, K. Goto, N. Tanabe, 2004 *J. Photochem. Photobiol. A* **164.1-3** 199-202.
- [5] R. Woods-Robinson, Y. Han, H. Zhang, T. Ablekim, I. Khan, K.A. Persson, A. Zakutayev, 2020 *Chem. Rev.* **120.9** 4007-4055.
- [6] Claes G. Granqvist, 2007 *Sol. Energy Mater. Sol. Cells* **91.17** 1529-1598.
- [7] S. Boscarino, I. Crupi, S. Mirabella, F. Simone, A. Terrasi, 2014 *Appl. Phys. A* **116** 1287–1291.
- [8] A. Shabani, M. K. Nezhad, N. Rahmani, Y. K. Mishra, B. Sanyal, & J. Adam, 2020 *Advanced Photonics Research* **2000086**.
- [9] B. Sarma, D. Barman, B.K. Sarma, 2019 *Appl. Surf. Sci.* **479** 786-795.
- [10] X. Li, C. Lin, C. Xu, 2019 *J. Mater. Sci. Mater. Electron.* **30.4** 3495-3503.
- [11] G. Torrisi, I. Crupi, S. Mirabella, A. Terrasi, 2017 *Sol. Energy Mater. Sol. Cells* **165** 88–93.
- [12] J.P. Kar, S. Kim, B. Shin, K.I. Park, K.J. Ahn, W. Lee, J.H. Cho, J.M. Myoung, 2010 *Solid State Electron.* **54** 1447–1450.
- [13] D. Miao, S. Jiang, H. Zhao, S. Shang, Z. Chen, 2014 *J. Alloys Compd.* **616** 26-31.
- [14] R.R. Lunt, J.B. Benziger, S.R. Forrest, 2010 *Adv. Mater.* **22.11** 1233-1236.
- [15] R.A. Puglisi, C. Bongiorno, S. Caccamo, E. Fazio, G. Mannino, F. Neri, S. Scalese, D. Spucches, A. La Magna, 2019 *ACS omega* **4.19** 17967-17971.
- [16] V. Schmidt, S. Senz, & U. Gösele, 2005 *Nano letters* **5(5)** 931-935.
- [17] C. Garozzo, A. La Magna, G. Mannino, V. Privitera, S. Scalese, P.M. Sberna, F. Simone, R.A. Puglisi, 2013 *J. Appl. Phys.* **113**, 214313.
- [18] S.H. Jeong, J.H. Boo, 2004 *Thin Solid Films* **447** 105-110.
- [19] R.H. French, H. Müllejjans, D.J. Jones, 1998 *J. Am. Ceram.* **81.10** 2549-2557.
- [20] G. Ballerini, K. Ogle, and M-G. Barthés-Labrousse, 2007 *Applied surface science* **253.16** 6860-6867.

- [21] Qiu, F. Cristiano, K. Huet, F. Mazzamuto, G Fisicaro, A La Magna, M. Quillec, N. Cherkashin, H. Wang, S. Duguay, & D. Blavette, 2014 *Nano Lett.* **14(4)** 1769-1775
- [22] E. Di Russo, P. Dalapati, J. Houard, L. Venturi, I. Blum, S. Moldovan, N. Le Biavan, D. Lefebvre, M. Hugues, J. M. Chauveau, D. C. Blavette, B. Deconihout, A. Vella, F. Vurpillot, & L. Rigutti, 2020. *Nano Lett.* **20(12)** 8733-8738.
- [23] Nanoelectronics: Doping difficulties deciphered. *NPG Asia Mater* (2010).
- [24] E. Arduca, & M. Perego, 2017 *Mater. Sci. Semicond. Process.* **62** 156-170.
- [25] S. Ossicini, F. Iori, E. Degoli, E. Luppi, R. Magri, R. Poli, G. Cantele, F. Trani & D. Ninno, 2006 *IEEE J. Sel. Top. Quant.* **12(6)** 1585-1591.
- [26] M. Samadi, M. Zirak, A. Naseri, E. Khorashadizade, & A.Z. Moshfegh, 2016 *Thin Solid Films.* **605** 2-19.
- [27] Ü. Özgür, Ya. I. Alivov, C. Liu, A. Teke, M. A. Reshchikov, S. Doğan, V. Avrutin, S.-J. Cho, and H. Morkoç, 2005 *J. Appl. Phys.* **98(4)** 11.
- [28] R. H. French, H. Mullejans & D. J. Jones, 1998 *J. Am. Ceram. Soc.* **81(10)** 2549–57.
- [29] Mi. Wu, D. Sun, C. Tan, X. Tian & Y. Huang, 2017 *Materials.* **10** 359.
- [30] L. P. Snedeker, A. S. Risbud, O. Masala, J. P. Zhang, & R. Seshadri, 2005 *Solid state sciences* **7.12** 1500-1505.
- [31] P.M. Perillo, M. N. Atia, D. F. Rodríguez, 2018 *Matéria (Rio J.)* **23.2**.
- [32] A. O. Furmanchuk, O. Isayev, T. C. Dinadayalane, D. Leszczynska, J. Leszczynski. 2012 *Wiley Interdiscip. Rev. Comput. Mol. Sci.* **2(6)** 817-828.
- [33] E. F. Pecora, A. Irrera, S. Boninelli, L. Romano, C. Spinella, F. Priolo, 2011 *Appl. Phys. A* **102(1)** 13-19.Y.A.
- [34] Greenberg, A. Kelrich, S. Cohen, S. Kar-Narayan, D. Ritter, Y. Calahorra, 2019 *Nanomaterials* **9(9)** 1327.
- [35] B. Bharti, S. Kumar, & R. Kumar, 2016 *Appl. Surf. Sci.* **364** 51-60.
- [36] J-J. Gallet, F. Bournel, F. Rochet, U. Köhler, S. Kubsky, M.G. Silly, S. Sirotti, D. Pierucci, 2011 *J. Phys. Chem. C.* **115.15** 7686-7693.
- [37] P. Gao , Z. Z. Wang , K. H. Liu , Z. Xu , W. L. Wang , X. D. Bai & E. G. Wang, 2009 *J. Mater. Chem.* **19** 1002-1005.

Conclusions

In this thesis SiNWs arrays were synthesized through the IP-CVD / VLS method and a new, more efficient and rapid post growth removal process of the catalyst (Au) was developed.

The main scope of the thesis was to study the SiNWs plasmonic features through the EELS technique. The SiNWs were found to support longitudinal (LM) and transverse (TM) plasmonic modes in the UV-Vis. For the first time, the spatial distribution of the electric field in these nanostructures has been mapped allowing to distinguish between the LM and TM modes. The former have proved to be propagating while the last one are localized. Moreover, the LMs show a harmonic behavior, i.e. the nanostructure works as a Fabry-Perot resonator in which the electric field is distributed in discrete spots along the main axis of the wires. This behavior is due to the reflection of the propagating plasmonic waves at the ends of the wire that giving rise to standing waves along the wire. This experimental evidence is in good agreement with the optical and electrodynamic simulations.

It has been confirmed that this behavior is maintained as the diameter of the wires decreases up to about 20 nm, however, below 12 nm in diameter this behavior seems to disappear for some reason yet to be understood. The onset of quantum effects, or simply physical compression effects due to the further reduced dimensionality are currently being studied.

Another element that has begun to be experimentally investigated is the effect of the variation in the thickness of the oxide on the spectral characteristics. Preliminary results clearly show that the EELS behavior in the UV-Vis range significantly depends on this parameter. Deeper investigation is currently underway.

Lastly, a study was presented related to the deposition of a TCO on these nanostructured substrates by an industrially scalable technique such as magnetron sputtering. The first steps of AZO deposition on SiNWs were investigated in order to understand the interaction mechanisms during the first deposition steps and as the thickness of the deposit increases. Surprisingly, we observed that the system composed of AZO + SiNWs shows a great curvature as the nominal thickness of deposited AZO increases. This unprecedented result is of great interest as it could be useful in piezoelectric devices or flexible screens.

Acknowledgments

I would like to thank my family without whom nothing would have been possible; my friends for their precious company in the annoying moments.

Furthermore, I would like to thank my supervisor Prof. Salvatore Patanè, and my cosupervisor Dr. Rosaria A. Puglisi especially for the skills transferred to me; all my PhD colleagues and in particular Dr. Mattia Pizzone with whom I shared the most intense moments of the daily activity research.

I would especially thank the Southern Denmark University for the opportunity and resources offered to me during my virtual visitor period and beyond, in particular the mechatronics group for the constant availability, friendliness and support towards me, in particular to the Prof. Jost Adam and Dr. Alireza Shabani, Dr. Matiyas Tsegay Korsaa, Dr. Neda Rahamani, Dr. Søren Petersen.

Other thanks go to the CNR-IMM institute of Catania where most of the experimental activity took place, to all researchers, technical staff, PhD students, fellows, postdocs with whom I have had the pleasure of dealing.

Finally, I would like to thank the University of Messina, in particular to the coordinator of the doctorate Prof. Vincenza Crupi and to all the professors I have learned from over the years.